Catalytic and Optical Application of Metal oxide and Carbon Dot Nanostructures: Effect of Morphology and Concentration

Thesis submitted in fulfillment of the requirement for the degree of

Doctor of Philosophy

By

Akansha
(Regn. No: 901509001)

Under the supervision of

Dr. Soumen Basu
(Associate Professor)

SCHOOL OF CHEMISTRY AND BIOCHEMISTRY
THAPAR INSTITUTE
OF ENGINEERING & TECHNOLOGY
(Deemed to be University)
PUNJAB, INDIA

May, 2018

DEDICATED

TO

MY

GRAND PARENTS

&

PARENTS

CERTIFICATE

This is to certify that thesis entitled "**Catalytic and Optical Application of Metal oxide and Carbon Dot Nanostructures: Effect of Morphology and Concentration**", being submitted by Mrs. Akansha in fulfillment of the requirement for the award of the Degree of Doctor of Philosophy in the School of Chemistry and Biochemistry, Thapar Institute of Engineering and Technology, Patiala, is a record of candidate's own independent and original research work carried out by her under my supervision and guidance. The matter presented in this thesis has not been submitted in part or full for the award of any degree in any other University or Institute.

SBasu

(Supervisor)
Dr. Soumen Basu
Associate Professor
School of Chemistry and Biochemistry
Thapar Institute of Engineering and Technology
Patiala- 147004, Punjab (India)

CANDIDATE'S DECLARATION

I, hereby declare that the work presented in the thesis entitled "Catalytic and Optical Application of Metal oxide and Carbon Dot Nanostructures: Effect of Morphology and Concentration", in fulfillment of the requirement for the award of the Degree of **Doctor of Philosophy**, School of Chemistry and Biochemistry, Thapar Institute of Engineering and Technology, Patiala, is an authentic record of my own work carried out under the supervision of Dr. Soumen Basu, Associate Professor, School of Chemistry and Biochemistry, Thapar Institute of Engineering and Technology, Patiala, India. The matter embodied in this thesis has not been submitted in part or full to any other university or institute for the award of any degree in India or Abroad.

S Basu

(Supervisor)
Dr. Soumen Basu
Associate Professor
School of Chemistry and Biochemistry
Thapar Institute of Engineering and Technology
Patiala- 147004, Punjab (India)

Akansha
Akansha

ACKNOWLEDGMENTS

"Radha Soami"

I devoutly thank almighty for granting me strength to profitably accomplish this project.

Through this section of the thesis, I would like to express my heartiest thankfulness to all those who encouraged and supported me in many ways for the accomplishment of this study and made it an unforgettable journey for me.

This work was carried out in the Advanced Nanomaterials Laboratory (Thapar Institute of Engineering and Technology) between 2015-2018. I would like to express my sincere thanks to my supervisor Dr. Soumen Basu, for giving me the opportunity to work on such a fascinating project with all necessary supports and continuous guidance throughout my study.

Many thanks to Dr. Amjad Ali, Head of School of Chemistry and Biochemistry Thapar Institute of Engineering and Technology, Patiala for his ever-helping attitude and good wishes. I would also like to express my special regards to the members of my doctoral committee, Dr. Satnam Singh, Dr. Amjad Ali and Dr. Rajeev Mehta for their perceptive comments, advices and scientific discussions. Special thanks to all the ***Teaching Faculty*** *of the department for their cooperation and guidance. Also, special thanks to Mr. Chander Thakur and office staff Mr. Mayank Sharma for their cooperation and timely support. I sincerely acknowledge Dr. O.P. Pandey Dean R & SP for finical support. The help from different laborites like SAI labs, CSIO Chandigarh and Sprint Testing Solutions is highly acknowledged.*

I warmly thank all my friends and lab mates Mr. Amit Mishra, Dr. Manisha Sharma, Mr. Jasminder Singh, Ms. Shagun Kainth, Ms. Surbhi, Ms. Aanchal, Ms. Aditi, Ms. Akansha for great time and moral support. I will forever cherish the warmth shown by them, whose smiling faces always inspired me. Special thanks to Dr. Rayees Ahmad for guidance, support and precious friendship.

The words are insufficient to convey my heartfelt gratitude to my father Mr. Rajesh Kumar and my mother Mrs. Anita Mehta for their encouragement and inspiration throughout my *research work. I owe everything to them. My special thanks to my younger sister, Ms. Yashvi Mehta, my grandpa, grandma, the whole Prempushp Parivar and Mehta family for unconditional love and support from childhood. A bottomless gratitude to my Father-in-law Late Mr. Raj Kumar and Mother-in-law Mrs. Kawaljeet Kaur for their sustained encouragement. Also thankful to the cheerful support of Mr. Satnam and Mrs. Penaz Bhandal throughout and always.*

Saving the most important for last, I would like to extend a huge thank you to my partner Mr. Prabhnoor for endless patience, help and support.

Besides this, I am thankful to the persons who knowingly and unknowingly helped me during the successful completion of this work.

Akansha

Akansha

TABLE OF CONTENTS

CHAPTER 1

Introduction and Literature

CHAPTER 2

Gold Nanoparticles Grafted Mesoporous Silica: A Highly Efficient and Recyclable Heterogeneous Catalyst for Reduction of 4-Nitrophenol

CHAPTER 3

Effect of Au Content on the Enhanced Photocatalytic Efficiency of Mesoporous Au/TiO_2 Nanocomposites in UV and Sunlight

CHAPTER 4

Controlled Photocatalytic Hydrolysis of Nitriles to Amides by Mesoporous MnO_2 Nanoparticles Fabricated by Mixed Surfactant Mediated Approach

CHAPTER 5

Enhanced photocatalytic water splitting by gold carbon dot core shell nanocatalyst under visible/sunlight

CHAPTER 6

Optical Detection of Thiol Drugs by Core Shell Luminous Carbon Dots- Gold Nanoparticles System

CHAPTER 7

Highly Effective CQD/TiO_2 Nanocomposite For Sensing of Toxic Metal Ions and Photodetoxification of Industrial Dyes with Kill Waste by Waste Concept

CHAPTER 8

Fluorescent Carbon Dots decorated MnO_2 Nanorods for Complete Photo mineralization of Phenol

BET	Brunauer Emmett Teller
BJH	Barrett-Joyner-Halenda
CB/E_{CB}	Conduction band/Electronic conduction band
DRS	Diffuse reflectance spectroscopy
FESEM	Field emission scanning electron microscopy
GC	Gas chromatography
HPLC	High pressure liquid chromatography
HRTEM	High resolution transmission electron microscopy
I-V	Potential-Voltage
JCPDS	Joint committee on powder diffraction standards
L	Length
M	Metal
mL	Milli-litre
mM	Milli molar
mol	Mole
mTiO_2	Mesoporous-TiO_2
NHE	Normal hydrogen electrode
nm	Nanometre
NP	Nanoparticle
PEC	Photoelectrochemical cell
PL	Photoluminescence
P25-TiO_2	Commercially available P25-TiO_2
SAED	Selected area electron diffraction
SPR	Surface plasmon resonance
STH	Solar to hydrogen
TCD	Thermal conductivity detector
TEM	Transmission electron microscopy
TGA	Thermogravimetric analysis
UV	Ultraviolet

VB/E_{VB}	Valence band/Electronic valence band
Vis	Visible
vol%	Volume percentage
W	Width
wt%	Weight percentage
XPS	X ray photoelectron spectroscopy
XRD	X-ray diffraction
1D	One dimensional
µL	Micro-litre
µM	Micro molar
CQDs	Carbon quantum dots
SiO_2	Silicon dioxide
MnO_2	Manganese dioxide
Au/Ag	Gold/Silver
SBA-15	Santa Barbara amorphous type material
HDP	Homogeneous deposition–precipitation
NP	Nitro phenol
AP	Aminophenol

LIST OF SYMBOLS

e^-	Electron
h^+	Hole
$OH^{\cdot}$	Hydroxyl radical
E_g	Band gap
Å	Angstrom
α	Absorption coefficient
A	Absorbance
°	Degree
λ	Wavelength
%	Percentage
μ	Micro
Θ	Theta
τ_{av}	Average lifetime
H	Hour
Φ	Work function
E^o	Electrode potential
m	Meter
g	Gram
mg	Milligram
E_f	Fermi energy
V	Volt
d	Distance
s	Second
C	Concentration
ν	Frequency
μmol	Micromol

List of Publications

1. **Mehta A**, Mishra A, Basu S. Highly Effective CQD/TiO_2 Nanocomposite For Sensing of Toxic Metal Ions and Photodetoxification of Industrial Dyes with Kill Waste by Waste Concept. *Material and Design*. 2018 (I.F - 4.3).
2. **Mehta A**, Mishra A, Basu S. Fluorescent Carbon Dots decorated MnO_2 Nanorods for Complete Photomineralization of Phenol from Water. *Environmental Science: Water Research & Technology*.2018 (I.F - 3.6)
3. **Mehta A**, Pooja D, Thakur A, Basu S. Enhanced photocatalytic water splitting by gold carbon dot core shell nanocatalyst under visible/sunlight. *New Journal of Chemistry*. 2017; 41(11):4573-81 (IF= 3.2).
4. **Mehta A**, Basu S. Controlled photocatalytic hydrolysis of nitriles to amides by mesoporous MnO_2 nanoparticles fabricated by mixed surfactant mediated approach. *Journal of Photochemistry and Photobiology A: Chemistry*. 2017 Jun 15; 343:1-6 (IF= 2.6).
5. **Mehta A**, Sharma M, Kumar A, Basu S. Effect of Au content on the enhanced photocatalytic efficiency of mesoporous Au/TiO_2 nanocomposites in UV and sunlight. *Gold Bulletin*. 2017 Mar 1; 50(1):33-41(IF= 1.6).
6. **Mehta A**, Sharma M, Kumar A, Basu S. Gold Nanoparticles Grafted Mesoporous Silica: A Highly Efficient and Recyclable Heterogeneous Catalyst for Reduction of 4-Nitrophenol. *Nano*. 2016 Sep; 11(09):1650104 (IF= -).
7. **Mehta A**, Mishra A, Basu S. Luminescent carbon quantum dot-Au nanoparticles system for fluorescence turn-on/off detection of biothiols. *Plasmonics*. 2018 (IF= 1.6).
8. **Mehta A**, Mishra A, Basu S. Band Gap Tuning and Surface Modification of Carbon Dots for Sustainable Development Application. 2018 (Under Review).
9. Dongre R S, Sadasivuni K K , Ponnamma D, **Mehta A**, Basu S, Meshram J S, Ali Al-Maadeed M A. Biocomposite for purification of water. 2017 (Under Review).

Other Publications

1. **Mehta A**, Mishra A, Sharma M, Singh S, Basu S. Effect of silica/titania ratio on enhanced photooxidation of industrial hazardous materials by microwave treated mesoporous SBA-15/TiO_2 nanocomposites. *Journal of Nanoparticle Research*. 2016 Jun 1; 18(7):209 (IF= 2.0).
2. Sharma M, Jain P, Mishra A, **Mehta A**, Choudhury D, Hazra S, Basu S. Variation of surface area of silica monoliths by controlling ionic character/chain length of surfactants and polymers. *Materials Letters*. 2017 May 1; 194:213-6 (IF= 2.5).
3. Mishra A, **Mehta A,** Sharma M, Basu S. Enhanced heterogeneous photodegradation of VOC and dye using microwave synthesized TiO_2/Clay nanocomposites: A comparison study of different type of clays. *Journal of Alloys and Compounds*. 2017 Feb 15;694:574-80 (IF= 3.1).
4. Sharma M, Mishra A, **Mehta A**, Choudhury D, Basu S. Enhanced catalytic and antibacterial activity of nanocasted mesoporous silver monoliths: kinetic and thermodynamic studies. *Journal of Sol-Gel Science and Technology*. 2017 Mar 1;81(3):704-10 (IF= 1.5).
5. Mishra A, **Mehta A**, Sharma M, Basu S. Impact of Ag nanoparticles on photomineralization of chlorobenzene by TiO_2/bentonite nanocomposite. *Journal of Environmental Chemical Engineering*. 2017 Feb 28;5(1):644-51 (IF= -).
6. Mishra A, Sharma M, **Mehta A**, Basu S. Microwave Treated Bentonite Clay Based TiO2 Composites: An Efficient Photocatalyst for Rapid Degradation of Methylene Blue. *Journal of Nanoscience and Nanotechnology*. 2017 Feb 1;17(2):1149-55 (IF= 1.3).
7. Sharma M, Mishra A, **Mehta A**, Basu S. Effect of Surfactants on the Structure and Adsorption Efficiency of Hydroxyapatite Nanorods. *Journal of Nanoscience and Nanotechnology* 2017 Jan 1;17: 1-11 (IF= 1.3).
8. Garg D, **Mehta A,** A Sensitive Turn Off – Turn On Fluorescent Probe For Detection Of Biothiols Using MnO_2@Carbon Dots. *Spectrochimica Acta Part A: Molecular and Biomolecular Spectroscopy* 2017 Nov 192: 411-419 (IF= 2.0).
9. Arora N, **Mehta A**, Mishra A. Nitrophenol Reduction Catalysed by Au-Ag Bimetallic Nanoparticles Supported in LDH: Homogeneous Vs. Heterogeneous Catalysis. *Applied Clay Science*. 2018 Jan 31; 151: 1-9 (IF= 3.3).
10. Kumar M, **Mehta A**, Mishra A, Singh J, Rawat M, Basu S. Biosynthesis of Tin

Oxide Nanoparticles using Psidium Guajava Leave Extract for Photocatalytic Dye Degradation under Sunlight. *Materials Letters*. 2017 Dec 18 (IF= 2.5).

11. Mishra A**, Mehta A**, Kainth S, Basu S. Effect of different plasmonic metals on photocatalytic degradation of volatile organic compounds (VOCs) by bentonite/M-TiO_2 nanocomposites under UV/visible light. *Applied Clay Science*. 2018 Mar 1;153: 144-53 (IF= 3.3).
12. Singh J, **Mehta A**, Mishra A, Rawat M, Basu S. Green Synthesis of Silver Nanoparticles Using Sun Dried Tulsi Leaves and Its Catalytic Application for 4-Nitrophenol Reduction. *Journal of Environmental Chemical Engineering*. 2018.6, 1468-1474 (IF= -).
13. Kaur N, **Mehta A**, Mishra A, Chaudhary S, Rawat M, Basu S. Amphiphilic Carbon Dots Derived By Cationic Surfactant for Selective and Sensitive Detection of Metal Ions. 2018 (Under Review).
14. A. Mishra, **Mehta A**, S. Basu, Effect of g-C_3N_4 Loading on TiO_2/Bentonite Nanocomposites for Efficient Heterogeneous Photocatalytic Degradation of Industrial Dye under Visible Light. 2018 (Under Review).
15. A. Mishra, **Mehta A**, S. Basu, A comparative study on the effect of different precursors for synthesis and efficient photocatalytic activity of g-C_3N_4/ TiO_2/Bentonite Nanocomposites. 2018 (Under Review).
16. Kaur S, **Mehta A**, Mishra A, Chaudhary S, Rawat M, Basu S. Highly fluorescent carbon dots derived from Mango leaves for selective detection of metal ions. 2018 (Under Review)
17. Dashairya L, **Mehta A,** Basu S, Saha P. Significant improvement in Photocatalytic degradation of Rhodamine-B by novel rod-shaped $BiSbS_3$ nanostructure. 2018 (Under Review).

Papers presented in Conferences /Workshops attended

1. Paper presentation (Poster) in National Conference on Material Science Applications in Energy and Environment at DAV Jalandhar on March 17, 2018 (**Best Poster Award)**.
2. Paper presentation (Oral) in International Conference on Nano for Energy and Water at Dehradun on Feb 22-24 2017.
3. Paper presentation (Oral) in 28th Annual General Meeting of Materials Research Society of India held at IIT Mumbai on Feb 13-15, 2017.
4. Paper presentation (Poster) in HETIS held at Punjab University Chandigarh on Sep 29- 30, 2016.
5. Paper presentation (Poster) in Third international conference on nanotechnology for better living held at National Institute of Technology Srinagar, India on May 25-29, 2016.
6. Paper presentation (Poster) in Second conference on microscopy in materials science (AMST-2016) held at Thapar University, Patiala on February 25-27, 2016.
7. Paper presentation (Poster) in International conference on recent advances in emerging technologies ICRAET-2016 held at SGGSWU Fatehgarh Sahib on February 23-24, 2016.
8. Participated in National workshop on advanced techniques for surface characterization held at Thapar University, Patiala on October 28-30, 2015.

ABSTRACTS

The thesis entitled "**Catalytic and Optical Application of Metal oxide and Carbon Dot Nanostructures: Effect of Morphology and Concentration**" is divided into eight chapters.

CHAPTER 1: This chapter gives the brief highlight of thesis including introduction, literature survey and scope of my work. The first section elaborates the basis of semiconductor photocatalysis with a precise discussion on titanium dioxide TiO_2, SiO_2 and MnO_2. The detailed photocatalysis mechanism by semiconductors is also pictorially eloborated in this section. The second section is focused upon the synthesis , band gap tunning, surface modification and sustianable applications of carbon quantam dots (CQDs). Moreover the research gaps, objectives and characterization techniques with specification has also been integrated.

CHAPTER 2: This chapter signifies the synthesis of gold nanoparticles dispersed uniformly on mesoporous silica (mAu/SiO_2) by homogeneous deposition–precipitation method. Silica provides support and surface area to increase catalytic activity of gold. X-ray photon spectroscopy revealed binding energy of Au $4f_{7/2}$ (~84.0 eV) and Au $4f_{5/2}$ (~87.7 eV) which supports the formation of Au^0 on SiO_2 surface. Au/SiO_2 showed Langmuir type-IV isotherms which are the characteristic features of mesoporous materials furthermore, pore size decreases with incorporation of Au NP's on SiO_2 surface. The enhancement is due to the strong interaction of Au^0 with silica support. The Au/SiO_2 as photocatalyst was used for the conversion of 4-Nitrophenol (4-NP) to 4- Aminophenol (4-AP). The catalytic conversion was studied by UV-Visible spectroscopy and HPLC quantification method, which shows conversion of nitro group into amino group. In addition, the catalyst was easily separated and reused. The reusability studies of the catalyst exhibited better reduction of 4-NP to 4- AP even after 10 consecutive cycles. In comparison to trisodium citrate capped pure gold nanoparticles mAu/SiO_2 catalysts showed very good catalytic activity toward nitrophenol reduction. Here we conclude that embedment of metal catalysts like Au into high surface area support like silica is a positive step towards development of novel heterogeneous catalysts.

CHAPTER 3: Detoxification of harmful dyes through non conventional catalytic processes is getting thrust in light of environmental remediation. This chapter reveals the synthesis of gold-titania (Au/TiO_2) mesoporous nanostructure and its photocatalytic performance for degradation of alizarin dye. Optically Au/TiO_2 shows a characteristic surface plasmonic

absorption band at 520 nm, XRD pattern reveal the anatase phase of TiO_2 with fcc unit cell structure and tetragonal geometry. X-ray photon spectroscopy depicts (Au $4f_{7/2}$ at 84.0 and Au $4f_{5/2}$ at 87.7 eV) the elemental state of gold (Au^0). Specific surface area was witnessed to decrease with increase of Au content (169, 141, 130, 119 m^2/g for 1, 2, 3 and 4 wt% respectively). Au/TiO_2 nanocomposite showed higher catalytic performance in comparison to TiO_2 (P25), this change is credited to better charge delocalisation at metal semiconductor interface.The reusability studies of the photocatalyst exhibited more than 98% degradation of the dye even after 10 consecutive cycles.

CHAPTER 4: The solid-phase MnO_2 nanoparticles fabricated by surfactant template method were exploited as the photocatalyst for the effective one-step synthesis of amides. Cationic or anionic surfactants and their combinations were used as porous templates to obtain the mesoporous MnO_2 nanoparticles with variable pore volume (0.23 to 1.95 cm^3/g). The morphological and structural observation of the material confirms the uniform facet structure (37.68 nm) of MnO_2 nanoparticles. The surface elemental state was confirmed by XPS analysis confirming Mn $2p_{3/2}$ (642.5 eV) and $Mn2p_{1/2}$ (654.7 eV) spin states, that are common for the tetravalent Mn ions. Presence of surfactant as stabilizer was also witnessed with a strong peak of C 1s (283-286 eV). The textural parameters obtained from XRD and Raman analysis depicted the β-phase and rutile type framework of MnO_2.The selective conversion of nitriles to amides was studied without any acid by products under visible light irradiation in the basic/neutral medium. Amides were obtained from various substrates (nitriles) with excellent yields (70-90%).

CHAPTER 5: The hydrogen production from water using photocatalyst under sunlight still remains a huge challenge. The search of suitable photocatalyst would combine an ability to dissociate water molecules having a band gap that absorbs light in visible range and to remain stable in contact with water. In, this regard present chapter represents a facile method for the fabrication of carbon quantum dots (CQDs) and Au@CQDs, useful for the photocatalytic hydrogen generation from water. The optical properties revealed the band gap energy (eV) for CQDs (2.78) and Au@CQDs (2.68); while photoluminescence analysis of CQDs showed maximum emission at 460 nm and also exhibits red shift when excited at longer wavelengths. Spherical shaped CQDs with an average size of 7 nm, d spacing of 0.22 nm, and core shell Au@CQDs with shell thickness of 6 nm was observed by HRTEM analysis. Comparatively both CQDs (260 μmol) and Au@CQDs (280 μmol) displayed higher rate of hydrogen production under sunlight irradiation than other carbon materials reported earlier. In photo electrochemical analysis, the current densities associated Au@CQDs and CQDs photoelectrodes (PEs) were found to be 16 mA/cm^2 and 6 mA/cm^2, respectively at very low bias of 0.16 V. Moreover, the Frequency response analysis (FRA) response associated to Randel's equivalent circuit shows that the polarization/charge transfer resistance for Au@CQDs is very low (2.74 ohm) over that of CQDs PEs (88.8 ohm), which is 12.9 kohm for bare TiO_2 PEs. All these observations indicate that both CQDs and Au@CQDs are ample for prevention of electron-hole recombination processes, which ultimately leads to superior photocatalytic water splitting.

CHAPTER 6: Nowadays carbon quantum dots (CQDs) with size less than 10 nm have emerged as one of the most exciting areas of chemical research in the class of inorganic nanomaterials. This chapter presents some interesting characteristics of CQDs and their fluorescence turn on/off quenching for the detection of 6-Thioguanine (6-TG). The CQDs were fabricated by simple one-step microwave technique and used for the simultaneous reduction of Au^{3+} to form Au^0-CQD core-shell (Au@CQDs) nanocomposites. The CQDs formed were spherical in shape having an average size of ~7 nm confirmed by HRTEM and DLS study. The interaction of CQDs with Au leads to its fluorescence turn off up to 96% analysed by UV-Visible, fluorescence spectroscopy and fluorescence lifetime measurements. The turn on fluorescence of CQDs has been witnessed by the formation of complex with 6-TG $[Au\text{- }(6\text{-TG})_n]^{3-}$ in the presence of thiols. Meanwhile, linear relationship between turn on fluorescence against the concentration of 6-TG is obtained in the range of 0-100 μM with the correlation coefficient of 0.9944 and limit of detection for 6-TG has been found to be 0.01μM. The Au@CQDs could also act as biosensor for the detection of various amino acids, enzymes and pentids drug.

CHAPTER 7: The exposure of even low amount of heavy metals and industrial dyes in wastewater leads to cardiovascular, reproductive, neurological and developmental disorders. Consequently, millions of inorganic, biological and organic pollutants containing toxic heavy metals have been accounted as water contaminants. This chapter illustrates a novel approach based on the methodology to "kill waste by waste". Firstly the toxic metal like lead (Pb) ions were detected using highly fluorescence carbon quantum dots (CQDs) and after impregnated of TiO_2 into the same Pb-CQDs composite, it was further used for the photodegradation of harmful industrial dyes like Reactive brilliant red X-3BS (RBX), Coralene red BS (CRB) and Remazol black XP (CNB). The CQDs have been constructed as a nanosensor for Pb ion detection and its fluorescence is effectively quenched with good sensitivity (0.070 μM) and selectivity. This Pb-CQDs solution was further immersed in TiO_2 by wet impregnation method to fabricate Pb-CQDs-TiO_2 (PCT) nanocomposite with a change in the energy gap (3.2 to 2.8 eV) making the composite active in visible light irradiation. The degradation efficiency achieved ~100% mark for RBX dye with the CO_2 evolution of 1.8 µmols in 60 minutes. The plausible mechanism has been proposed based on GCMS studies suggesting the formation of intermediates like triazine and aryl sodium sulphonates before complete decomposing into CO_2 and water. The presenting probe also reveals excellent analytical feature for real-time applications of lead ions in wastewater.

CHAPTER 8: The enormous generation of wastewater has become the highest rated problem all over the world and day by day photocatalysis is gaining its importance as best option for its treatment. In context to recent studies this chapter signifies the development of novel MnO_2@CQD nanocomposite (carbon dots decorated on MnO_2 nanorods) which was prepared by a facile one-pot hydrothermal method. The optical properties revealed an excitation edge at 540 nm and a band gap of 1.3 eV for the nanocomposite. Structural and morphological studies revealed the open-ended MnO_2 nanorods (length and breadth are 5 nm and 1 nm respectively) and the spherical CQDs (5-7 nm) are seen deposited on the surface of MnO_2. The nanocomposite also possesses high surface area (95.3 m^2g^{-1}) and pore diameter (39 nm) which directly influences the ionic transport. Using MnO_2@CQDs the photocatalytic degradation of phenol was tested under varies operational parameters. Under optimum operational parameter, phenol degradation efficiency was found to be ~90 % with rate constant R = 0.029 min^{-1}. The mechanism for higher activity of MnO_2@CQD nanocomposite was elucidated by different scavenger and cyclic voltammetry study. These results underline the prospective application of this metal-free photocatalyst in water treatment.

INTRODUCTION AND LITERATURE

1.1 Background

1.1.1 Catalysis and Photocatalysis

Any substance in chemical terms can be a photocatalyst when it accelerates the photochemical reaction without being consumed in the process. In other words, we can say that it lowers the activation energy of the photochemical reaction. One of the most common examples can be the photosynthesis process which takes place inside the leaves of many trees and plants. Many other photocatalytic reactions have been carried out artificially such as photocatalytic organic processes water splitting for fuel cell applications and advanced oxidation process [1-3]**.** The photocatalyst can hasten the reaction in two ways: either it can react with the substrate in its original or excited state or with final products of photoreaction [4-5] as represented in Fig. 1.1.

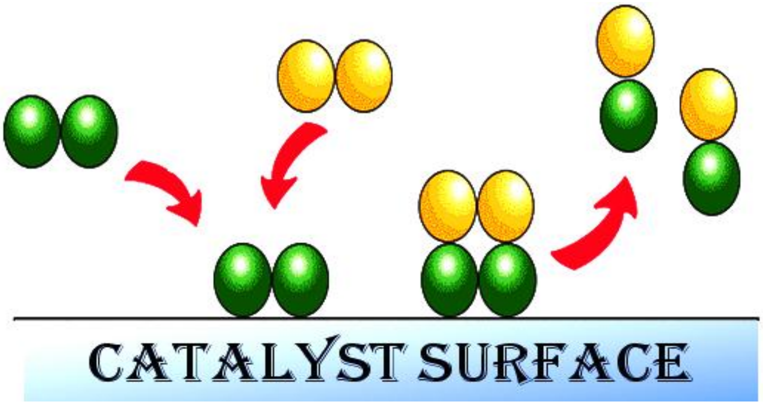

Fig. 1.1: Pictorial representation of catalysis reaction.

1.1.2 Semiconductor Photocatalysis

Semiconductors are the idyllic materials for photocatalysis reaction owing to their unique electronic structure which allows the spatial separation of charge carriers through absorption of photons. When a molecule is formed bonding and antibonding orbital develop according to Pauli exclusion principle. In, a diatomic molecule the energy level of an isolated atom splits into two molecular orbitals, one is lower in energy and other higher than the original atomic level. Generally only the less energetic orbital is occupied. While monomers are placed together, the energy required to photoexcite the electron decreases [6, 7].

Mathematically for n atomic orbitals in a molecule, n molecular orbitals are always formed. Concluding, as the number of molecular orbital increases, the energy gap between highest bonding and lowest bonding orbital increases, also the gap between each individual orbital decreases. For a huge number of monomers such as in crystalline solid a band of allowed energy is created for unoccupied and occupied states. These are also known as conduction and valence bands, which are separated by forbidden energy level called as band gap (Eg) [8-10]. In the present work, we are focusing on such catalytic processes for various sustainable applications. The photocatalytic process of semiconductor is reported to occur by absorption of photon of energy greater than or equal to the semiconductor bandgap energy, which afterward leads to the promotion of electron (e-) from the valence band to the conduction band, also creating a hole (h+) in the valence band pictorially shown in Fig. 1.2 [11].

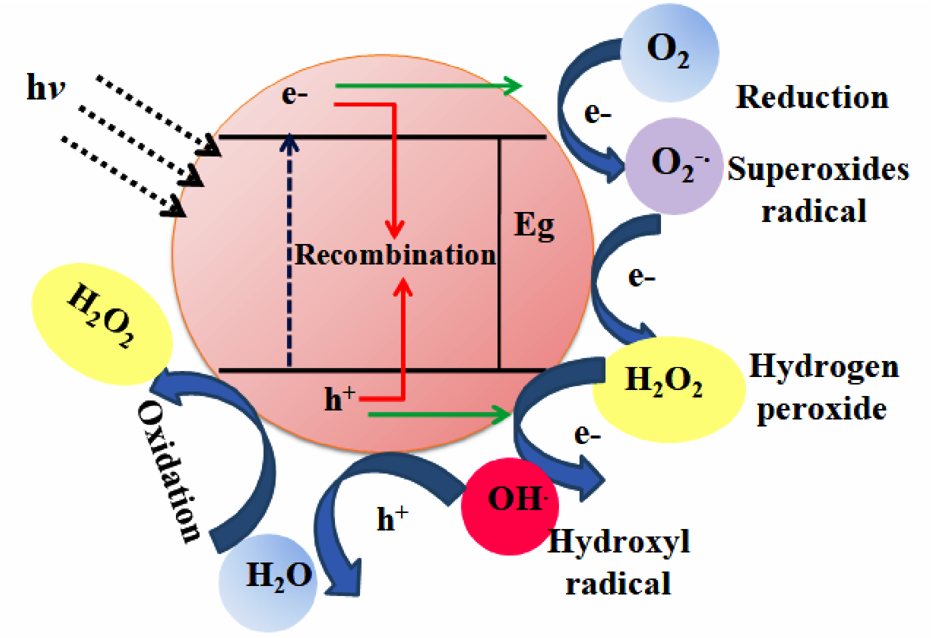

Fig. 1.2: Schematic representation for the basis of photocatalysis.

A large number of metal oxides have been examined as a photocatalyst for sustainable applications. Among all TiO_2, SiO_2 and MnO_2 have attracted great interest because of its unique properties and good thermal and chemical stability [12]. Absorption in UV-light and fast recombination of photoexcited charge carriers (e^-h^+) in TiO_2 and MnO_2 like bandgap (3.2, 1.6 eV), impair their application to a great extent [13]. Considerable efforts have been made to develop modified semiconductor photocatalysts that are capable of showing activity under visible light like:

- Metal loading

- Loading of metal oxides on the mesoporous material as clay, activated carbon, zeolites, silica etc
- Use of cationic and anionic surfactants as pore templates.

1.1.3 Carbon Quantum Dots (CQDs)

There are a variety of low dimensional semiconductors which include quantum wires, quantum wells, and quantum dots. Out of these quantum dots have gained extensive popularity for research nowadays [14]. Quantum dots are zero-dimensional structures in which electrons are delocalized along all three spatial dimensions leading to so-called the quantum confinement effect [15, 16]. Quantum confinement occurs when the size of nanocrystal becomes smaller than twice the Bohr radius and becomes weak when it exceeds Bohr radius. In semiconductor nanocrystals upon absorption of a photon with energy greater than the semiconductor band gap results in the generation of electron-hole pairs or excitons in which electrons and holes are bounded by electrostatic attraction. The average distance between an electron and hole in an exciton is of the order of Bohr radius. The optical and electrical properties of semiconductor nanocrystal become dependent upon its physical dimensions when its size approaches Bohr radius [17]. Luminescent semiconductor quantum dots exhibit remarkable photostability, broad absorption profiles, high quantum yields and stability against photobleaching. The size and shape controlled luminescent properties of quantum dots arising from quantum confinement effect allows implementation of the same material as an optical label for parallel analysis of different analytes. The narrow emission bands and large Stokes shifts in luminescence spectra of quantum dots enable effective coupling of emitted light to other fluorophores or quantum dots [18].

Recently, carbon quantum dots have gained interest due to their bright photoluminescence in visible spectra, high photostability, tunable excitation, and emission wavelengths. These are better than above-mentioned quantum dots due to their biocompatibility, nontoxic and eco-friendly nature. Hence, they possess immense scope in fields such as biological labeling, bioimaging, drug delivery and optoelectronic devices [19]. These new classes of zero-dimensional nanomaterials were accidentally obtained during purification of SWNTs in 2004. Since then they have attained a special status in the nanocarbon family [20]. Having size below 10 nm the quantum confinement effect and graphite-like sp^2 π bonds are highly prominent. The optical absorptions of the carbon quantum dots correspond to π-plasmon transition in the core of the dots whereas the fluorescence emissions from visible to near-IR are related to radiated recombination of trapped photogenerated electrons and holes at various surface sites. The carbon quantum dots tend to possess various surface active functional groups such as amino, epoxy, ether, carbonyl, hydroxyl, and carboxylic acids on their surface which results in high hydrophilicity and provide a path for functionalization with several organic, polymeric and biological species [21]. The fabrication of CQDs usually completes four stages to give fluorescent properties as clearly shown in Fig. 1.3.

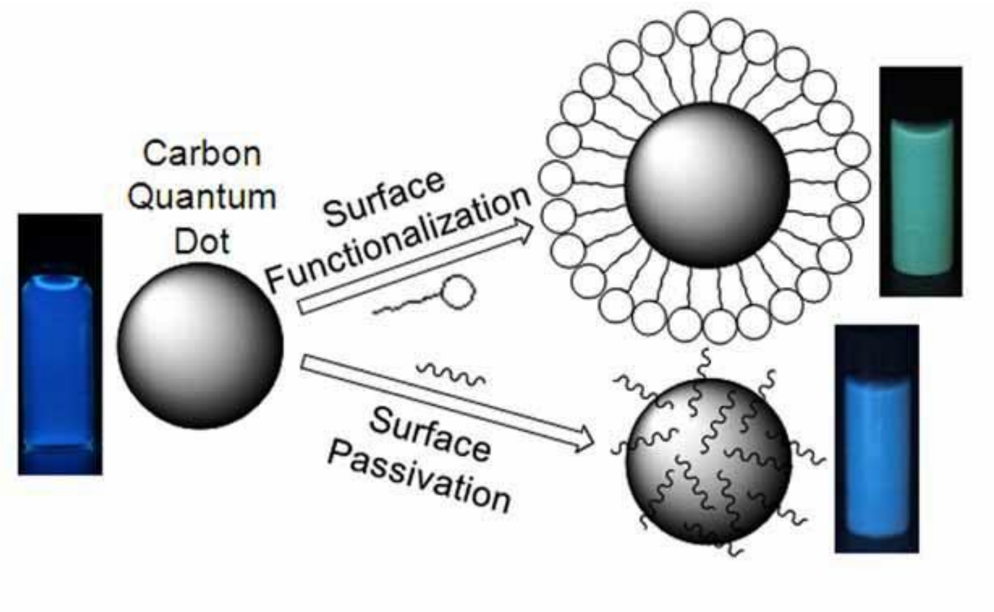

Fig. 1.3: Mechanism for the fabrication of fluorescence CQDs.

Considering the above-mentioned properties in combination with their broad absorption spectra and large absorption coefficients tend to make carbon dots as the most favorable candidates in contrast to rare and costly heavy metals in the field of photovoltaic, photocatalysis and in various environmental treatment applications.

1.1.4 Band gap tuning and sensitization of CQDs by Nobel metals

The interaction of metal and ligands have been credited as a driving source in assembling nanoparticles based sensors for high operability and selectivity in an aqueous medium. These metal NPs are known as excellent fluorescence quenchers and their quenching effect has been thoroughly explored on various fluorophores. In addition, these NPs have a huge number of applications in the field of sensing and catalysis [21-23]. Fluorescence quenching by the metal NPs is generally a type of energy transfer method taking place among the fluorophores and NPs. The composite formation of these metallic NPs with other active materials has been reported to be efficient in several advanced biomedical applications [24]. Commonly, these type of nanosensors are based on gathering nanoparticles with tailored functional groups that can selectively bind with the analyte, leading to 1D, 2D or 3D interparticle bridging assemblies. This technique results in optical tuning induced by short and long-range interactions of surface plasmon resonance (SPR) of individual nanoparticles. On the other side ligand displacement reactions, like an exchange of surface stabilizing agents by analytes with higher affinity for the nanoparticle surface could potentially be used for biological recognition events, if the specific marker of interest leads to interparticle cross-linking. Additionally, if the ligands exchange process could lead to enhancement of fluorescence inherent to the displaced surface stabilizing agents, then the nanosensor could function as a dual probe detector, both colorimetric and fluorometric, for the sensitive analysis of specific biomolecules and metal ions [25]. Some important reports on band gap tuning and surface modification of CQDs by different catalysts are summarized in Table 1.1.

Table 1.1: Band gap tuning and surface modification of CQDs by different analytes.

Analyte	**Advantages**	**Application**	**Reference**
Core-shell Au@CQDs	Band gap decreased from 2.78 eV to 2.68 eV	Photocatalytic hydrogen production	[26]
Core-shell silicon nanowire (SiNW) array/carbon quantum dot (CQD) core-shell	The heterojunction with a barrier height of 0.75 eV exhibited excellent rectifying behaviour	High-performance optoelectronic devices	[27]
Carbon nitride nanosheets (CNNS) /CQDs composites	Higher photocatalytic efficiency than the pure g-C_3N_4.	Photocatalytic hydrogen production	[28]
Carbon Quantum Dot/Silver Nanoparticle/Polyoxometalate Composites	SPR of Ag improves the solar-energy conversion efficiency	Overall Water Splitting in Visible Light.	[29]
Glutathione-Capped Quantum Dots(QDs)	Efficient surface and photophysical properties of the QDs	Pb^{2+} ion detection in water.	[30]
Nitrogen (N) and sulphur (S) doped carbon dots (NSCQDs)	Good luminescence, uniform size, excellent stability, and excitation-dependent photoluminescence (PL) property	Hg^{2+} ion detection in living cells.	[31]

T-rich- or C-rich-modified QDs	Specific quenching of the QDs by the ions enabled us to use Hg^{2+} and Ag^{+} ions as inputs that activate logic gates	Selective analysis of Hg^{2+} or Ag^{+} ions in water.	[32]
CdS QDs capped with l-cysteine	Water-soluble and highly stable in aqueous solution.	Detection of heavy and transition metal (HTM) ions in aqueous solution.	[33]
TiO_2/CQDs and SiO_2/CQDs complex system	Efficient usage of the full spectrum of sunlight	Photocatalytic degradation of methyl blue dye	[34]
CQDs/Bi_2WO_6 hybrid	Interfacial transfer of photogenerated electrons from Bi_2WO_6 to CQDs, leading to effective charge separation of Bi_2WO_6.	Photocatalytic degradation of organic pollutant.	[35]
Carbon Quantum Dot (CQD) Deposited Fe_3O_4@mTiO_2 Nano-Pom-Pom Balls	Expanding the light absorption of mTiO_2 from the UV to visible region.	Photodegradation for ciprofloxacin, methylene blue, quinalphos, and 4-nitrophenol under visible light	[36]
CdS-Bi_2WO_6/CQDs	Stronger absorption in the visible light region	Photodegradation of methyl orange	[37]

1.1.5 CQDs for Sustainable Development

Clean environment and energy are two basic needs for human survival and economic development. However, the rise in demand for various products has led the manufactures to indulge in risky but profitable production modes leading to long-term environmental threats. Also, the consumption of energy from fossil fuels such as coal, petroleum and natural gas has led to pollution of air and water bodies. The limited availability of fossil fuels and their increasing year wise and unregulated consumption can lead to energy crises in the future. Since the Kyoto protocol in 2005, these issues have emerged in the global scenario in a highly transparent fashion [38]. Formulation and implementation of an integrated set of policies addressing energy and environmental concerns simultaneously have lot of challenges in a developed nation such as USA. The present policies and techniques are ineffective in the realization of long-term goals [39]. In order to tackle the fossil fuel based energy crises and environmental pollution, there is a need for greener and sustainable source which can resolve both energy and environment-related issues. Nanotechnology can be a highly promising field for such a purpose. It is an emerging field which can contribute towards the development of smarter materials capable of both generating energy and degrading environmental pollutants. It deals with designing and manipulation of materials at the molecular scale. The rapid development of novel Nanomaterials can create options regarding new product innovation and high-performance applications. Fabrication of such novel functional materials with tunable sizes, shapes, crystallinity, porosity, and structures are of great importance for innovations in sustainable energy technologies [40]. It also allows fabrication of materials having specific functionalities capable of recognizing a particular pollutant in the mixture. Thus, tremendous progress in nanotechnology can lead to a basic understanding of physics at the nanoscale in order to control system properties and searching for new materials for energy and environmental applications. Low energy solution based synthesis of nanomaterials can allow their incorporation into devices. Among the nanomaterials photoactive metal oxide nanoparticles, quantum dots and carbon-based nanomaterials have potential candidature in this regard since they rely upon sunlight which itself is a clean and sustainable energy source. Quantum confinement effect in nanomaterials such as quantum dots has given rise to many of the fascinating optoelectronic features which make them highly eligible candidates for energy and environmental based applications [26]. Hence, such smart functional materials can be helpful in the development of clean energy source and also for water and air purification based devices. Carbon-based nanomaterials such as carbon quantum dots (CQDs) can play a significant role in this regard due to their unique optoelectronic properties. These carbon-based eco-friendly materials are being highly investigated nowadays for photovoltaic applications, water splitting and their ability to degrade harmful pollutants.

1.2 Research Gaps

Transition metal oxides show excellent performance in the photocatalytic area, which belongs to their large specific surface area, controllable structure, and their own special optical, electrical, magnetic properties. However, owing to the limitations of the synthetic method and low quantum yield due to lower activation energy in photocatalytic reactions, there exist some drawbacks which are discussed below:

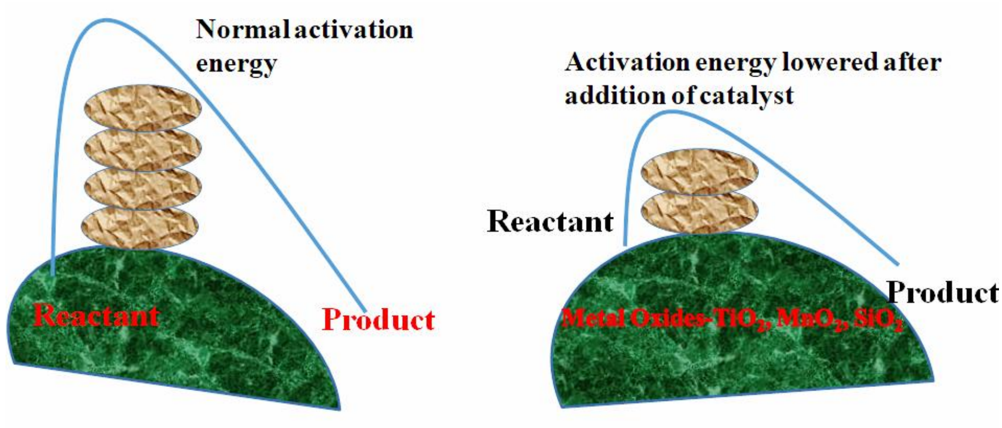

Fig. 1.4: Pictorial representation of lowering the activation energy in photocatalytic reactions.

- Poor structure controllability and broad particle size distribution, which are adverse to catalytic activity.
- Various types of transition metals own catalytic property, but the photodegradation efficiency is low due to lack of surface area.
- The existing synthesis methods for high surface area metal oxides are quite complicated and costly. So there is a need for a synthetic route which is very simple, reproducible and cost/time-effective.
- There is not much significant work done to explore the effect of metal doping on CQD for fluorescence turn-on/off detection of different biomolecules.

1.3 Objectives

- Synthesis and characterization of metal oxide nanostructures (TiO_2, SiO_2, MnO_2) and CQDs with different morphologies.
- Band gap tuning and sensitization of the metal oxide nanostructures and CQDs under visible/sun-light irradiation by noble metal (Au/Ag) loading.
- Catalytic application of as-prepared metal oxide nanocomposites and CQDs for sustainable developments and different organic transformation reactions (hydrolysis of nitriles/ reduction of nitrophenols) under visible and UV-light irradiation.

1.4 Techniques for Characterizations

After fine-tuning the final photocatalysts will undergo material characterization and the details are mentioned below in Table 1.2.

Table 1.2 Techniques for Characterizations

Characterization Technique	**Specifications**
UV-Vis spectroscopy	Absorption properties of nanoparticles were done both in dispersed and in the solid phase on Analytikjena Specord 205 (Germany) spectrophotometer (spectral range, 190-1100 nm).
X-ray diffraction analysis (XRD)	The faceted design, phase structural, unit cell properties and polymorphism were studied by X-ray diffraction with PANalytical Xpert Pro (Almelo, Netherlands) by Cu Kα at 1.54 A^o operating at 45 kV and the diffraction angle was set between 10-80^o with a scan speed of 5^o/min rise.
Transmission electron microscopy (TEM),	The morphology of samples was examined by Hitachi, 7500 model (Japan) TEM, operating at the voltage of 50-200 kV with the resolution of 2.4 A^o.
Field emission-SEM (FESEM)	The morphological characters like the shape and statistical distribution of particle size were examined on SU8-180 (Tokyo Japan)
Time-resolved spectroscopy (TRS)	The dynamics and lifetime of charge carriers (electrons and holes) were studied on Tektronix TDS-1012 TRS.
X-ray photoelectron spectroscopy (XPS)	The quantitative elemental composition, oxidation state, and surface chemistry were studied by XPS technique. The XPS was recorded on KRATOS Axis 165 (Shimadzu, UK) with Mg Kα radiation (1252.6 eV at 75 W).
Surface area analyzer (BET)	The N_2 adsorption-desorption based Brunner-Emmet-Teller (BET) equation and BEL mini-II, Micro Trac Corp. Pvt. Ltd (Tokyo, Japan) instrument was used for the determination of surface area of the catalysts.
Raman spectroscopy	The structural properties of the catalysts were elucidated by Raman spectroscopy recorded on the Renishaw system 2000 (100-800 cm^{-1}) using a He–Ne laser (514.5 nm) and Atrix (STR500) spectrometers
Potential voltage (I-V) characteristics	The potential voltage (I-V) characteristics of the Gold doped Carbon dots heterojunction were witnessed on KEITHLEY

	(4200-SCS) with ZYVEX S100 nanomanipulator
Fourier transform infrared spectroscopy (FTIR)	The functional groups present in catalysts were recorded on Carry 660 Agilent Technologies (USA).
Photoluminescence spectroscopy (PL)	The fluorescence properties of carbon dots were recorded on Perkin-Elmer (LS55).
Gas chromatography (GC)	The quantification of CO_2 and H_2 evolved during the reaction was examined by gas chromatography (GC, Nucon Ltd, India)

1.5 Photocatalytic Activity

The photocatalytic activity of nanostructures was performed by simple powder method under different irradiation sources. In this method, the photocatalytic activity of as-synthesized nanostructures was evaluated at room temperature under visible, sunlight and UV light irradiation. A 250 W halogen (tungsten) lamp will serve as the light source to provide visible light within a range of 400–1100 nm and Hg arc lamp (125 W) as UV source. The visible and UV source set up was extended above the reaction mixture for maximum illumination and better passage of light. The sunlight based experiments were performed in open air conditions; here the reaction tube will be kept in suitable dimensions to get maximum solar flux. The gas-tight Pyrex test tube (20 cm length and 2.2 cm diameter) containing water and photocatalyst was irradiated along one dimension under continuous stirring**.**

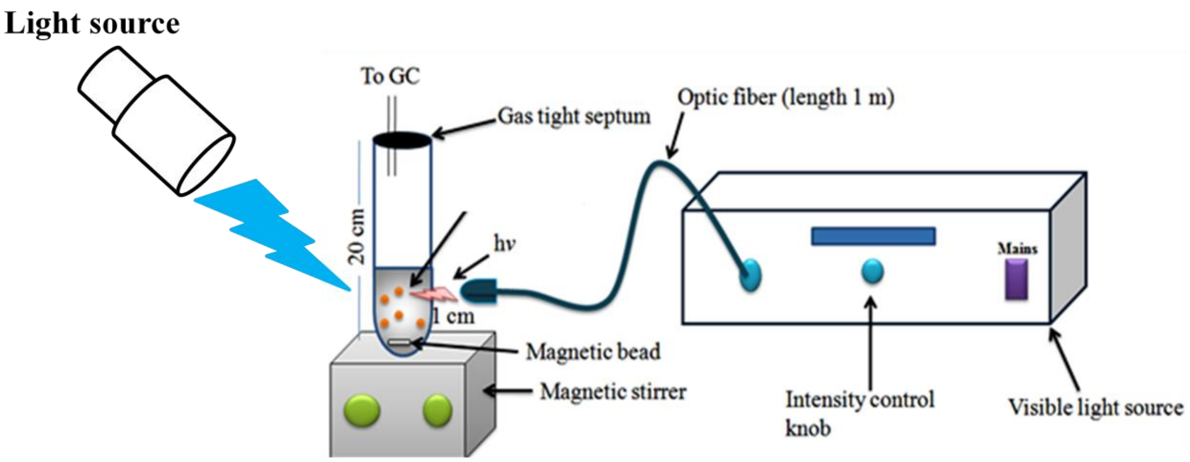

Fig. 1.5: Reaction setup for photocatalytic reactions.

References

1. Ravelli D, Dondi D, Fagnoni M, Albini A. Photocatalysis. A multi-faceted concept for green chemistry. Chemical Society Reviews. 2009;38(7):1999-2011.

2. Mills A, Le Hunte S. An overview of semiconductor photocatalysis. Journal of photochemistry and photobiology A: Chemistry. 1997 Jul 31;108(1):1-35.

3. Su J, Vayssieres L. A place in the sun for artificial photosynthesis?. ACS Energy Letters. 2016 May 23;1(1):121-35.

4. Kuznetsov VN, Serpone N. Visible light absorption by various titanium dioxide specimens. The Journal of Physical Chemistry B. 2006 Dec 21;110(50):25203-9.

5. Yu H, Shi R, Zhao Y, Waterhouse GI, Wu LZ, Tung CH, Zhang T. Smart utilization of carbon dots in semiconductor photocatalysis. Advanced Materials. 2016 Nov 1;28(43):9454-77.

6. Weinhold F. Chemistry: A new twist on molecular shape. Nature. 2001 May;411(6837):539.

7. Ono K, Austing DG, Tokura Y, Tarucha S. Current rectification by Pauli exclusion in a weakly coupled double quantum dot system. Science. 2002 Aug 23;297(5585):1313-7.

8. Kelsall R, Hamley IW, Geoghegan M, editors. Nanoscale science and technology. John Wiley & Sons; 2005 Nov 1.

9. Vanmaekelbergh D, Liljeroth P. Electron-conducting quantum dot solids: novel materials based on colloidal semiconductor nanocrystals. Chemical Society Reviews. 2005;34(4):299-312.

10. Daghrir R, Drogui P, Robert D. Modified TiO_2 for environmental photocatalytic applications: a review. Industrial & Engineering Chemistry Research. 2013 Feb 26;52(10):3581-99.

11. Varshney G, Kanel SR, Kempisty DM, Varshney V, Agrawal A, Sahle-Demessie E, Varma RS, Nadagouda MN. Nanoscale TiO_2 films and their application in remediation of organic pollutants. Coordination Chemistry Reviews. 2016 Jan 1;306:43-64.

12. Adeleye AS, Conway JR, Garner K, Huang Y, Su Y, Keller AA. Engineered nanomaterials for water treatment and remediation: Costs, benefits, and applicability. Chemical Engineering Journal. 2016 Feb 15;286:640-62.

13. Dong H, Zeng G, Tang L, Fan C, Zhang C, He X, He Y. An overview on limitations of TiO_2-based particles for photocatalytic degradation of organic pollutants and the corresponding countermeasures. Water research. 2015 Aug 1;79:128-46.

14. Kumar S, Nehra M, Deep A, Kedia D, Dilbaghi N, Kim KH. Quantum-sized nanomaterials for solar cell applications. Renewable and Sustainable Energy Reviews. 2017 Jun 1;73:821-39.

15. Berends AC, de Mello Donega C. Ultrathin One-and Two-Dimensional Colloidal Semiconductor Nanocrystals: Pushing Quantum Confinement to the Limit. The Journal of Physical Chemistry Letters. 2017 Aug 16;8(17):4077-90.

16. Fu H, Ji Z, Chen X, Cheng A, Liu S, Gong P, Li G, Chen G, Sun Z, Zhao X, Cheng F. A versatile ratiometric nanosensing approach for sensitive and accurate detection of Hg^{2+} and biological thiols based on new fluorescent carbon quantum dots. Analytical and bioanalytical chemistry. 2017 Mar 1;409(9):2373-82.

17. Bergren MR, Palomaki PK, Neale NR, Furtak TE, Beard MC. Size-dependent exciton formation dynamics in colloidal silicon quantum dots. ACS nano. 2016 Feb 5;10(2):2316-23.

18. Owen J, Brus L. Chemical Synthesis and Luminescence Applications of Colloidal Semiconductor Quantum Dots. Journal of the American Chemical Society. 2017 Jul 19;139(32):10939-43.

19. Dong Y, Cai J, You X, Chi Y. Sensing applications of luminescent carbon based dots. Analyst. 2015;140(22):7468-86.

20. Roy P, Chen PC, Periasamy AP, Chen YN, Chang HT. Photoluminescent carbon nanodots: synthesis, physicochemical properties and analytical applications. Materials Today. 2015 Oct 1;18(8):447-58.

21. Dimos K, Carbon quantum dots: Surface passivation and functionalization. Current Organic Chemistry. 2016 Mar 1;20(6):682-95.

22. Moores A, Goettmann F. The plasmon band in noble metal nanoparticles: an introduction to theory and applications. New Journal of Chemistry. 2006;30(8):1121-32.

23. Astruc D, Boisselier E, Ornelas C. Dendrimers designed for functions: from physical, photophysical, and supramolecular properties to applications in sensing, catalysis, molecular electronics, photonics, and nanomedicine. Chemical reviews. 2010 Mar 31;110(4):1857-959.

24. Thoniyot P, Tan MJ, Karim AA, Young DJ, Loh XJ. Nanoparticle–hydrogel composites: Concept, design, and applications of these promising, multi- functional materials. Advanced Science. 2015 Feb 1;2(1-2).

25. Kim HN, Ren WX, Kim JS, Yoon J. Fluorescent and colorimetric sensors for detection of lead, cadmium, and mercury ions. Chemical Society Reviews. 2012;41(8):3210-44.

26. Mehta A, Pooja D, Thakur A, Basu S. Enhanced photocatalytic water splitting by gold carbon dot core shell nanocatalyst under visible/sunlight. New Journal of Chemistry. 2017;41(11):4573-81.

27. Xie C, Nie B, Zeng L, Liang FX, Wang MZ, Luo L, Feng M, Yu Y, Wu CY, Wu Y, Yu SH. Core–shell heterojunction of silicon nanowire arrays and carbon quantum dots for photovoltaic devices and self-driven photodetectors. Acs Nano. 2014 Mar 31;8(4):4015-22.

28. Li K, Su FY, Zhang WD. Modification of g-C_3N_4 nanosheets by carbon quantum dots for highly efficient photocatalytic generation of hydrogen. Applied Surface Science. 2016 Jul 1;375:110-7.

29. Liu J, Zhang H, Tang D, Zhang X, Yan L, Han Y, Huang H, Liu Y, Kang Z. Carbon quantum dot/silver nanoparticle/polyoxometalate composites as photocatalysts for overall water splitting in visible light. ChemCatChem. 2014 Sep 1;6(9):2634-41.

30. Mohamed Ali E, Zheng Y, Yu HH, Ying JY. Ultrasensitive Pb^{2+} detection by glutathione-capped quantum dots. Analytical chemistry. 2007 Dec 15;79(24):9452-8.

31. Chandra S, Chowdhuri AR, Mahto TK, Laha D, Sahu SK. Sulphur and nitrogen doped carbon dots: A facile synthetic strategy for multicolour bioimaging, tiopronin sensing, and Hg2+ ion detection. Nano-Structures & Nano-Objects. 2017 Oct 1;12:10-8.

32. Freeman R, Finder T, Willner I. Multiplexed analysis of Hg^{2+} and Ag^{+} ions by nucleic acid functionalized CdSe/ZnS quantum dots and their use for logic gate operations. Angewandte Chemie International Edition. 2009 Oct 5;48(42):7818-21.

33. Chen J, Zheng A, Gao Y, He C, Wu G, Chen Y, Kai X, Zhu C. Functionalized CdS quantum dots-based luminescence probe for detection of heavy and transition metal ions in aqueous solution. Spectrochimica Acta Part A: Molecular and Biomolecular Spectroscopy. 2008 Mar 1;69(3):1044-52.

34. Li H, He X, Kang Z, Huang H, Liu Y, Liu J, Lian S, Tsang CH, Yang X, Lee ST. Water- soluble fluorescent carbon quantum dots and photocatalyst design. Angewandte Chemie International Edition. 2010 Jun 14;49(26):4430-4.

35. Di J, Xia J, Ge Y, Li H, Ji H, Xu H, Zhang Q, Li H, Li M. Novel visible-light-driven CQDs/Bi2WO6 hybrid materials with enhanced photocatalytic activity toward organic pollutants degradation and mechanism insight. Applied Catalysis B: Environmental. 2015 Jun 1;168:51-61.

36. Das RK, Kar JP, Mohapatra S. Enhanced photodegradation of organic pollutants by carbon quantum dot (CQD) deposited Fe_3O_4@ $mTiO_2$ Nano-Pom-Pom Balls. Industrial & Engineering Chemistry Research. 2016 May 12;55(20):5902-10.

37. Ge L, Liu J. Efficient visible light-induced photocatalytic degradation of methyl orange by QDs sensitized $CdS\text{-}Bi_2WO_6$. Applied Catalysis B: Environmental. 2011 Jun 22;105(3-4):289-97.

38. Chen DH, Chen CJ. Formation and characterization of Au–Ag bimetallic nanoparticles in water-in-oil microemulsions. Journal of Materials Chemistry. 2002;12(5):1557-62.

39. Hutchison JE. The road to sustainable nanotechnology: Challenges, progress and opportunities.

40. Liu CJ, Burghaus U, Besenbacher F, Wang ZL. Preparation and characterization of nanomaterials for sustainable energy production.

CHAPTER 2

Gold Nanoparticles Grafted Mesoporous Silica: A Highly Efficient and Recyclable Heterogeneous Catalyst for Reduction of 4-Nitrophenol

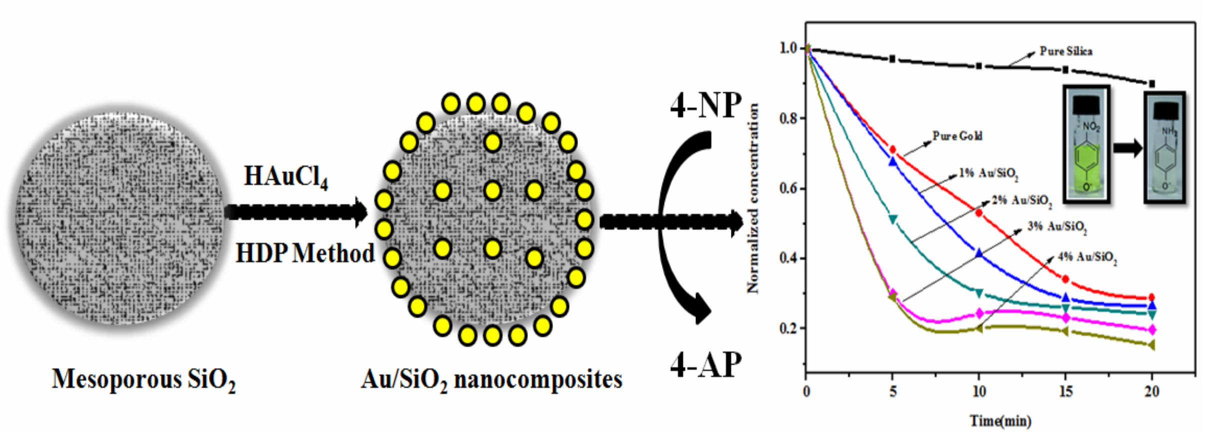

Highlights

- Microwave-assisted technique favoured the formation of SBA-15/SiO_2 nanocomposites with varied Silica and Titania precursor content.
- Photodegradation of organic dyes and pollutants by these nanocomposites were compared with commercially available SiO_2-P25 (Degussa).
- The reusability of the catalysts exhibited more than 98% conversion of the photodegradation of organic dyes and pollutants even after 10 consecutive cycles.

2.1 Introduction

A new class of materials, based on nanoparticles (NPs) in the composition of semiconductors (TiO_2, ZnO etc.) and dielectrics (SiO_2, Al_2O_3 etc.) substantially extends the range of their several applications, particularly in heterogeneous catalysis, in the creation of electronic devices, chemical sensors, protecting coatings, bactericidal materials, for surface-enhanced Raman scattering, etc [1-3]. It is very much important to develop methods for the synthesis of systems based on NPs/metal oxide and to investigate the nature of the interaction of NPs with the oxide matrix. Gold was initially regarded as useless in catalysis until Haruta *et al.* found that small Au NPs supported on reducible oxide supports can be highly active for CO oxidation reaction [4-5]. This finding triggered a great deal of interest in exploring the application of Au catalysts in other reactions [6], such as organic catalysis [7]. The Au/support interface is a model of a metal-insulator or metal-semiconductor junction bearing unique size-dependent electronic properties, which could play an essential role in the foundation of the high catalytic activity. For this reason, the specific support materials should play an important role in the catalytic behavior of gold [8]. The nature of the active species is still being discussed. It has been suggested that the role of the oxide support is the stabilization of the gold NPs, and that the catalysis reaction takes place on the gold surface. In recent year, $mSiO_2$ have attracted much attention due to their attractive properties such as high surface area, uniform pore size, large pore volume, high thermal stability, controllable morphology, and facile surface functionalization. Silica is used as a support because of its inert character, which allows the investigation of the effect of the metal, minimizing the effect of the metal-support interaction. The weak interaction between SiO_2 surfaces and Au particles makes silica supports very convenient for their catalytic activity, minimizing the disturbance of the support interaction [9].

Extensive research work, both in fundamental and in applied catalysis has been carried out in order to understand the catalytic properties of gold nanoparticles supported on SiO_2, prepared by homogeneous deposition-precipitation (HDP) method using urea as the precipitating agent [10]. It is well established that the catalytic activity of supported Au NPs depends on the particle size, the nature of support and the preparation method. The present investigation deals with a direct correlation study between metal dispersion, metal area and catalytic reduction of 4-nitrophenol (4-NP) as a model reaction. In recent years, the reduction of 4-nitrophenol to 4-aminophenol (4-AP) by borohydride in aqueous solution has become such a model reaction that meets all criteria of a model reaction. It can be monitored easily with high precision by UV−Vis spectroscopy and High-performance liquid chromatography. This is due to the fact that 4-NP has a strong absorption at 400 nm and the decay of this peak can be measured precisely as the function of time [10].

This work has allowed us to draw clear conclusions regarding the behaviour of Au/SiO_2 for (i) the quantitative influence of particle composition; (ii) the role of particle size; and (iii) the influence of the support on catalytic reduction of 4-NP. The structural features of Au/SiO_2 catalysts were investigated by X-ray diffraction (XRD), CO-chemisorption, Brunauer–Emmet–Teller (BET), nitrogen adsorption-desorption and BJH pore size distribution (PSD), transmission electron microscopy (TEM), and X-ray photoelectron spectroscopy (XPS).

2.2 Experimental

2.2.1 Preparation of Au/SiO_2 catalysts

The Au/SiO_2 catalysts with different Au loading (wt%) were prepared by HDP method using urea as the precipitating agent [11]. The mixture of an aqueous solution containing $HAuCl_4.3H_2O$ (Sigma–Aldrich, 99.8%) and urea was stirred with gradual heating to a temperature up to 95 °C for 6 h. Urea decomposes to ammonia and hence the precipitation occurs in a homogeneous way as the pH shifts towards basic conditions (pH ~ 6–8). Subsequently, the support (commercial origin Aldrich, SiO_2) was added to the above solution with continuous stirring. The requisite amount of 0.1 M freshly prepared $NaBH_4$ aqueous solution [12] was added to the above solution so as to precipitate metallic Au nanoparticles on SiO_2 support. The solid product formed was filtered, washed thoroughly with deionized water until the filtrate contained no chloride ions (confirmed with the $AgNO_3$ test) and subsequently dried in a hot air oven for 5 h and finally calcined at 400 °C for 3 h in the N_2 atmosphere. The EDAX–analysis suggest that the concentration of sodium is present in a negligible amount (<0.01%).

2.2.2 Catalyst characterization

X-ray powder diffraction (XRD) patterns of the catalysts were recorded on a Rigaku Miniflex (M/s. Rigaku Corporation, Japan). X-ray diffractometer using Ni-filtered Cu Kα radiation ($\lambda = 0.15406$ nm) with a scan speed of 2° min^{-1} and a scan range of 10 – 80° for wide angle diffraction at 30 kV and 15 mA. The crystallite size of Au is calculated by using the Debye–

Scherrer equation and phase identification with the help of the JCPDS files. The CO–chemisorptions measurements were carried out on Auto-Chem 2910 (Micromeritics, USA) instrument. A 100 mg of the catalyst was pre-treated with He gas for 1 h at 150 °C. The sample was subsequently cooled to 50 °C in the same He gas stream. CO uptake was determined by injecting pulses of 10% CO/He from a calibrated online sampling valve into the He gas stream passing over the samples at 80 °C. Metal area, metal dispersion and metal average particle size were calculated assuming the stoichiometric factor (CO/Au) as 1. Adsorption was deemed to be completed after three successive runs showed similar peak area. Gold content was determined by inductively coupled plasma optical emission spectrometer (ICP–OES) on a Varian 720–ES instrument. Solid samples were first digested in a mixture of HF, HCl, and HNO_3 in a microwave oven for 2 h and further diluted with deionized water to analyze the gold contents by ICP-OES. ICP analysis, performed on the fresh samples of Au/SiO_2 catalysts. The BET surface areas of the catalysts were obtained from N_2 adsorption-desorption isotherms (Autosorb 1 - Quantachrome instruments, USA at –196 °C). The samples were first degenerated at 300 °C to ensure a clean surface prior to construction of adsorption isotherm. The Barrett–Joyner–Halenda (BJH) method was used to calculate the pore–size distribution from the desorption branch of the isotherm (Autosorb 1-Quantachrome, USA). Transmission electron microscopy (TEM) images of the catalysts were obtained using a Technai-12, FEI, Netherlands at an accelerating voltage of 120 kV. The specimens were prepared by dispersing the samples in methanol using an ultrasonic bath and evaporating a drop of resultant suspension onto the carbon coated copper grid. X-ray photoelectron spectroscopy (XPS) was used to study the chemical composition and oxidation state of catalyst surfaces. The XPS spectra of the catalysts were measured on an XPS spectrometer (KRATOS Axis 165, Shimadzu, UK) with Mg Kα radiation 1253.6 eV at 75 W. The gold 4f core-level spectra were recorded and the corresponding binding energies referenced to the C 1s line at 284.6 eV (accuracy within (0.2 eV)). The background pressure during the data acquisition was kept below 10^{-9} Torr.

2.2.3 Catalytic activity

The catalytic reduction process of 4-NP was monitored by HPLC (Thermofischer C-18, solvent system water: methanol, 30:70) at 254 nm wavelength and also by UV–Vis absorption spectra. Initially, 0.375 mL of 0.2 M freshly prepared $NaBH_4$ solution was added to a solution containing 0.0375 mL of 0.005 M 4-NP and 1.65 mL of deionized water. At this stage, the 4-nitrophenol was converted into 4-nitrophenolate anion. After that, the 5 mg of catalyst was added and the reaction was spectrophotometrically monitored at 400 nm for different time intervals. A gradual change of the solution color from bright yellow to colorless was observed during the reaction. In a similar pattern, the study was carried out for a different catalyst with varying ratio of gold in Au/SiO_2 catalyst. The peaks of a different solution of 4-NP are compared with trisodium citrate-capped pure Au NPs and commercially available SiO_2 in order to assure the catalytic properties of prepared samples.

2.**3 Results and Discussion**

2.3.1 Characterization of catalysts

2.3.1.1 X-ray diffraction (XRD) analysis

The broad XRD diffraction peak at 2θ ~ 22° (Fig. 2.1) are observed for all the Au/SiO_2 catalysts due to the amorphous silica framework of SiO_2 support [13]. After Au loading the Au/SiO_2 catalysts exhibits four diffraction peaks at 2θ ~ 38.2°, 44.6°, 64.9°, 77.9° which are indexed to (111), (200), (220), and (311) planes of metallic Au respectively (JCPDS-ICDD Card No. 01-1172), the unit cell structure shows compatibility with face-centered cubic lattice (fcc) [14-17]. A considerable increase in the line widths, with varying gold content (1.0 – 4.0 wt %) is a feature arising due to a decrease in particle size. The peaks are sharp and intense indicating good crystallinity of metallic Au^0. The crystallite size of gold was calculated from the diffraction peak (111), by applying the Debye-Scherrer formula and is reported in Table 2.1.

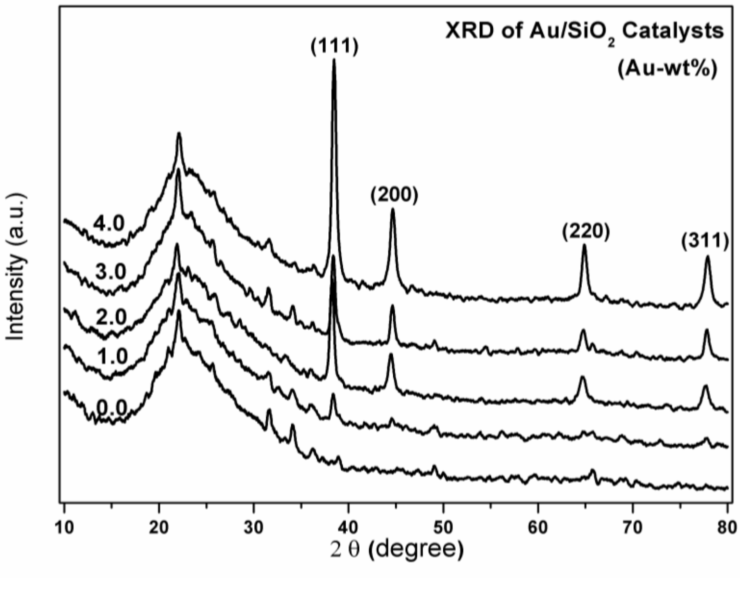

Fig. 2.1: Powder XRD patterns of SiO_2 and various wt% Au/SiO_2 catalysts.

2.3.1.2 CO-chemisorption analysis

The physicochemical properties of Au/SiO_2 catalysts such as dispersion, metal area, and particle size were determined from CO–chemisorption. It is observed that the increase in CO uptake with an increase in metal loading leads to be an increase in particle size (Fig. 2.2). This suggests to the agglomeration of gold particles at higher metal loading. This agglomeration in turn leads to the decrease in metal dispersion and increase in particle size [29].

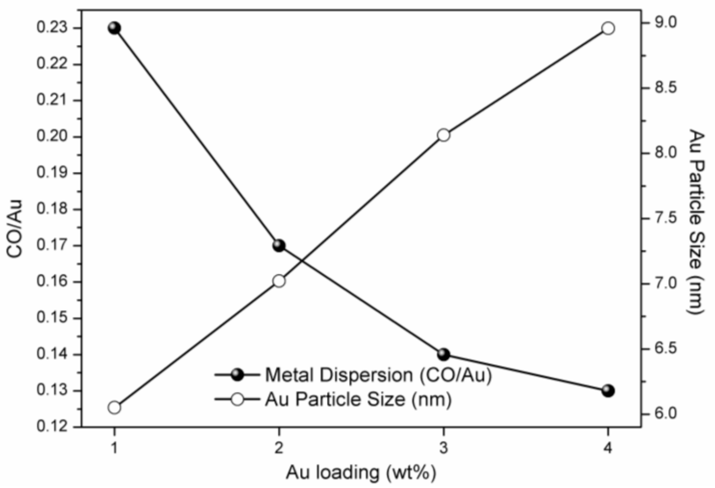

Fig. 2.2: Effect of CO–chemisorption properties on Au (wt %) loadings**.**

2.3.1.3 BET surface area and pore size distribution (PSD) studies

The N_2 adsorption/desorption is a standard method to characterize porous materials, which can provide information about the surface area, average pore diameter and pore volume of the catalysts. The surface area decreases with the increase in Au content ascribed to the incorporation of Au into the pores of the support as evidenced from pore size distribution measurements. Fig. 2.3(a) show the N_2 adsorption/desorption isotherms & Barrett Joyner Halenda (BJH) pore size distribution of bare supports (SiO_2), and various supported Au catalysts (Au/SiO_2). Pure SiO_2 support shows the presence of mesoporous nature with the average pore diameters in the range of ~17 nm. The addition of gold to SiO_2 has a significant effect on the isotherms, and pore size distribution. A well-defined step occurs in P/P_0 range of 0.6–0.8 represents the spontaneous filling of the mesopores due to capillary condensation, which is also evidenced by the BJH distribution (Fig. 2.3(b)). All the samples exhibit Langmuir type-IV isotherms which is a characteristic feature of mesoporous materials [18-

19]. The nitrogen adsorption isotherms of SiO_2 and Au/SiO_2 catalysts exhibit H_2–type hysteresis loop corresponding to pores with narrow necks and wider bodies [20] and features a sharp step in the P/P_0 range of 0.65–0.95, the sharpness of this step is indicative of the uniformity of the pore size [19] The calcination temperature of 400 °C in the SiO_2 sample is really important to lead to a better mesoporous structure formation. The mean pore diameter of SiO_2 and Au/SiO_2 catalysts are obtained by the BJH method from the corresponding adsorption-desorption data as reported in Table 2.1. The obtained specific surface areas are in agreement with those reported by other authors [21].

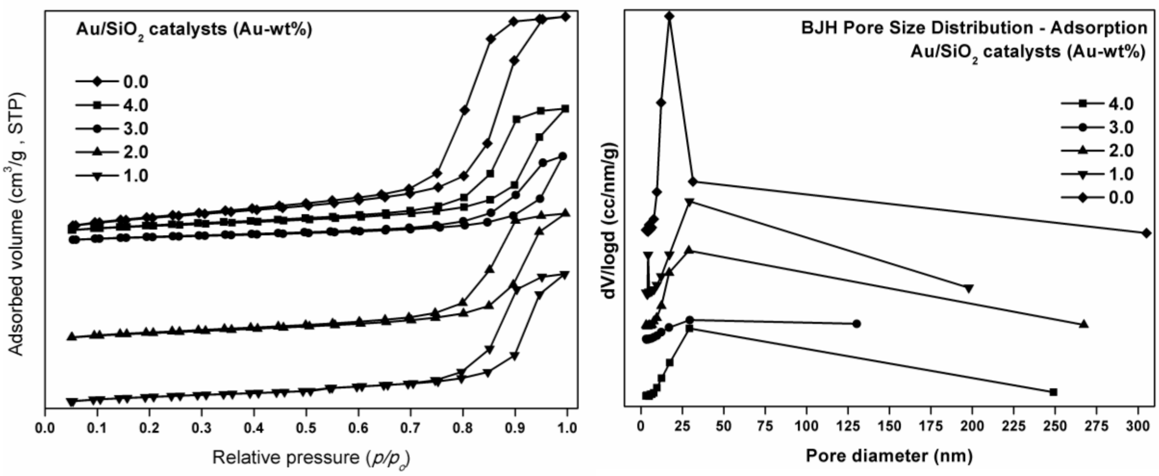

Fig. 2.3: (a) N_2 adsorption-desorption isotherms for SiO_2 and various wt% Au/SiO_2 catalysts (b) BJH pore size distribution for SiO_2 and various wt% Au/SiO_2 catalysts.

2.3.1.4 Transmission electron microscopy (TEM) analysis

Transmission electron microscope is a powerful technique to investigate the particle size of metal NPs on catalytic support. The gold NPs are spherical in shape and are uniformly dispersed and confined to the channels of the SiO_2 (Fig. 2.4). The corresponding histogram shows the distribution of gold particles on SiO_2. The mean diameter of Au particles is found to be ~ 6–10 nm while the average crystallite size of Au particles was obtained to be ~ 7–11 nm from XRD results.

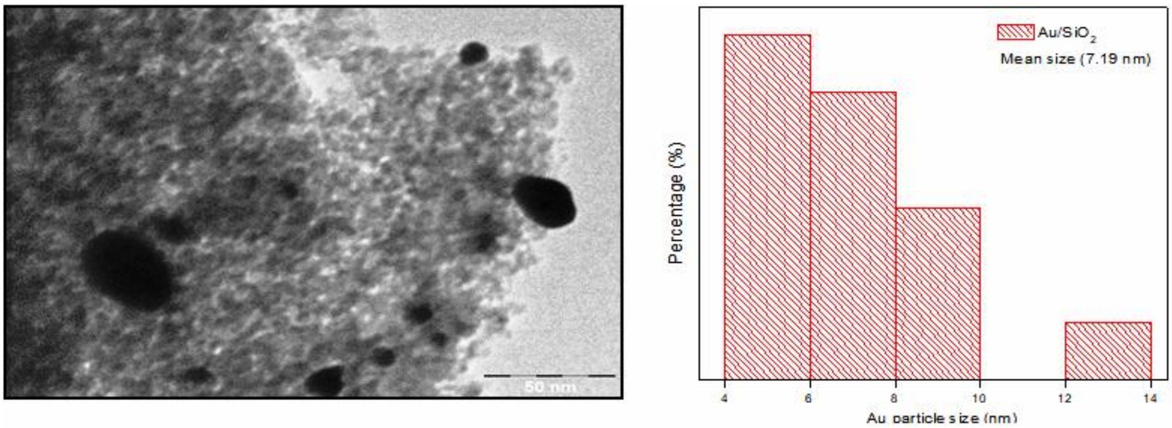

Fig. 2.4: TEM image and histogram comparing the Au particle size distribution of 4wt% Au/SiO$_2$ catalyst.

2.1.5 X-ray photoelectron spectroscopy (XPS) analysis

In order to verify the oxidation states of gold element in as-synthesized Au/SiO$_2$ catalysts were investigated by XPS. The high resolution XPS spectrum (Fig. 2.4) shows binding energy of Au 4f$_{7/2}$ at 84.0 and Au 4f$_{5/2}$ at 87.7 eV, which are significantly different from Au$^+$ 4f$_{7/2}$ (84.6 eV) and Au^{3+} 4f$_{7/2}$ (87.0 eV). The result suggests that the gold species is in the metallic state [23] and these binding energy values correspond to the metallic gold particles [24]. However, the XPS results confirmed the absence of any contamination from sodium and chlorine species [12]. These results further confirm that gold NPs on the surface of SiO$_2$ support are in zero valence state. The XPS spectra of the present investigation did not show any peaks corresponding to the binding energies at 84.6 eV (4f$_{7/2}$) and 87.0 eV (4f$_{7/2}$) due to the cationic form of Au$^+$ and Au^{+3} oxidation states respectively. This suggests that the formation of gold NPs takes place on the surface of the SiO$_2$ support.

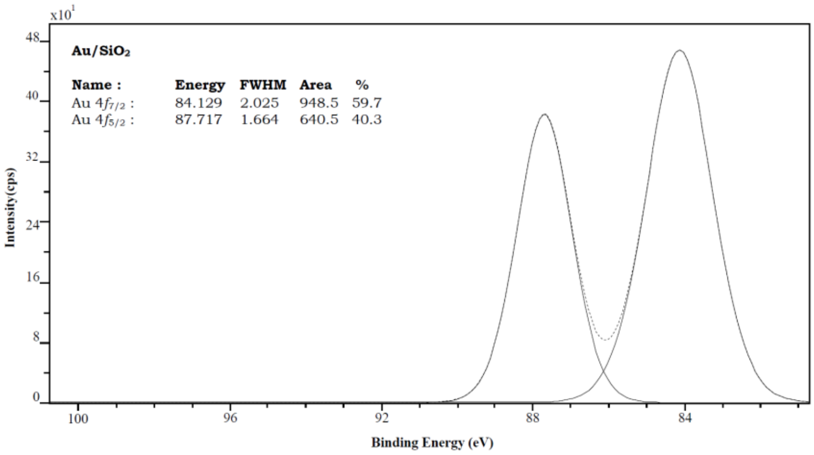

Fig. 2.4: XPS spectrum of 4wt% Au/SiO$_2$ catalyst.

Table 2.1 Textural properties of SiO_2 and various Au/SiO_2 catalysts.

Au (wt %)	**Au content (wt %)[a]**	**S_{BET} (m^2/g)**	**V_t (cc/g)**	**D_{BJH} (nm)**	**Binding Energy (eV)**		**Rate of Reaction[b]**
					$4f_{5/2}$	**$4f_{7/2}$**	
0.0	0.00	450	0.82	17.11	-	-	-
1.0	0.89	421	0.77	28.83	87.721	84.138	0.0375
2.0	1.65	402	0.75	29.22	87.717	84.129	0.0439
3.0	2.43	395	0.74	29.31	87.671	83.911	0.0532
4.0	3.34	385	0.69	29.46	87.658	83.891	0.0979

[a] Au content measured by ICP-OES; S_{BET} : BET surface area; V_t : total pore volume; D_{BJH} : average pore diameter calculated by BJH method; Binding Energy (eV) was determined by XPS.

[b] Rate of Reaction on the basis of mmol gold on the surface of SiO_2.

2.3.2 Catalytic reduction of 4-nitrophenol over Au/SiO_2 nanocomposites catalysts

The catalytic activity of as-prepared Au/SiO_2 nanocomposites was confirmed through reduction of 4-NP in the presence of sodium borohydride as a reductant. Nitrophenol is one of the water pollutants having high toxicity and is of great environmental concern [25]. Due to electron withdrawing nitro group in 4-NP it is resistant to chemical, biological oxidation, and hydrolysis. After the addition of Au/SiO_2 as a catalyst, the reduction of 4-NP started immediately, and the colour of the reaction solution became lighter. As shown in Fig. 2.5, the HPLC quantification data of Au/SiO_2 (4wt%) confirms the conversion (70%) of 4-NP (tR=3.6 min) to 4-AP (tR=2.9 min) for 15 min. With time the catalytic reaction increases and attain 98% concentration change of 4-NP (Fig. 2.6) [26]. In order to compare the catalytic activity of trisodium citrate-capped pure Au NPs a linear relationship between normalized concentration (C/Co) and reaction time was derived with as-prepared samples.

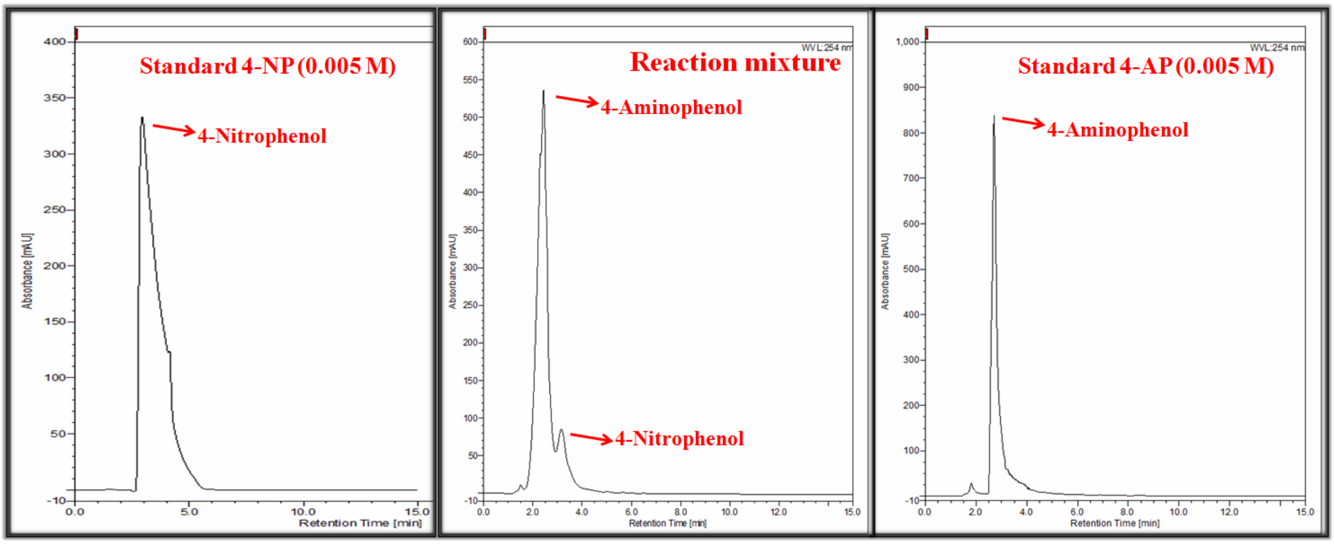

Fig. 2.5: HPLC Chromatogram of standard 4-nitrophenol, 4-aminophenol and reaction mixture.

The catalytic activities of different Au loading on Au/SiO_2 sample are found to have higher activity than that of trisodium citrate-capped pure Au NPs and pure Silica as shown in Fig. 2.6. In this model catalytic reaction, Au/SiO_2 catalysts exhibit good catalytic activity, because the mSiO_2 shells prevent the gold cores from undergoing aggregation. These activity results suggest that 4wt% Au/SiO_2 catalysts are found to be the best catalyst for the reduction of 4-NP to 4-AP in our present investigation.

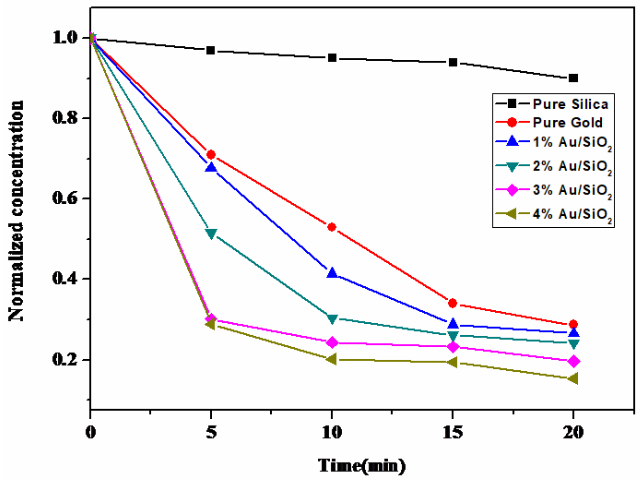

Fig. 2.6: Plot of normalized concentration(C/C_O) of 4-NP against reaction time in the presence of different wt% Au/SiO_2 nanocomposites.

In literature, there are few reports which represent the synthesis and enhanced photocatalytic activity of Au/SiO_2 nanocomposites [27-28]. So in comparison with other SiO_2 nanocomposites our catalyst has satisfactory photocatalytic activity due (Table 2.2) to high dispersion of Au into SiO_2 through HDP method. The catalytic activity was well correlated with the particle size of gold on SiO_2 supports. The 1, 2 and 3wt% Au/SiO_2 catalysts exhibit low catalytic activity compared to 4wt% Au/SiO_2 catalyst and it can be attributed to the decrease in the number of active sites of gold on SiO_2 due to agglomeration of gold NPs as evidenced from XRD, TEM and CO–chemisorption results.

In, heterogeneous catalytic reaction, reusability of the catalyst is one of the most important factors nowadays. Due to difficulties in the separation of the catalyst after reaction, there are limited numbers of experiments which are based upon reusability studies. Present catalysts are easily separable from the reaction solution and also it is well dispersible under stirring. There was no permanent adsorption of reactants over the catalyst, so it is very simple to separate the catalyst from the 4-aminophenol solution by the centrifugation process. Regeneration of 4wt% Au/SiO_2 catalyst was done after each reaction, by centrifugation and further washing with water. The catalytic activity of the catalyst remains approximately constant even up to ten consecutive experiments (Fig. 2.7).

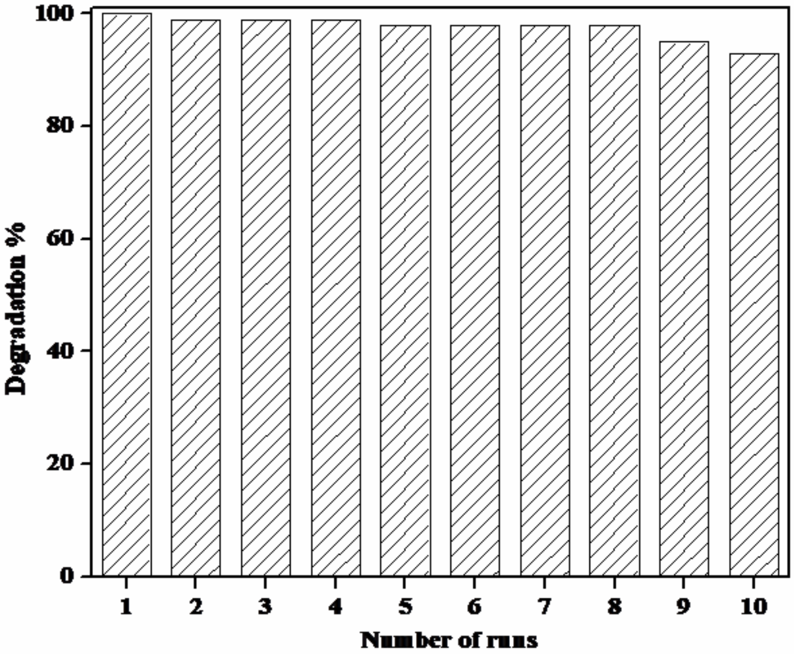

Fig. 2.7: Reusability data over 4wt% Au/SiO_2 for the catalytic reduction of 4-NP to 4-AP.

Table 2.2: Comparison of an overall reduction of 4-nitrophenol to 4-aminophenol from present work with recently reported in the literature.

Catalysts	**4-Nitrophenol amount (µL)**	**Amount of catalyst (mg)**	**Reduction Time (min)**	**References**
Fe@Au core-shell	25.0	3.0	20	[27]
Au immobilized in polyelectrolyte	100.0	8.0	20	[28]
Au/SiO_2	37.5	5.0	20	Present Work

References

1. Zhang Q, Ge J, Goebl J, Hu Y, Lu Z, Yin Y. Rattle-type silica colloidal particles prepared by a surface-protected etching process. Nano Research. 2009 Jul 1;2(7):583-91.
2. Kim YH, Lee DK, Cha HG, Kim CW, Kang YS. Synthesis and characterization of antibacterial Ag− SiO_2 nanocomposite. The Journal of Physical Chemistry C. 2007 Mar 8;111(9):3629-35.
3. Schubert MM, Hackenberg S, Van Veen AC, Muhler M, Plzak V, Behm RJ. CO oxidation over supported gold catalysts—"Inert" and "active" support materials and their role for the oxygen supply during reaction. Journal of Catalysis. 2001 Jan 1;197(1):113-22.
4. Haruta M, Yamada N, Kobayashi T, Iijima S. Gold catalysts prepared by coprecipitation for low-temperature oxidation of hydrogen and of carbon monoxide. Journal of catalysis. 1989 Feb 1;115(2):301-9.
5. Haruta M, Tsubota S, Kobayashi T, Kageyama H, Genet MJ, Delmon B. Low-temperature oxidation of CO over gold supported on TiO_2, α-Fe_2O_3, and Co_3O_4. Journal of Catalysis. 1993 Nov 1;144(1):175-92.
6. Takei T, Akita T, Nakamura I, Fujitani T, Okumura M, Okazaki K, Huang J, Ishida T, Haruta M. Heterogeneous catalysis by gold. InAdvances in catalysis 2012 Jan 1 (Vol. 55, pp. 1-126). Academic Press.
7. Stratakis M, Garcia H. Catalysis by supported gold nanoparticles: beyond aerobic oxidative processes. Chemical Reviews. 2012 Jun 12;112(8):4469-506.
8. Guczi L, Petö G, Beck A, Frey K, Geszti O, Molnár G, Daróczi C. Gold nanoparticles deposited on SiO_2/Si (100): Correlation between size, electron structure, and activity in CO oxidation. Journal of the American Chemical Society. 2003 Apr 9;125(14):4332-7.
9. Eremenko AM, Smirnoval NP, Mukhal IP, Yashan HR. Silver and gold nanoparticles in silica matrices: synthesis, properties, and application. Theoretical and Experimental Chemistry. 2010 Jul 1;46(2):65-88.
10. Amezquita- Garcia HJ, Razo- Flores E, Cervantes FJ, Rangel- Mendez JR. Anchorage of anthraquinone molecules onto activated carbon fibers to enhance the reduction of 4- nitrophenol. Journal of Chemical Technology and Biotechnology. 2015 Sep 1;90(9):1685-91.

11. Kumar A, Kumar VP, Vishwanathan V, Chary KV. Synthesis, characterization, and reactivity of Au/MCM-41 catalysts prepared by homogeneous deposition–precipitation (HDP) method for vapor phase oxidation of benzyl alcohol. Materials Research Bulletin. 2015 Jan 1;61:105-12.
12. Vadakkekara R, Chakraborty M, Parikh PA. Hollow mesoporous silica spheres supported Ag and Ag–Au catalyzed reduction of 4-nitrobenzo-15-crown. Journal of Industrial and Engineering Chemistry. 2014 May 25;20(3):767-74.
13. Yu X, Wang M, Li H. Study on the nitrobenzene hydrogenation over a Pd-B/SiO_2 amorphous catalyst. Applied Catalysis A: General. 2000 Jul 31;202(1):17-22.
14. Chi Y, Yuan Q, Li Y, Tu J, Zhao L, Li N, Li X. Synthesis of Fe_3O_4@ SiO_2–Ag magnetic nanocomposite based on small-sized and highly dispersed silver nanoparticles for catalytic reduction of 4-nitrophenol. Journal of colloid and interface science. 2012 Oct 1;383(1):96-102.
15. Chen Y, Wang H, Liu CJ, Zeng Z, Zhang H, Zhou C, Jia X, Yang Y. Formation of monometallic Au and Pd and bimetallic Au–Pd nanoparticles confined in mesopores via Ar glow-discharge plasma reduction and their catalytic applications in aerobic oxidation of benzyl alcohol. Journal of catalysis. 2012 May 1;289:105-17.
16. Sareen S, Mutreja V, Pal B, Singh S. Homogeneous dispersion of Au nanoparticles into mesoporous SBA-15 exhibiting improved catalytic activity for nitroaromatic reduction. Microporous and Mesoporous Materials. 2015 Jan 15;202:219-25.
17. Kumar A, Sreedhar B, Chary KV. Highly dispersed gold nanoparticles supported on SBA-15 for vapor phase aerobic oxidation of benzyl alcohol. Journal of nanoscience and nanotechnology. 2015 Feb 1;15(2):1714-24.
18. Forryan CL, Lawrence NS, Rees NV, Compton RG. Voltammetric characterisation of the radical anions of 4-nitrophenol, 2-cyanophenol and 4-cyanophenol in N, N-dimethylformamide electrogenerated at gold electrodes. Journal of Electroanalytical Chemistry. 2004 Jan 1;561:53-65.
19. Zhao Y, Wang H, Zhao Y, Shen J. Preparation of a novel sulfonated carbon catalyst for the etherification of isopentene with methanol to produce tert-amyl methyl ether. Catalysis Communications. 2010 Apr 30;11(9):824-8.
20. Yu JG, Su YR, Cheng B. Template- free fabrication and enhanced photocatalytic activity of hierarchical macro- /mesoporous titania. Advanced Functional Materials. 2007 Aug 13;17(12):1984-90.

21. Flego C, Carluccio L, Rizzo C, Perego C. Synthesis of mesoporous SiO_2–ZrO_2 mixed oxides by sol–gel method. Catalysis Communications. 2001 May 1;2(2):43-8.
22. Du M, Zhan G, Yang X, Wang H, Lin W, Zhou Y, Zhu J, Lin L, Huang J, Sun D, Jia L. Ionic liquid-enhanced immobilization of biosynthesized Au nanoparticles on TS-1 toward efficient catalysts for propylene epoxidation. Journal of catalysis. 2011 Oct 27;283(2):192-201.
23. Zwijnenburg A, Goossens A, Sloof WG, Craje MW, van der Kraan AM, Jos de Jongh L, Makkee M, Moulijn JA. XPS and Mössbauer characterization of Au/TiO_2 propene epoxidation catalysts. The Journal of Physical Chemistry B. 2002 Sep 26;106(38):9853-62.
24. Kumar A, Kumar VP, Kumar BP, Vishwanathan V, Chary KV. Vapor phase oxidation of benzyl alcohol over gold nanoparticles supported on mesoporous TiO_2. Catalysis letters. 2014 Aug 1;144(8):1450-9.
25. Chen J, Zhang R, Han L, Tu B, Zhao D. One-pot synthesis of thermally stable gold@ mesoporous silica core-shell nanospheres with catalytic activity. Nano research. 2013 Dec 1;6(12):871-9.
26. Zhao P, Feng X, Huang D, Yang G, Astruc D. Basic concepts and recent advances in nitrophenol reduction by gold-and other transition metal nanoparticles. Coordination Chemistry Reviews. 2015 Mar 15;287:114-36.
27. Gupta VK, Atar N, Yola ML, Üstündağ Z, Uzun L. A novel magnetic Fe@ Au core–shell nanoparticles anchored graphene oxide recyclable nanocatalyst for the reduction of nitrophenol compounds. Water research. 2014 Jan 1;48:210-7.
28. Wunder S, Polzer F, Lu Y, Mei Y, Ballauff M. Kinetic analysis of catalytic reduction of 4-nitrophenol by metallic nanoparticles immobilized in spherical polyelectrolyte brushes. The Journal of Physical Chemistry C. 2010 Apr 21;114(19):8814-20.
29. Sprunger PT, Plummer EW. The interaction of hydrogen with simple metal surfaces. Surface science. 1994 Apr 20;307:118-23.

CHAPTER 3

Effect of Au Content on the Enhanced Photocatalytic Efficiency of Mesoporous Au/TiO_2 Nanocomposites in UV and Sunlight

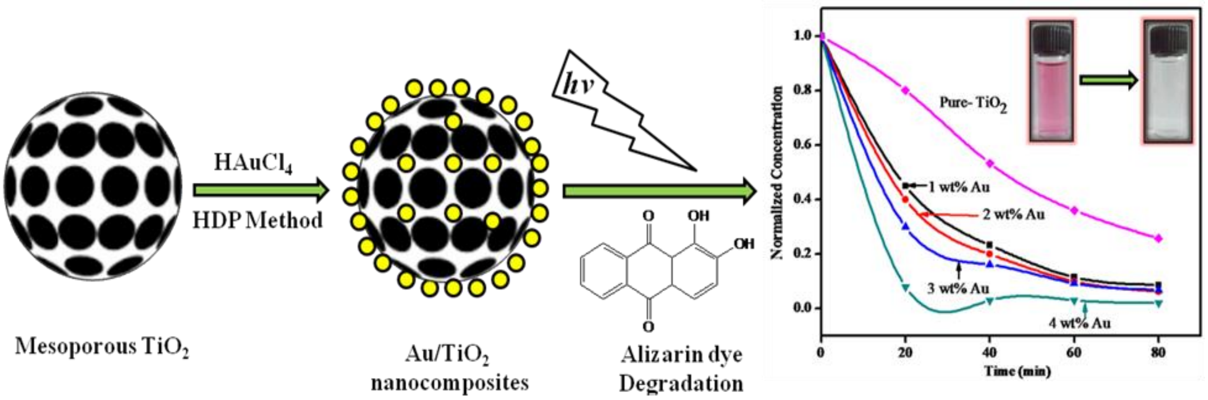

Highlights

- Homogeneous deposition-precipitation (HDP) method favored the formation of Au/TiO_2 nanocomposites with different Au loading.
- Complete photodegradation of alizarin dye under UV and sunlight by these nanocomposites were compared.
- Catalytic activity and sedimentation properties were better than commercial nano-TiO_2 (Degussa P25).
- The reusability of the photocatalysts exhibited more than 98% degradation of the dye even after 10 consecutive cycles.

3.1 Introduction

Dye pollutants are among the prime sources of water contamination from the textile and printing industries. The treatment of these dye effluents is highly desired for the preservation of clean air, soil and water. There is an immediate need to take some necessary steps to develop efficient photocatalyst to degrade these toxic pollutants.

Anatase phase of TiO_2 is one of the best photocatalysts for pollutant dye degradation. Selectively TiO_2 is important due to their very low cost, excellent chemical, mechanical stability, catalytic activity, availability and non-toxicity [1-3]. The only limitation for TiO_2 as a photocatalyst is its band gap (3.2 eV for anatase) disables it to be active in the visible light region of the solar spectrum. But, the presence of rutile phase shifts its absorption maximum towards visible light. Doping with metal or nonmetallic elements [4-5] or by deposition of noble metal nanoparticles (NPs) on TiO_2 surface is also an effective way to improve the photocatalytic activity of the catalyst [6-8]. Previously it has been reported that when TiO_2 is doped with noble metals it's photocatalytic activity is enhanced under UV and visible light irradiation. The improved UV light photocatalytic activity is recognized due to effective charge separation of the electron when they are transferred from conduction band (CB) of TiO_2 to metal NPs, [9-10] on the other hand the surface plasmon resonance effect of some metals like Au and Ag also help TiO_2 to sensitize in visible light [11-13]. Earlier reports revealed the improved visible light activity of the Au/TiO_2 due to sensitization of TiO_2 by Au credited to the metal surface plasmon resonance [14-16]. Various methods have been employed for synthesis of metal (Au) loaded TiO_2 as adsorption of gold colloids, [17] photo deposition under UV irradiation, [18] deposition precipitation, [19] wet impregnation and chemical reduction [20]. Large surface area of mesoporous TiO_2, make it a best support material with better efficiency. But the synthesis of mesoporous TiO_2 with high crystalline nature is challenging [21]. Electrons from the conduction band of anatase TiO_2 can transfer to the gold NP's (excited state) which help in the formation of superoxide radical anions [22]. The catalytic activity of mesoporous TiO_2 supported gold NPs largely depends on particle size, the surface area of supported material and the synthesis method. Literature reveals [23] that the BET surface area of mesoporous TiO_2 is in the range of 50-100 m^2/g. Different techniques have been utilized to create and modify the Au/TiO_2 catalyst for better catalytic performances. Homogeneous deposition–precipitation (HDP) method is one of the most favored methods for the synthesis of Au-TiO_2 due to the greater accessibility of higher dispersion of gold NPs at the lesser concentration on catalyst support and control of pore structures [24].

In this respect herein, we have synthesized a series of Au/TiO_2 (different weight ratio of Au) nanocomposites by HDP method. We have maintained the quantitative control of particle composition and studied the role of particle size as well as surface area on reaction rate. The influence of support on the photocatalytic action was also monitored. The structural and morphological results were investigated by X-ray diffraction (XRD), (BET) analysis, N_2 adsorption-desorption isotherms, Ultraviolet-visible spectroscopy. The surface morphology was studied by transmission electron microscopy (TEM) and the oxidation state by X-ray photoelectron spectroscopy (XPS). The main goal of our work was to synthesize different Au/TiO_2 composites using HDP method and to study their photocatalytic activity regarding degradation of alizarin red dye as model water pollutant under UV irradiation as well as sunlight. Also, the effect of different Au/TiO_2 ratios on the photocatalytic activity and reusability was investigated.

3.2 Experimental procedure

3.2.1 Synthesis of mesoporous titania support

The mesoporous titania was prepared by the method as reported by Cui et al. [25]. The mixture of titanium isopropoxide, 2-propanol and H_2O, having molar ratio nearly as 1:20:5 whereas the volume (in mL) ratios equal to 10:60:3 were continuously stirred at room temperature for 1h. Then the precipitates were aged at 353K, dried in hot air oven at 373K and finally calcined at 623K for 4h.

3.2.2 Synthesis of gold doped titania nanocomposites

The synthesis of Au/TiO_2 catalysts with varying gold ratio was done by HDP method [24, 26] using urea as the precipitating agent. An aqueous suspension of $HAuCl_4.3H_2O$ (Sigma–Aldrich, 99.8%) with required gold loading and urea was continuously stirred at a temperature of -10^oC for 5h. Upon heating, urea decomposes to ammonia completely and the reaction occurs in a homogeneous manner and as a result the solution pH shifts to the basic range (pH ~6–8). The mesoporous titania (support) was then added to the above mixture with continuous stirring. After 30 minutes, freshly prepared 0.1 M $NaBH_4$ was added dropwise in order to precipitate gold NPs over TiO_2 support. The composite obtained was centrifuged at 3000 rpm with water till the filtrate constrained no chloride ions (confirmed with the $AgNO_3$ test), dried in hot air oven at 60^0C and finally calcined at 400^0C for 3h in the N_2 atmosphere.

3.2.3 Catalyst characterization

Diffraction analysis (XRD) of different Au/TiO_2 catalysts was performed using Miniflex (M/s. Rigaku Corporation, Japan). X-ray Diffractometer having Ni-filtered Cu Kα radiations

(λ = 0.1504 nm) at 30 kV. Fourier transforms infrared (FTIR) spectra were carried on Carry 660, Agilent Technologies FTIR spectrometer. Surface area was analyzed through BET surface area analyzer of Autosorb-1, Quanta chrome instruments, USA at –196 °C. The samples were first degassed at 250^0C to ensure a clean surface for adsorption isotherm. The pore size distribution records were calculated by the BJH model from N_2 desorption isotherms. UV-Vis diffused reflectance spectra of catalysts were carried out through Shimadzu UV-2450 spectrophotometer with an integrating sphere reflectance accessory. The detailed structural analysis of catalyst was carried out through transmission electron microscopy (TEM) using a Technai-12, FEI Netherlands by the accelerating voltage of 120 kV. X-ray photoelectron spectroscopy (XPS) was used to study the chemical composition and oxidation state of different Au/TiO_2 catalysts. The XPS spectra of the various catalysts were determined on an XPS spectrometer (KRATOS Axis 165 Shimadzu, UK) through Mg Kα radiation 1252.6 eV at 75W.

3.2.4 Photocatalytic Study

The desired amount of catalyst (20 mg) was added to aqueous solution of alizarin dye (5 mL of 0.01 mM) and stirred for 30 minutes in the dark to establish adsorption-desorption equilibrium. The reaction sample was irradiated by UV irradiation (64W Hg lamp) and in bright sunlight for all the catalysts at different time intervals up to 80 minutes (1000 to1200 hrs). The catalyst was filtered (0.2µm cellulose filter) and change in dye concentration was monitored by UV-Vis spectrophotometer (Analytik Jena Specord-200). Photodegradation efficiency was calculated by the following formula:

$$R = \{(C_0-C)/ C_0 \}\times 100=\{(A_0-A)/A_0\}\times 100$$

Where A_0, A, and C_0, C are the absorbance and concentration of alizarin dye when the reaction time was 0 and t, respectively.

The turn over number (TON) and the turn over frequency (TOF) were calculated as per following equations:

$$\text{TON} = \frac{\text{No.of mole (equivalents) of rectant}}{\text{No.of mole (equivalents) of catalyst}}$$

$$\text{TOF} = \frac{\text{TON}}{\text{time (h)}}$$

3.3 Results and discussion

3.3.1 Characterization of catalysts

The diffuse reflectance spectra of mesoporous TiO_2 and Au/TiO_2 catalysts are shown in Fig. 3.1 (a). TiO_2 is almost transparent to visible region (400-700) of the spectrum whereas the as-prepared Au/TiO_2 composites show absorbance in the wavelength range 400-450 nm [35, 36]. The absorbance spectra show a red shift in excitation wavelength upon Au loading on TiO_2 which can be due to the quantum size effect of Au NPs on increasing Au content in the catalyst. The red shift corresponds to a narrowing of the band gap of the Au/TiO_2 catalysts due to an increase of the size of Au NPs. The intensity of the absorbance band increases gradually for higher loadings of gold which is probably due to the more gold NPs embedded in mesoporous TiO_2. The intensity of the UV-region absorbance band for Au/TiO_2 catalysts was found to be almost similar to that of mesoporous TiO_2. As observed from XRD results, the crystallite sizes increase as Au loading increases. Therefore, the absorption band shifts toward the region of longer wavelength with an increase in the crystallite size of Au in Au/TiO_2 nanocomposites.

X-Ray diffraction patterns of Au/TiO_2 catalysts are shown in Fig. 3.1(b). The wide angle diffraction peaks at 2θ ~ 25.6°, 37.8°, 48.1°, 55.1°, and 62.7° correspond to (101), (112), (200), (105) and (204) diffraction planes are characteristic of the anatase TiO_2 (JCPDS file number: 21-2172) [27,28]. Peaks corresponding to Au can be observed around 2θ ~ 38.2°, 44.6°, 64.9°, 77.9° and are related to Au-FCC lattice of (111), (200), (220), and (311) planes, (JCPDS file number: 04–0784) [29]. Crystallite size of Au can be calculated using Debye Scherrer equation with a mean range of 6.1-6.9 nm.

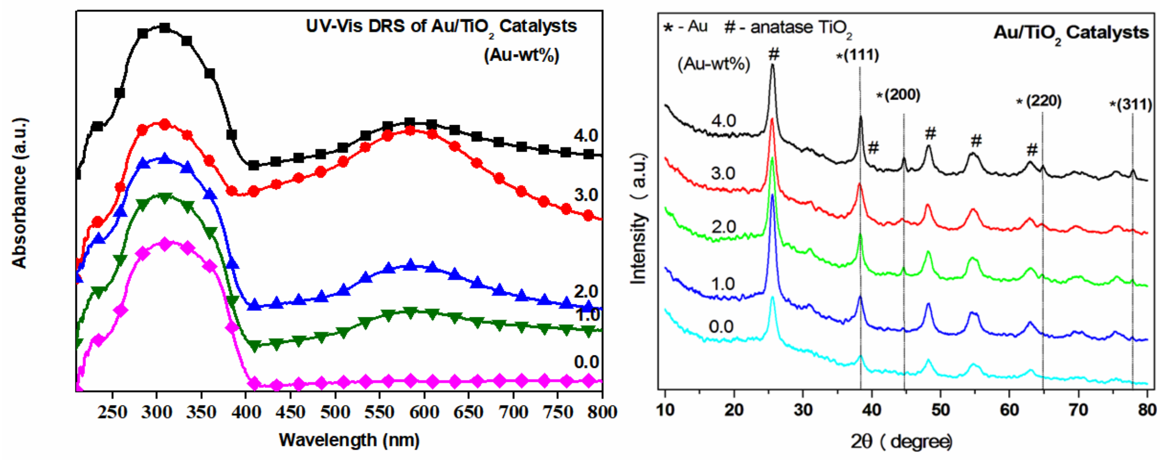

Fig. 3.1: (a) UV-Vis diffused reflectance spectrum **(b)** XRD patterns of mesoporous TiO_2 and Au/TiO_2 catalysts.

The nitrogen adsorption/desorption isotherm of the mesoporous TiO_2 and Au/TiO_2 catalysts are shown in Fig. 3.2(a). All samples were observed to possess Langmuir type-IV isotherm [30, 31] and BJH plots depicting the pore size distribution of Au/TiO_2 catalysts (Fig 3(b)). The values of the specific surface area, mean pore diameter and pore volume of as-prepared Au/TiO_2 catalysts are given in Table 3.1.

Table 3.1: Textural properties of mesoporous TiO_2 and different wt% of Au/TiO_2 catalysts.

Au loading (wt%)	**Au content ^{a} (wt%)**	**Surface area^b(m^2/g)**	**V_t (cc/g)**	**D_{BJH} (nm)**
0.0	0.00	186	0.32	6.9
1.0	0.85	169	0.28	6.7
2.0	1.55	141	0.21	6.3
3.0	2.54	130	0.20	6.2
4.0	3.58	119	0.19	6.1

[a] Gold content measured by ICP-OES.

[b] BET method; V_t : total pore volume; D_{BJH} : average pore diameter calculated by BJH adsorption method.

It is observed that the surface area and pore volume of Au/TiO_2 catalysts tend to decrease upon incorporation of Au on TiO_2. The nitrogen adsorption isotherms of catalysts exhibit H_2–type hysteresis loop which corresponds to pores having narrow necks and the wider bodies [32] and shows a sharp step in P/P_0 range of 0.6 – 0.9. This sharp step indicates the uniform nature of the pore size [33, 34]. But, the hysteresis loops of all Au/TiO_2 catalysts becomes smaller due to which position of the step shift towards slightly lower relative pressure in the range of 0.45 – 0.89 (observed from the Fig. 3.2 (a)), which indicates that smaller pore size is formed.

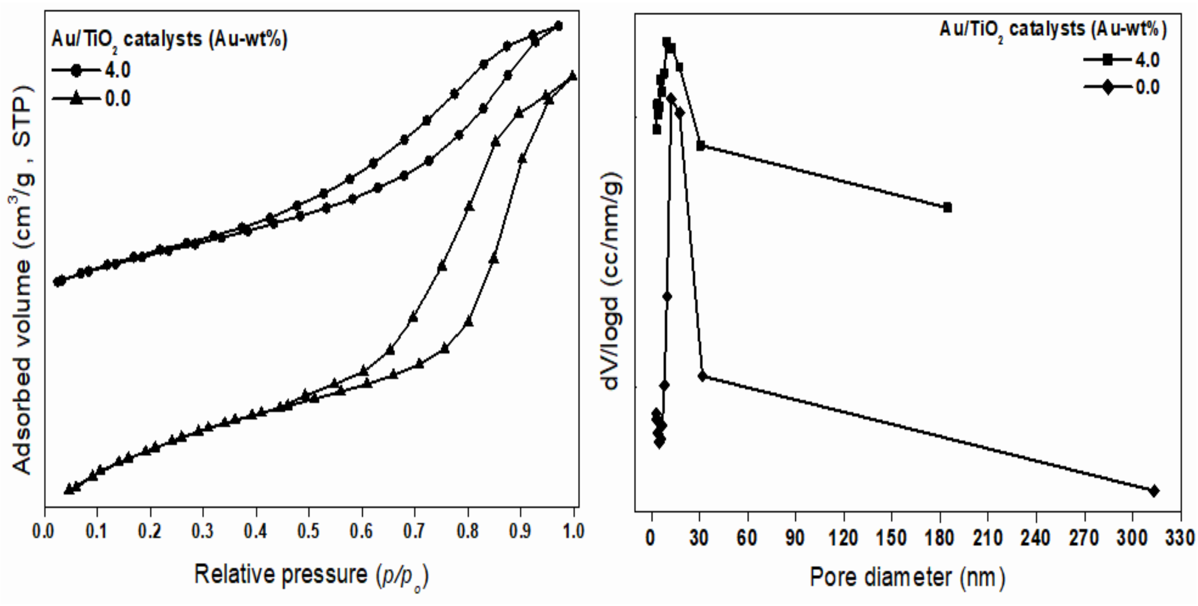

Fig. 3.2: (a) N_2 adsorption-desorption isotherms (b) BJH pore size distribution for mesoporous TiO_2 and 4wt% Au/TiO_2 catalyst.

Spherical Au NPs can be clearly observed to be confined on TiO_2 channels as seen from TEM images (Fig. 3.3). The particle size of Au NPs can be observed to be around 14 nm and the corresponding histogram (Fig. 3.3(d)) clearly shows the gold particles distribution with different loading of the catalysts. The fraction of gold atoms exposed to the surface of AuNPs was calculated based on upon the work of Boudart and Djega-Mariadassou [38]. The strength or percentage of AuNPs that are exposed to the substrate is approximately 0.9/d, where d is the mean particle diameter in nm. Thus AuNPs with a diameter of 14 nm has about 6.42 % (0.9/14 nm) of their atoms lying at the surface of the AuNP. Furthermore, TON and TOF based upon surface atoms are 2800 and 2333 h^{-1} respectively.

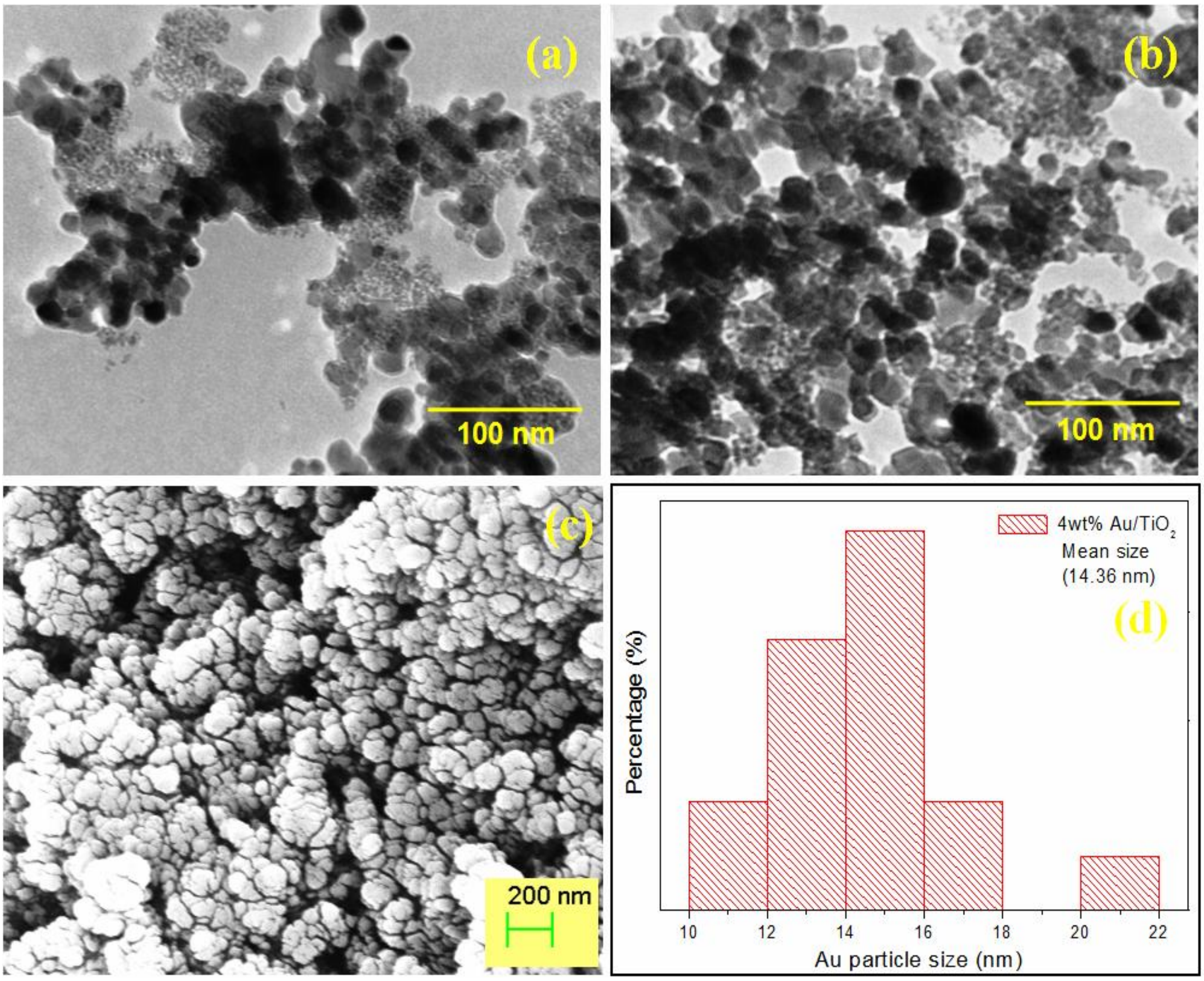

Fig. 3.3: (a) TEM image of 1wt% of Au/TiO_2 (b) TEM image of 4wt% Au/TiO_2 (c) FESEM image of 4wt% Au/TiO_2 and (d) histogram of 4wt% Au/TiO_2 catalyst.

The high resolution XPS (Fig. 3.4) spectrum show binding energy of Au $4f_{7/2}$ at 84.0 eV and Au $4f_{5/2}$ at 87.7 eV, which are notably different from Au^{+} $4f_{7/2}$ (84.6 eV) and Au^{3+} $4f_{7/2}$ (87.0 eV). Peaks corresponding to the binding energies at 84.6 eV ($4f_{7/2}$) and 87.0 eV ($4f_{7/2}$) are absent. These results also confirm that Au NPs on the surface of mesoporous TiO_2 support are in the Au^{0} state [39-41]. On the other hand, the XPS results confirm the absence of any contamination from chlorine and sodium species.

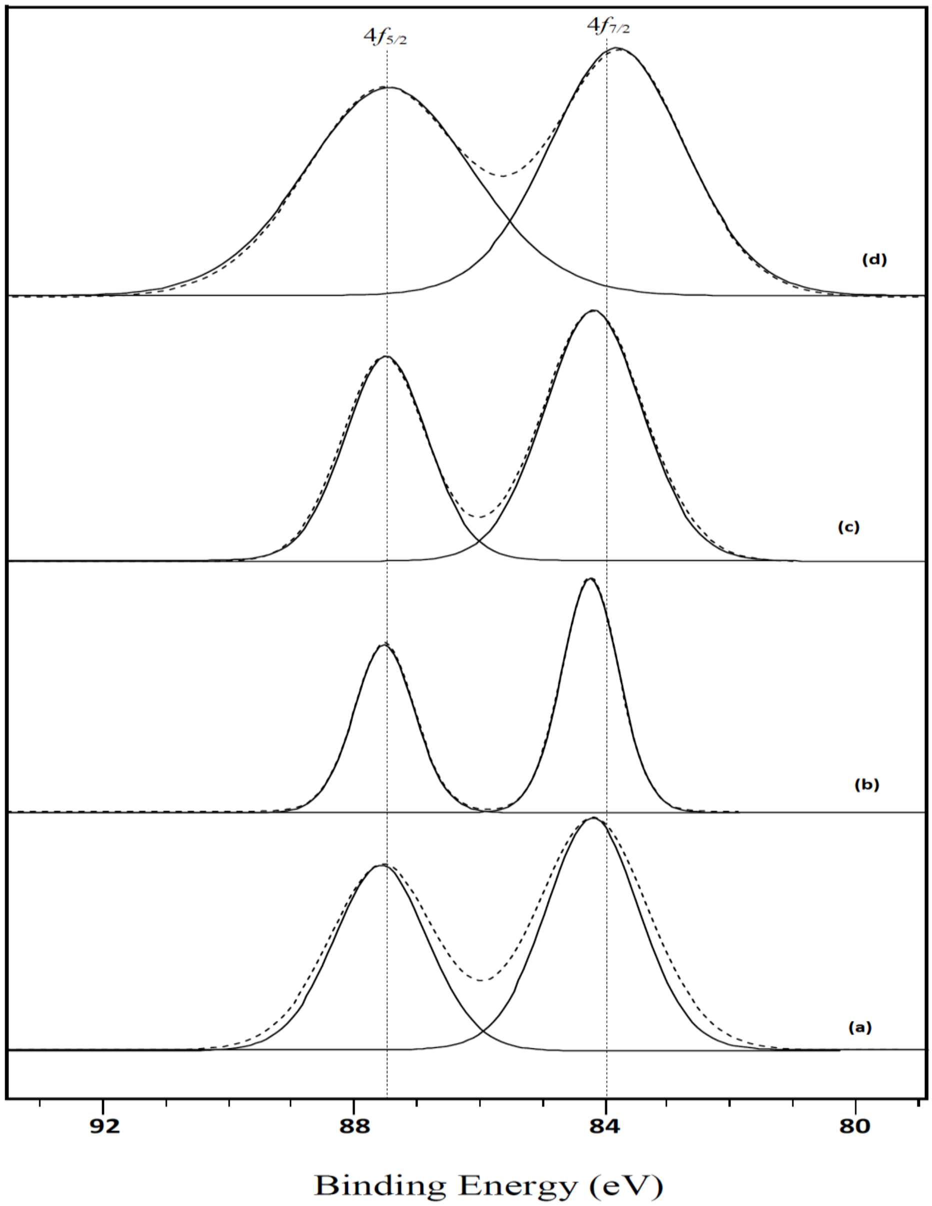

Fig. 3.4: XPS spectrum of Au/TiO_2 catalysts with different Au (wt %) loadings [(a) 1wt% (b) 2wt% (c) 3wt% and (d) 4wt%].

3.3.2 Photocatalytic degradation of alizarin dye

Control experiments established that alizarin dye did not degrade by Au/TiO_2 composite suspensions in the dark. The photolysis of alizarin in the absence of photocatalyst is only ~4% which can be neglected. The photodegradation was monitored prior to the decrease in the intensity of absorption peak corresponding to 520 nm in the UV-Visible spectra (Fig. 3.5)

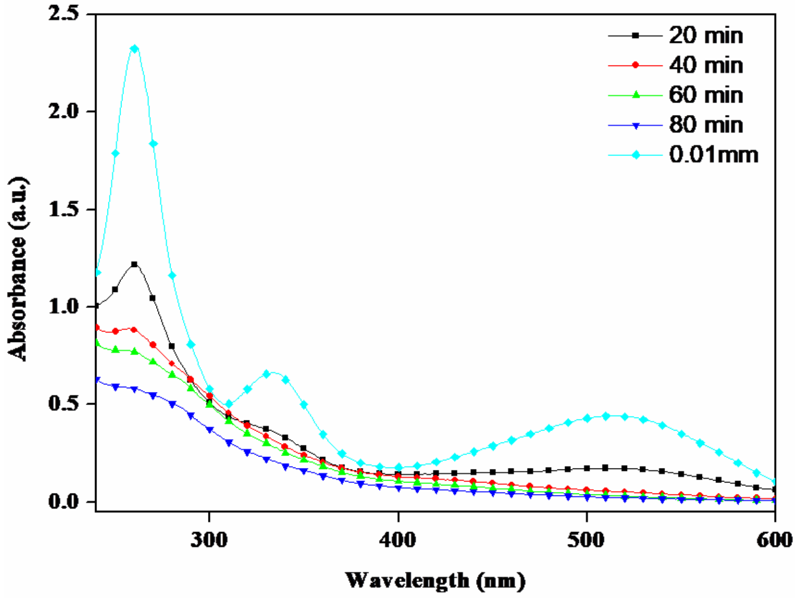

Fig. 3.5: UV-Visible spectra of alizarin dye under UV irradiation showing photocatalytic activity by 4wt% Au/TiO_2 nanocomposite.

The photocatalytic activities of different Au content on TiO_2 sample are found to have higher activity than that of commercial pure TiO_2 (Fig. 3.6). The percentage of gold doping over TiO_2 is varied in order to accomplish the maximum photocatalytic activity. Incorporation of Au NPs increases the activity of TiO_2 significantly. Among all these samples that contain higher loading of Au (4% Au) shows the highest photocatalytic activity. The calculated degradation efficiency of Au/TiO_2 (4%) is up to ~99%. The change in normalized concentration of dye by different Au (wt %) loaded TiO_2 is illustrated in Fig. 3.6 which shows 4 wt% as optimum to enhance the photocatalytic activity of TiO_2 under UV and Visible light irradiation.

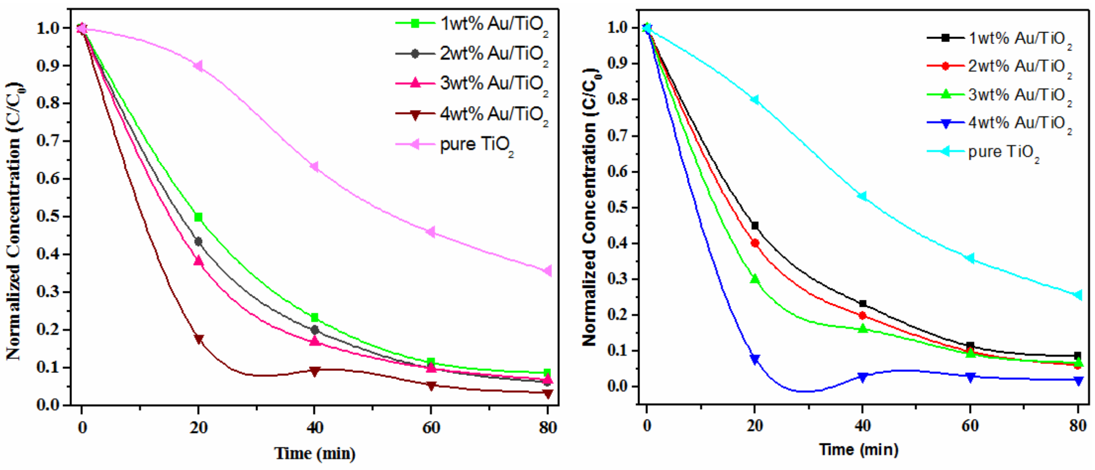

Fig. 3.6: Kinetic variation towards alizarin photodegradation under UV-irradiation (left) and sunlight (right) on various Au/TiO_2 nanocomposities.

The increase in photocatalytic activity with Au content can be understood by the reason that the number of Au NPs over the support can lead to the enhanced migration of electrons from the CB of TiO_2 to the Au surfaces which promotes the electron transfer to the adsorbed O_2 molecules [42]. This will facilitate the formation of more number of $O_2^{\cdot -}$ and finally can lead to the formation of more number of ·OH which is responsible for dye degradation. The OH radicals are very strong oxidative species (2.8V vs. SHE) which are capable of oxidizing almost all organic pollutants.

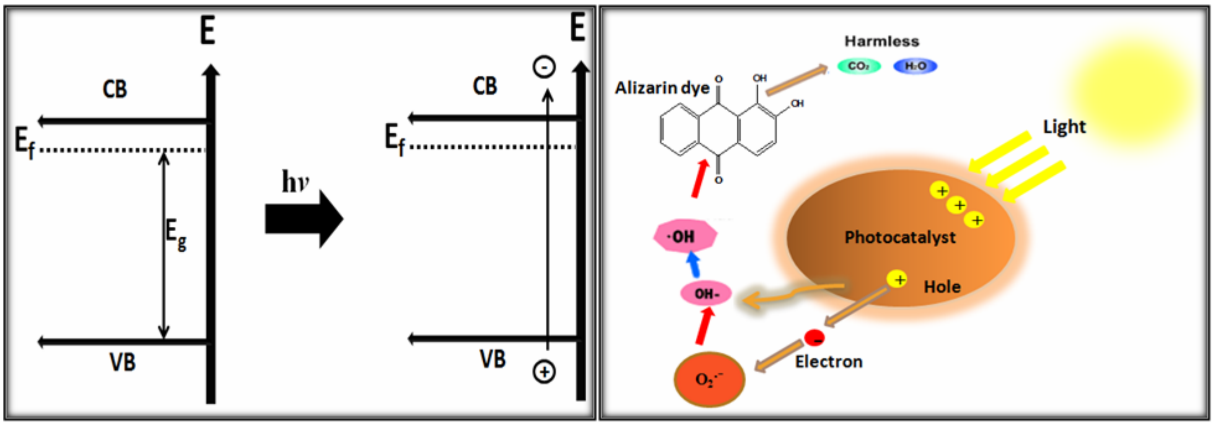

Fig. 3.7: Plausible mechanism of photodegradation of dyes over Au/TiO_2 nanocomposites.

In addition, the case of incorporated metal nanocomposites can enhance electron migration from the semiconductor surface and reduces the recombination probability of photogenerated electrons and holes. Thus it can be understood that insertion of Au NP as well as increase in the amount of gold particles (4wt%) has increased the photocatalytic activity of TiO_2 significantly. The general mechanism of photodegradation is schematically represented in Fig. 3.7. Recently, reusability of the photocatalyst is one of the most important attempts to avoid the difficulties in the separation of catalytic powder after dye degradation. There are limited numbers of experiment which are based on reusability studies. Present catalysts are easily separable from the solution and also it is well dispersible under stirring. There was no permanent adsorption of dye over the catalyst, so it is very simple to detach the catalyst from the dye solution by the centrifugation process. Regeneration of 4wt% Au/TiO_2 catalyst was done after each reaction, by centrifugation and further washing with water. The photocatalytic activity of the catalyst remains approximately constant even up to ten consecutive experiments.

References

1.Yu J, Qi L, Jaroniec M. Hydrogen production by photocatalytic water splitting over Pt/TiO_2 nanosheets with exposed (001) facets. The Journal of Physical Chemistry C. 2010 Jul 13;114(30):13118-25.

2. Li H, Bian Z, Zhu J, Zhang D, Li G, Huo Y, Li H, Lu Y. Mesoporous titania spheres with tunable chamber stucture and enhanced photocatalytic activity. Journal of the American Chemical Society. 2007 Jul 11;129(27):8406-7

3. Xiaobo C. Titanium dioxide nanomaterials and their energy applications. Chinese Journal of Catalysis. 2009 Aug 1;30(8):839-51.

4. Wang X, Blackford M, Prince K, Caruso RA. Preparation of boron-doped porous titania networks containing gold nanoparticles with enhanced visible-light photocatalytic activity. ACS applied materials & interfaces. 2012 Jan 13;4(1):476-82.

5. Hamal DB, Klabunde KJ. Synthesis, characterization, and visible light activity of new nanoparticle photocatalysts based on silver, carbon, and sulfur-doped TiO_2. Journal of Colloid and Interface Science. 2007 Jul 15;311(2):514-22.

6. Primo A, Corma A, García H. Titania supported gold nanoparticles as photocatalyst. Physical Chemistry Chemical Physics. 2011;13(3):886-910.

7. Wang X, Caruso RA. Enhancing photocatalytic activity of titania materials by using porous structures and the addition of gold nanoparticles. Journal of Materials Chemistry. 2011;21(1):20-8.

8. Tada H, Kiyonaga T, Naya SI. Rational design and applications of highly efficient reaction systems photocatalyzed by noble metal nanoparticle-loaded titanium (IV) dioxide. Chemical Society Reviews. 2009;38(7):1849-58.

9. Gomes Silva C, Juárez R, Marino T, Molinari R, García H. Influence of excitation wavelength (UV or visible light) on the photocatalytic activity of titania containing gold

nanoparticles for the generation of hydrogen or oxygen from water. Journal of the American Chemical Society. 2010 Dec 13;133(3):595-602.

10. Gomes Silva C, Juárez R, Marino T, Molinari R, García H. Influence of excitation wavelength (UV or visible light) on the photocatalytic activity of titania containing gold nanoparticles for the generation of hydrogen or oxygen from water. Journal of the American Chemical Society. 2010 Dec 13;133(3):595-602.

11. Nishijima Y, Ueno K, Kotake Y, Murakoshi K, Inoue H, Misawa H. Near-infrared plasmon-assisted water oxidation. The journal of physical chemistry letters. 2012 Apr 30;3(10):1248-52.

12. Tsukamoto D, Shiraishi Y, Sugano Y, Ichikawa S, Tanaka S, Hirai T. Gold nanoparticles located at the interface of anatase/rutile TiO_2 particles as active plasmonic photocatalysts for aerobic oxidation. Journal of the American Chemical Society. 2012 Apr 2;134(14):6309-15.

13. Wang H, You T, Shi W, Li J, Guo L. Au/TiO_2/Au as a plasmonic coupling photocatalyst. The Journal of Physical Chemistry C. 2012 Mar 6;116(10):6490-4.

14. Lu Y, Yu H, Chen S, Quan X, Zhao H. Integrating plasmonic nanoparticles with TiO_2 photonic crystal for enhancement of visible-light-driven photocatalysis. Environmental science & technology. 2012 Jan 20;46(3):1724-30.

15. Seh ZW, Liu S, Low M, Zhang SY, Liu Z, Mlayah A, Han MY. Janus Au- TiO_2 Photocatalysts with Strong Localization of Plasmonic Near- Fields for Efficient Visible- Light Hydrogen Generation. Advanced Materials. 2012 May 2;24(17):2310-4.

16. Li J, Zeng HC. Preparation of monodisperse Au/TiO_2 nanocatalysts via self-assembly. Chemistry of materials. 2006 Sep 5;18(18):4270-7.

17. Yogi C, Kojima K, Takai T, Wada N. Photocatalytic degradation of methylene blue by Au-deposited TiO_2 film under UV irradiation. Journal of materials science. 2009 Feb 1;44(3):821

18. Li WC, Comotti M, Schüth F. Highly reproducible syntheses of active Au/TiO2 catalysts for CO oxidation by deposition–precipitation or impregnation. Journal of Catalysis. 2006 Jan 1;237(1):190-6.

19. Hidalgo MC, Maicu M, Navío JA, Colón G. Effect of sulfate pretreatment on gold-modified TiO_2 for photocatalytic applications. The Journal of Physical Chemistry C. 2009 Jun 18;113(29):12840-7.

20. Tian Y, Tatsuma T. Mechanisms and applications of plasmon-induced charge separation at TiO_2 films loaded with gold nanoparticles. Journal of the American Chemical Society. 2005 May 25;127(20):7632-7.

21. Iliev V, Tomova D, Bilyarska L, Tyuliev G. Influence of the size of gold nanoparticles deposited on TiO_2 upon the photocatalytic destruction of oxalic acid. Journal of Molecular Catalysis A: Chemical. 2007 Feb 14;263(1-2):32-8.

22. Chen D, Huang F, Cheng YB, Caruso RA. Mesoporous anatase TiO_2 beads with high surface areas and controllable pore sizes: a superior candidate for high- performance dye- sensitized solar cells. Advanced Materials. 2009 Jun 5;21(21):2206-10.

23. Tran ND, Besson M, Descorme C. TiO_2-supported gold catalysts in the catalytic wet air oxidation of succinic acid: influence of the preparation, the storage and the pre-treatment conditions. New Journal of Chemistry. 2011;35(10):2095-104.

24. Addamo M, Augugliaro V, Di Paola A, García-López E, Loddo V, Marcì G, Molinari R, Palmisano L, Schiavello M. Preparation, characterization, and photoactivity of polycrystalline nanostructured TiO_2 catalysts. The Journal of Physical Chemistry B. 2004 Mar 11;108(10):3303-10.

25. Cui F, Hua Z, Wei C, Li J, Gao Z, Shi J. Highly dispersed Au nanoparticles incorporated mesoporous TiO_2 thin films with ultrahigh Au content. Journal of Materials Chemistry. 2009;19(41):7632-7.

26. Dimitratos N, Lopez-Sanchez JA, Morgan D, Carley A, Prati L, Hutchings GJ. Solvent free liquid phase oxidation of benzyl alcohol using Au supported catalysts prepared using a sol immobilization technique. Catalysis today. 2007 Apr 30;122(3-4):317-24.

27. Pizzio LR. Mesoporous titania: effect of thermal treatment on the texture and acidic properties. Materials Letters. 2005 Apr 1;59(8-9):994-7.

28. Chen Y, Wang H, Liu CJ, Zeng Z, Zhang H, Zhou C, Jia X, Yang Y. Formation of monometallic Au and Pd and bimetallic Au–Pd nanoparticles confined in mesopores via Ar

glow-discharge plasma reduction and their catalytic applications in aerobic oxidation of benzyl alcohol. Journal of catalysis. 2012 May 1;289:105-17.

29. Niwa M, Iwamoto M, Segawa KI. Temperature-programmed desorption of ammonia on zeolites. Influence of the experimental conditions on the acidity measurement. Bulletin of the Chemical Society of Japan. 1986 Dec;59(12):3735-9.

30. Yang H, Tang D, Lu X, Yuan Y. Superior performance of gold supported on titanium-containing hexagonal mesoporous molecular sieves for gas-phase epoxidation of propylene with use of H_2 and O_2. The Journal of Physical Chemistry C. 2009 Apr 22;113(19):8186-93.

31. Yu JG, Su YR, Cheng B. Template- free fabrication and enhanced photocatalytic activity of hierarchical macro- /mesoporous titania. Advanced Functional Materials. 2007 Aug 13;17(12):1984-90.

32. Flego C, Carluccio L, Rizzo C, Perego C. Synthesis of mesoporous SiO_2–ZrO_2 mixed oxides by sol–gel method. Catalysis Communications. 2001 May 1;2(2):43-8.

33. Du M, Zhan G, Yang X, Wang H, Lin W, Zhou Y, Zhu J, Lin L, Huang J, Sun D, Jia L. Ionic liquid-enhanced immobilization of biosynthesized Au nanoparticles on TS-1 toward efficient catalysts for propylene epoxidation. Journal of catalysis. 2011 Oct 27;283(2):192-201.

34. Basu S, Pande S, Jana S, Bolisetty S, Pal T. Controlled interparticle spacing for surface-modified gold nanoparticle aggregates. Langmuir. 2008 Apr 22;24(10):5562-8.

35. Yu J, Yue L, Liu S, Huang B, Zhang X. Hydrothermal preparation and photocatalytic activity of mesoporous Au–TiO_2 nanocomposite microspheres. Journal of colloid and interface science. 2009 Jun 1;334(1):58-64.

36. Zhong X, Feng Y, Lieberwirth I, Knoll W. Facile synthesis of morphology-controlled platinum nanocrystals. Chemistry of materials. 2006 May 16;18(10):2468-71.

37. Zwijnenburg A, Goossens A, Sloof WG, Craje MW, van der Kraan AM, Jos de Jongh L, Makkee M, Moulijn JA. XPS and Mössbauer characterization of Au/TiO2 propene epoxidation catalysts. The Journal of Physical Chemistry B. 2002 Sep 26;106(38):9853-62.

38. Boudart M, Djéga-Mariadassou G. Kinetics of heterogeneous catalytic reactions. Princeton University Press; 2014 Jul 14.

39. Kumar A, Kumar VP, Kumar BP, Vishwanathan V, Chary KV. Vapor phase oxidation of benzyl alcohol over gold nanoparticles supported on mesoporous TiO_2. Catalysis letters. 2014 Aug 1;144(8):1450-9.

40. Kumar A, Kumar VP, Vishwanathan V, Chary KV. Synthesis, characterization, and reactivity of Au/MCM-41 catalysts prepared by homogeneous deposition–precipitation (HDP) method for vapor phase oxidation of benzyl alcohol. Materials Research Bulletin. 2015 Jan 1;61:105-12.

41. Xiang Q, Yu J, Cheng B, Ong HC. Microwave- Hydrothermal Preparation and Visible- Light Photoactivity of Plasmonic Photocatalyst Ag- TiO_2 Nanocomposite Hollow Spheres. Chemistry–An Asian Journal. 2010 Jun 1;5(6):1466-74.

42. Sharma M, Das D, Baruah A, Jain A, Ganguli AK. Design of porous silica supported tantalum oxide hollow spheres showing enhanced photocatalytic activity. Langmuir. 2014 Mar 13;30(11):3199-208.

Controlled Photocatalytic Hydrolysis of Nitriles to Amides by Mesoporous MnO_2 Nanoparticles Fabricated by Mixed Surfactant Mediated Approach

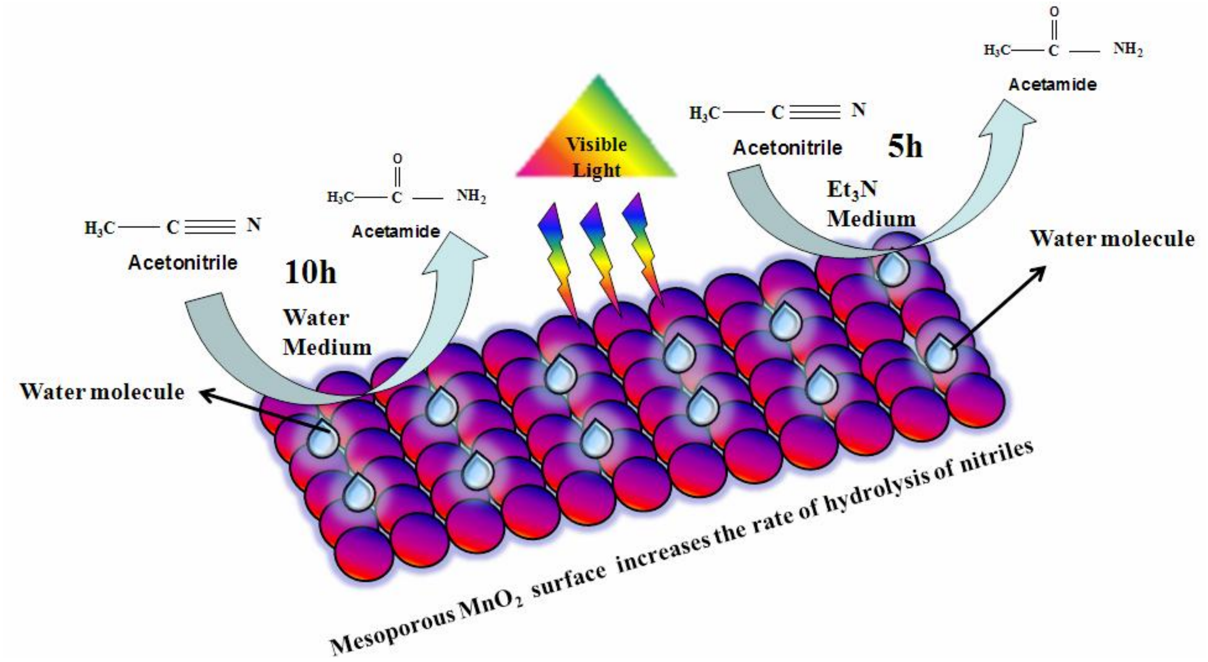

Highlights

- Synthesis of mesoporous MnO_2 by using a mixture of cationic and anionic surfactants with variable pore volume.
- The cat-anionic surfactant yields 5 times higher surface area (195.32m^2/g) than their corresponding individual form (CTAB 29 m^2/g and SDS 36 m^2/g).
- The synergic effect, low critical aggregation concentration of cat-anionic surfactant is endorsed for its high surface area.
- The mesoporous MnO_2 as a novel catalyst for the hydrolysis of nitriles to amides.
- Higher yield (90%) in basic reaction medium compared to neutral medium (70%).

4.1 Introduction

One of the most important industrial reactions in the organic chemistry is amide bond formation as it constitutes important moieties in many pharmaceutical and biologically active ingredients[1]. Moreover, the flattering properties of amides like stability, conformational diversity and high polarity make it one of the most reliable and accepted functional groups in every branch of organic chemistry. Among all the methods reported for the fabrication of amides, hydration of nitriles has become one of the most widely used methods to obtain primary amides. But this is a challenging reaction as there is the possibility of acid formation from amides. The hydrolysis reaction is catalysed in acidic and basic medium, but many of the methods require harsh conditions with poor yields due to further conversion of amides to acids[2, 3]. Improved methods for the selective and controlled synthesis of amides using catalysts under stable conditions are of great demand [4(a)]. In this regard, the formation of amides by hydrolysis of nitriles using transition metal oxides nanomaterials as a photocatalyst is good choice to obtain better yields. It is a principal objective of the present study to provide a new method for converting nitriles to amides.

Nanoporous transition metal oxides with controlled morphology, porous structures, tunable nano pores, and well-ordered mesostructures make them ideal photocatalysts in the field of catalysis. During recent times, of all the transition metal oxides, manganese dioxide (MnO_2) nanostructures have received keen attention due to its attractive physical and chemical properties[4(b, c)]. The MnO_2 is non-stoichiometric compound and can exist in different crystallographic forms. The crystallographic forms are generally supposed to be responsible for their variable properties and the controlled synthesis of MnO_2 which make the controlled design of a specific form primary objective [5]. Previously, many processes have been developed for the synthesis of MnO_2 nanoparticles with different shapes and morphology. Out of all the processes MnO_2 nanostructures are commonly synthesized using hydrothermal treatment[6, 7], the sol-gel process[8, 9], refluxing[10, 11] and normal thermal approach[12] for enormous catalytic application [13, 14] because of their different morphology and variable oxidation states. Several attempts have been made to further improve the catalytic activity by using some facile techniques [15, 16] but enhancing surface area is an excellent way to improve its catalytic properties. As a remedial surfactants based synthesis, are considered as a best route to develop a mesoporous structure. They have the exceptional property to self-organize in the solution, which may modify the interfacial properties and increase the compatibility among the particles. Materials prepared without using surfactants or other stabilizing agents lead to agglomeration as well as reduce the processing temperature of metal oxide and several other materials [17]. Earlier Yan *et al*. have reported the synthesis of MnO_2 using the cationic surfactant (CTAB or CTAC) by direct electrodeposition method with a specific surface area of 102 m^2/g [18], Roy *et al*. have synthesized mesoporous manganese oxides nanostructures by using a bi-template approach with the surface area of 65 m^2/g [19], Zhi *et al.* have fabricated MnO_2 nanoarrays using vacuum-assisted nanocasting with a surface area of 139 m^2/g [20], Saputra *et al.* have synthesized one-dimensional MnO_2 nanoparticles with a surface area of 194 m^2/g [21]. But still, the role of individual surfactants as a porous template for the synthesis of high surface area mesoporous MnO_2 nanoparticles and their effect to convert nitriles to amides has not been fully explored.

In this regard, current work signifies the single step selective and controlled hydrolysis of nitriles to amides under visible light both in the basic and neutral medium using MnO_2 as a photocatalyst. The mechanism for the selective fabrication of amides without any acid moieties has also been fully explored.

4.2. Experimental

4.2.1 Chemicals and Reagents

Manganese (II) nitrate tetrahydrate ($MnNO_3.4H_2O$), Cetyl trimethylammonium bromide (CTAB), Sodium dodecyl sulphate (SDS) and acetonitrile were received from Aldrich. An aqueous solution of $MnNO_3.4H_2O$ (1 M) with the mixture of CTAB (0.25×10^{-3} M) and SDS (0.25×10^{-3} M) was stirred at normal room temperature. For complete conversion of Mn (II) to Mn (IV), the solution was stirred for 20 min in the presence of NaOH and change in the color of the solution was observed from light pink to dark brown, which indicates the formation of MnO_2 nanoparticles denoted as m-MnO_2 (CTAB+SDS) as shown in Fig. 4.1.

The product was recovered by filtration, washing with distilled water, drying and calcined at 623 K for 3 h and used as a solid catalyst for the hydrolysis of nitriles. Similarly, other samples of MnO_2 were also prepared using cationic, CTAB (0.25×10^{-3} M) as well as anionic, SDS (0.25×10^{-3} M) surfactant were denoted as c-MnO_2 and s-MnO_2 respectively.

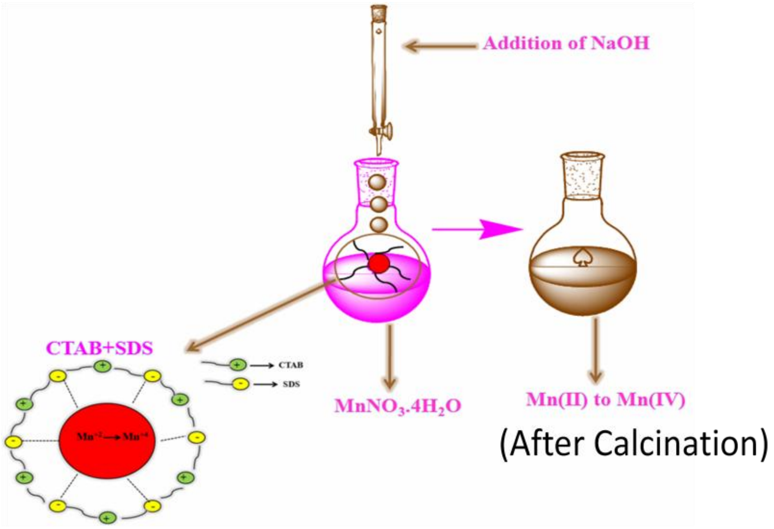

Fig. 4.1: Schematic representation of the synthesis of mesoporous MnO_2.

4.2.2 Photocatalytic Activity

The photocatalytic experiment was carried out in a test tube containing 5 mL of nitrile in 100 μL of solvent (Et_3N or water) and 20 mg of the catalyst. The reaction mixture was illuminated under visible light (40 W CFL lamp) for 5 h by keeping a distance of 1cm apart from the surface of the reaction mixture in the test tube. The reactions were also performed under dark and without catalysts, but no conversions of nitriles to amides are obtained which confirms that reaction does not take place without the presence of both visible light and catalyst. The product was isolated from the reaction mixture by using a nylon syringe filter (0.22μm) and the product was quantitatively analysed by GC-MS and ^{13}C NMR to confirm the formation of amides.

4.3 Results and Discussion

4.3.1 Characterization of Photocatalyst

The phase identification of crystalline MnO_2 was analyzed through XRD analysis (PANALYTICAL X'Pert PRO) with Cu Kα (λ=1.540 Å) as radiation source over the range $0° \leq 2\theta \leq 90°$. The diffraction pattern of as-synthesized different MnO_2 samples exhibits intense diffraction peaks of (110), (101), (211), (220) and (002) which is characteristics of β-MnO_2 structure (JCPDS Card no. 24-0735) with lattice parameters a = 4.399 Å, c = 2.874 Å and space group $P4_2/mnm$ (Fig. 1a).Some other peaks are also highlighted in the Fig. 4.2 which are due to an addition of surfactants.

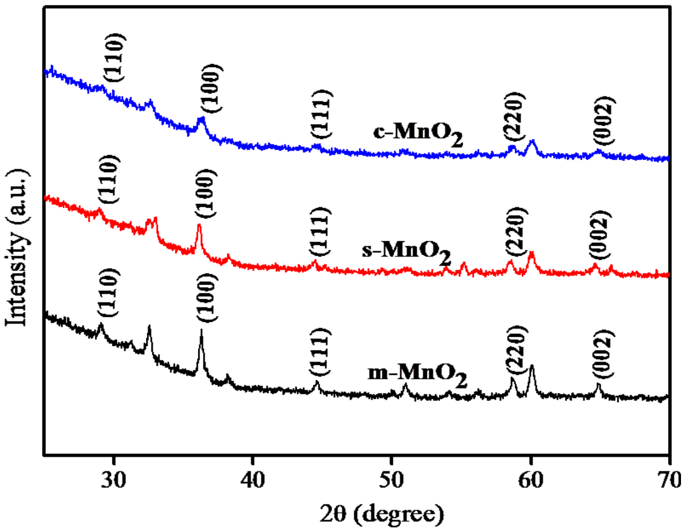

Fig. 4.2: XRD pattern for different MnO_2 nanostructures.

The crystallite size and lattice strain was calculated by Scherrer equation ($D = 0.9\lambda/\beta\cos\theta$), the sample m-$MnO_2$ has largest crystallite size and smallest lattice strain (13nm, 0.0090) compared to c-MnO_2 and s-MnO_2, which is shown in Table 4.1. This larger crystallite size is due to self- assembly in cat-anionic surfactant, which occurs synergistically because of electrostatic attraction between the polar head groups of the surfactants.

Table 4.1: Textural properties of different MnO_2 nanostructures.

Samples	**d**^{a}	ε_L^{b}	**S**$_{bet}$^{c} **(m^{2}g)**	V_p^{d} **(Cm^3/g)**	D_{BJH}^{e}
CTAB	9.28	0.0126	29.0	0.23	46.79
SDS	9.09	0.0129	36.0	0.30	46.85
CTAB+SDS	13	0.0090	195.3	1.95	40.48

[a] Crystallite size determined from Scherrer formula.

[b] Lattice strain determined from XRD analysis.

[c] BET surface area calculated from the linear part of the BET plot ($p/p_0 = 0.05\text{-}0.25$).

[d] Total pore volume, taken from the volume of N_2 adsorbed at $p/p_0 = 0.990$.

[e] Mean pore diameter estimated using the adsorption isotherm.

The chemical composition of m-MnO_2 sample was studied by X-ray photoelectron spectroscopy (XPS) shown in Fig. 4.3, the survey spectra reveals the presence of elements like Mn, O, C. The peaks for β-MnO_2 corresponding to Mn $2p_{3/2}$ and Mn $2p_{1/2}$ were observed at a binding energy of 642.5 and 654.7 eV respectively, which clearly indicates the presence of tetravalent Mn ions. Similarly, the deconvoluted peaks of O 1s at 528.7 eV and 531.3 eV are due to the linkage of Mn-O and Mn-OH respectively. The C 1s peaks at 283.9 eV and 286.2 eV are associated with the presence of a surfactant.

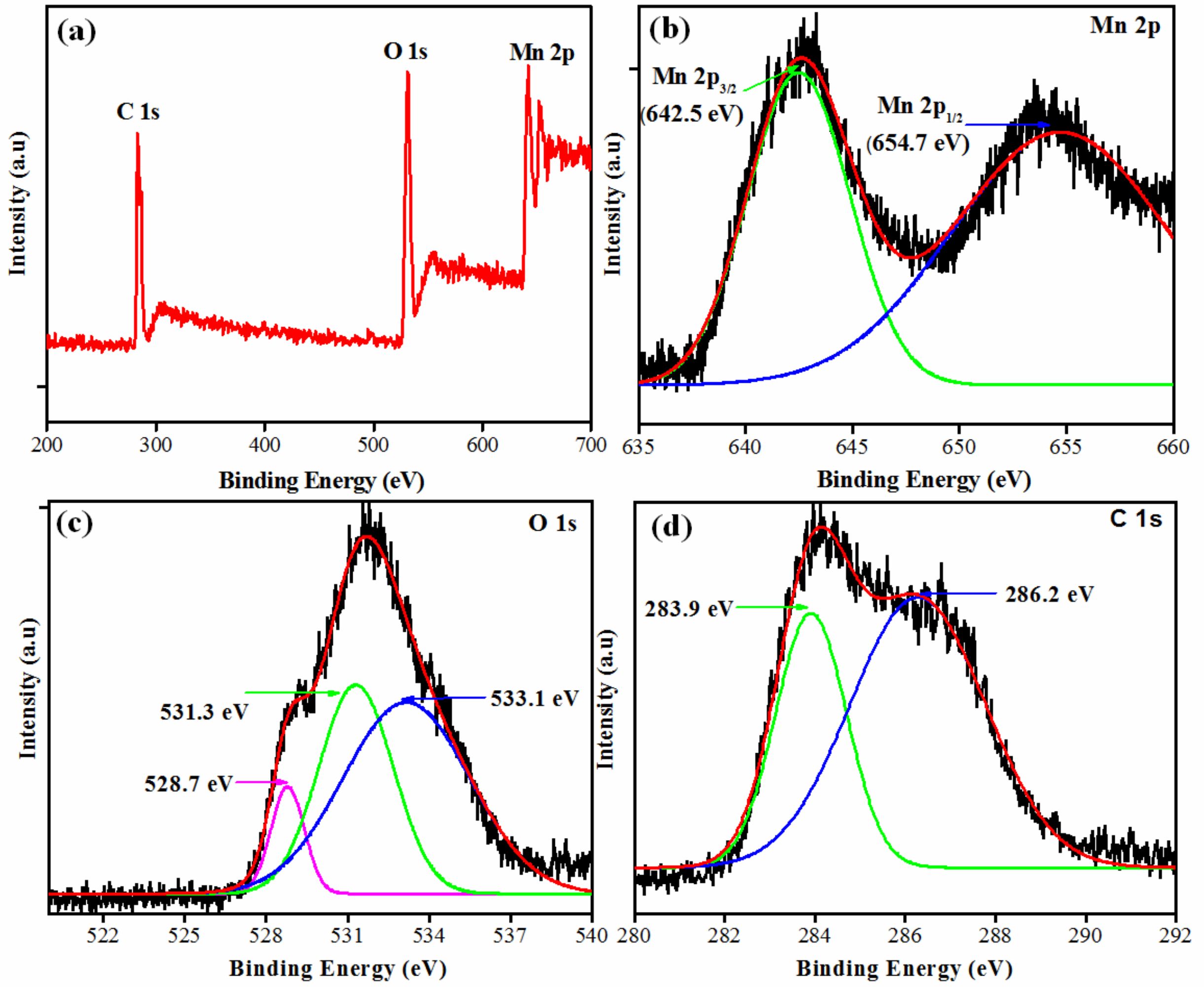

Fig. 4.3: XPS spectrum of m-MnO_2.

The HRTEM images explore faceted morphology with little aggregating nature, which may be due to the drying of the sample on the TEM grid (Fig. 4.4). The mean particle size distribution calculated by TEM analysis has been observed to be of 30-40 nm. Fig. 4.4 also shows the plot of the frequency of particles against the logarithm of size. The particle size follows the following lognormal distribution function.

$$f(d) \ = \frac{1}{\sqrt{2\pi}.\sigma.d_i} e^{-\left(\frac{(log(d_i)-\mu)^2}{2\sigma^2}\right)}$$

where $\mu = \frac{\sum log\,(d_i)}{\sum n_i}$;and $\sigma = \sqrt{\frac{\sum(log(d_i)-\mu)^2}{\sum n_i}}$

Where *f (d)* designates the lognormal distribution of particle size, d_i represents the size of an i^{th} particle of NbC, $\sum n_i$ is the total number of particles in consideration, μ is mean diameter and σ is the standard deviation of particle size. The variation in average particle size calculated by different criteria is due to the few agglomerated nanoparticles. The structure, dispersion and lattice fringes of MnO_2 nanoparticles are shown in HRTEM micrograph (Fig. 4.4) which corresponds to (101) plane with inan terplanar distance of 0.39-0.80 nm that was further supported by the SAED pattern (Fig. 4.4 (c) Inset).

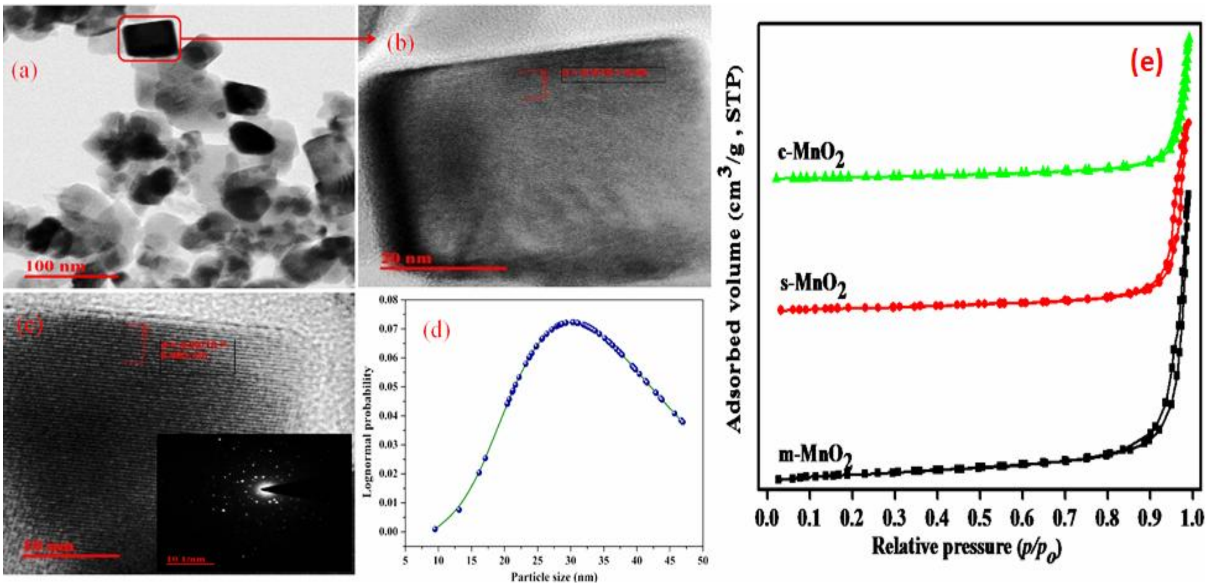

Fig. 4.4: (a-d) HRTEM images with particle size distribution plot and SAED pattern of m-MnO_2 (e) N_2 adsorption-desorption isotherms.

The N_2 adsorption-desorption isotherms and pore size distribution plot (Table 4.1) was monitored with the help of BEL mini-II, Micro Trac Corp. Pvt. Ltd, Japan. The m-MnO_2

shows highest surface area (195.3 m^2/g) and smaller pore diameter (40.48 nm) due to the charges present on the surface of surfactants as well as on metal ions (positive charge) [23].

4.3.2 Mechanism for the Synthesis of Mesoporous MnO_2

Mixed micelle formation in the aqueous phase is usually achieved when two surfactants of the different polarities are mixed. The hydrophilic polar head of cat-anionic surfactants was actively participating in the reaction which facilitates by either the electrostatic attraction or repulsion between the ions. Generally, rod-shaped micelles are formed in the case of CTAB rich corner and spherical micelles are formed in SDS rich corner. The morphology suddenly turned upon addition of equal amount of SDS into CTAB results in wormlike micelles because SDS reduces the surface potential by charge neutralization and also increment in the ionic strength is observed by an asset of the released counter ions. Thus, oppositely charged cat-anionic surfactants show enrichment in a synergistic effect over that of either parent surfactant, an effect which may be exploited in various catalytic applications[24].

4.3.3 Photocatalytic Activity

The aim of present work is to study the reactivity of m-MnO_2 by converting nitriles into amides under visible light in the weakly basic medium as well as in neutral medium. The product was isolated from the reaction mixture and characterized by GC-MS and ^{13}C NMR (Fig. 4.5) to confirm the formation of amides.

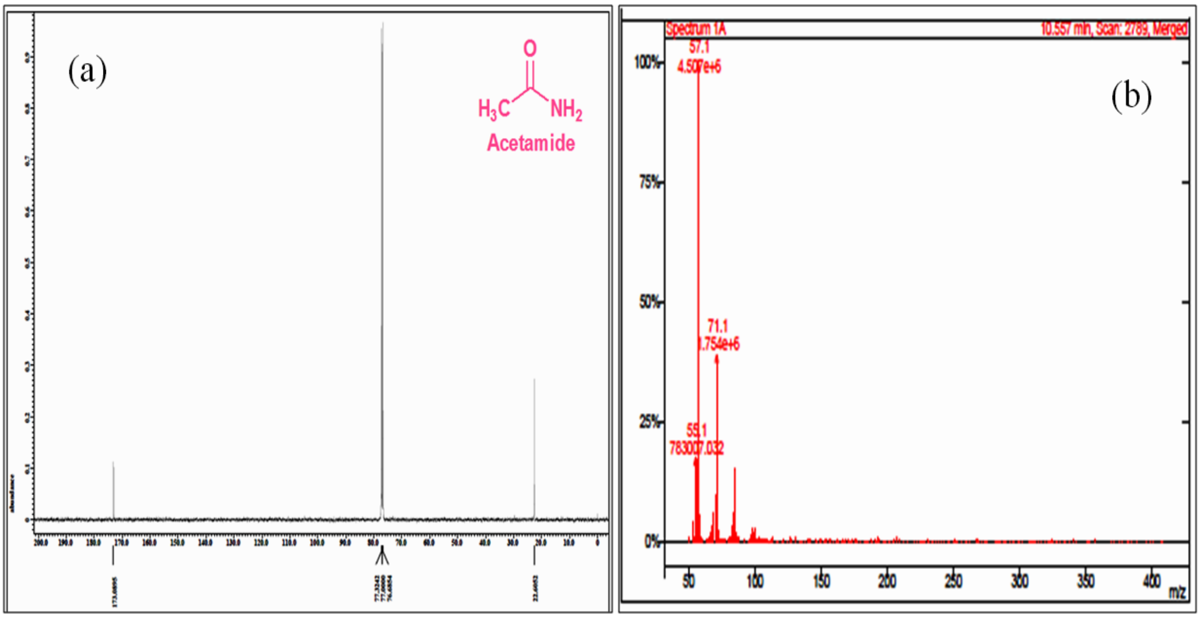

Fig. 4.5: (a) **^{13}C**-NMR spectrum of isolated acetamide in $CDCl_3$, **(b)** GC-MS spectra of the product (acetamide, as the fragmentation pattern, shows a peak at m/z 59 due to acetamide).

The yield calculated from c-MnO_2 and s-MnO_2 is around 50 % which is very less as compare to m-MnO_2 (70 - 90 %). The GC-MS spectra of the product authenticate the formation of amides from the reaction of acetonitrile. The fragmentation pattern shows, peak at m/z = 59 due to acetamide (Fig. 4.5(b)). The ^{13}C NMR spectrum shows carbonyl carbon peak at δ = 171.67 ppm and the methyl carbon peak at 22.72 ppm which authenticates the formation of acetamide (Fig. 4.5(a)). The % yield and reaction time for all the nitriles are summarized in Table 4.2. The other importance of the catalyst is its reusability, which remains constant even after 5 cycles. The photocatalyst is easily separable from the reaction mixture by centrifugation process and has no permanent adsorption of nitriles/amides over the catalyst. The % yield of the catalyst is calculated theoretically (Actual yield/theoretical yield*100) which lies in the range of 70-90 % as presented in Table 4.2.

Table 4.2: Catalytic activity of m-MnO_2 with different substrates and solvents.

Substrate	Product	Medium	Reaction Time (h)	Yield (%)
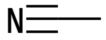 Acetonitrile	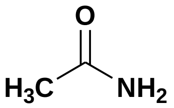 Acetamide	Triethylamine	5	90
		Water	10	75
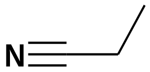 Propionitrile	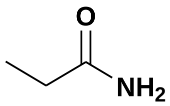 Propionamide	Triethylamine	4	88
		Water	8	72
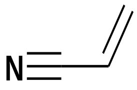 Acrylonitrile	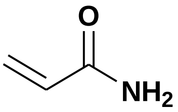 Acrylamide	Triethylamine	4	85
		Water	8	71

The reported mechanism suggests that the reaction of hydrolysis of nitriles took place in two steps [25]. The first step is the conversion of acetonitrile to acetamide and the second step is rapid hydrolysis to acetic acid. But, the brightness of m-MnO_2 catalyst falls on this point that it limits the reaction up to the formation of acetamide giving the desired product. This happens because MnO_2 confines the water molecule droplets and there is no direct hydration of amides. (hydration directly in the presence of water can undergo further hydrolysis to the acid) [26,27]. The catalytic activity of m-MnO_2 is attributed to its large surface area along with additional active sites. The proposed mechanism for the hydrolysis of nitriles to amides in a basic/neutral medium under visible light is heterogeneously catalyzed hydrolysis involving water on the surface of the catalyst, as m-MnO_2 retains moisture on its surface. The reaction of nitriles only with water (neutral medium) would be so slow (10 h) because of the poor nucleophilic nature of water and results in fewer yields (70-80 %). So, the reaction is carried out in alkaline medium (base catalyzed reaction, Fig. 4.6) to activate the nitriles group in a short period of time to get good yields (80 - 90 %).

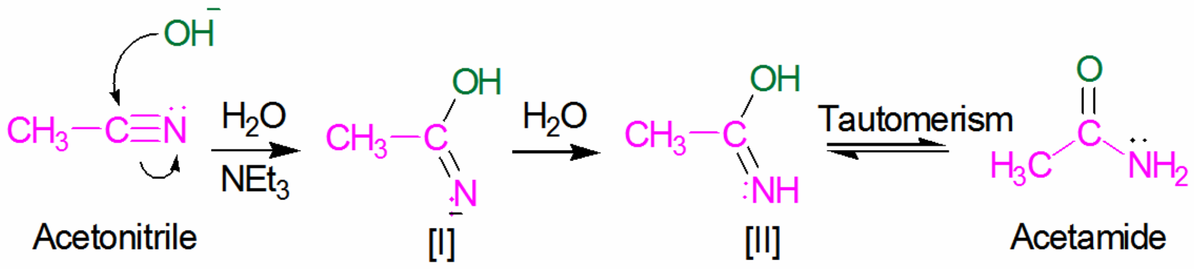

In 1st step the MnO2 which is acting as a catalyst provides water molecule with triethylamine to form transition state [I].
In 2nd step another water molecule provides proton to form intermediate state [II].
In 3rd step intermediate state [II] tautomerise to form acetamide.

Fig. 4.6: Proposed reaction mechanism for hydrolysis of nitriles to amides in basic medium.

The reaction strategy for the synthesis of m-MnO_2 is quite simple, cost-effective and is devoid of any harsh atmospheric conditions. By observing several advantages in the present strategy it can be mentioned that commercially available MnO_2 and other reported MnO_2 catalysts could not produce such effective products with good yields under the same protocol [28, 29].

References

1. Lee LV, Mitchell ML, Huang SJ, Fokin VV, Sharpless KB, Wong CH. A potent and highly selective inhibitor of human α-1, 3-fucosyltransferase via click chemistry. Journal of the American Chemical Society. 2003 Aug 13;125(32):9588-9.
2. Nawaz F, Xie Y, Cao H, Xiao J, Zhang X, Li M, Duan F. Catalytic ozonation of 4-nitrophenol over an mesoporous α-MnO_2 with resistance to leaching. Catalysis Today. 2015 Dec 1;258:595-601.
3. Mehta A, Basu S. Controlled photocatalytic hydrolysis of nitriles to amides by mesoporous MnO_2 nanoparticles fabricated by mixed surfactant mediated approach. Journal of Photochemistry and Photobiology A: Chemistry. 2017 Jun 15;343:1-6.
4. Pattabiraman VR, Bode JW. Rethinking amide bond synthesis. Nature. 2011 Dec;480(7378):471.
5. Xu F, Wang T, Li W, Jiang Z. Preparing ultra-thin nano-MnO_2 electrodes using computer jet-printing method. Chemical physics letters. 2003 Jun 25;375(1-2):247-51.
6. da Silva AG, Kisukuri CM, Rodrigues TS, Candido EG, de Freitas IC, da Silva AH, Assaf JM, Oliveira DC, Andrade LH, Camargo PH. MnO_2 nanowires decorated with Au ultrasmall nanoparticles for the green oxidation of silanes and hydrogen production under ultralow loadings. Applied Catalysis B: Environmental. 2016 May 5;184:35-43.
7. Qiu G, Huang H, Dharmarathna S, Benbow E, Stafford L, Suib SL. Hydrothermal synthesis of manganese oxide nanomaterials and their catalytic and electrochemical properties. Chemistry of Materials. 2011 Aug 2;23(17):3892-901.
8. Wang X, Yuan A, Wang Y. Supercapacitive behaviors and their temperature dependence of sol–gel synthesized nanostructured manganese dioxide in lithium hydroxide electrolyte. Journal of Power Sources. 2007 Oct 25;172(2):1007-11.
9. Lin J, Yu M, Lin C, Liu X. Multiform oxide optical materials via the versatile pechini-type sol− gel process: synthesis and characteristics. The Journal of Physical Chemistry C. 2007 Apr 26;111(16):5835-45.
10. Yan J, Fan Z, Wei T, Qian W, Zhang M, Wei F. Fast and reversible surface redox reaction of graphene–MnO_2 composites as supercapacitor electrodes. Carbon. 2010 Nov 1;48(13):3825-33.
11. Lei Y, Li J, Wang Y, Gu L, Chang Y, Yuan H, Xiao D. Rapid microwave-assisted green synthesis of 3D hierarchical flower-shaped NiCo2O4 microsphere for high-

performance supercapacitor. ACS applied materials & interfaces. 2014 Jan 30;6(3):1773-80.

12. Muraoka Y, Chiba H, Atou T, Kikuchi M, Hiraga K, Syono Y, Sugiyama S, Yamamoto S, Grenier JC. Preparation of α-MnO_2 with an Open Tunnel. Journal of Solid State Chemistry. 1999 Apr 1;144(1):136-42.
13. Xu X, Zhou X, Li X, Yang F, Jin B, Xu T, Li G, Li M. Electrodeposition synthesis of MnO_2/TiO_2 nanotube arrays nanocomposites and their visible light photocatalytic activity. Materials Research Bulletin. 2014 Nov 1;59:32-6.
14. Cheng G, Yu L, Lan B, Sun M, Lin T, Fu Z, Su X, Qiu M, Guo C, Xu B. Controlled synthesis of α-MnO_2 nanowires and their catalytic performance for toluene combustion. Materials Research Bulletin. 2016 Mar 1;75:17-24.
15. Lin T, Yu L, Sun M, Cheng G, Lan B, Fu Z. Mesoporous α-MnO_2 microspheres with high specific surface area: controlled synthesis and catalytic activities. Chemical Engineering Journal. 2016 Feb 15;286:114-21.
16. Li L, Nan C, Lu J, Peng Q, Li Y. α-MnO_2 nanotubes: high surface area and enhanced lithium battery properties. Chemical Communications. 2012;48(55):6945-7.
17. Hyeon T, Lee SS, Park J, Chung Y, Na HB. Synthesis of highly crystalline and monodisperse maghemite nanocrystallites without a size-selection process. Journal of the American Chemical Society. 2001 Dec 26;123(51):12798-801.
18. Huang M, Li F, Dong F, Zhang YX, Zhang LL. MnO_2-based nanostructures for high-performance supercapacitors. Journal of Materials Chemistry A. 2015;3(43):21380-423.
19. Roy M, Basak S, Naskar MK. Bi-template assisted synthesis of mesoporous manganese oxide nanostructures: Tuning properties for efficient CO oxidation. Physical Chemistry Chemical Physics. 2016;18(7):5253-63.
20. Zhi B, Ding H, Wang D, Cao Y, Zhang Y, Wang X, Liu Y, Huo Q. Ordered mesoporous MnO_2 as a synergetic adsorbent for effective arsenic (iii) removal. Journal of Materials Chemistry A. 2014;2(7):2374-82.
21. Saputra E, Muhammad S, Sun H, Ang HM, Tade MO, Wang S. Different crystallographic one-dimensional MnO_2 nanomaterials and their superior performance in catalytic phenol degradation. Environmental science & technology. 2013 May 22;47(11):5882-7.
22. Gao T, Fjellvåg H, Norby P. A comparison study on Raman scattering properties of α- and β-MnO_2. Analytica chimica acta. 2009 Aug 26;648(2):235-9.

23. Raghavan SR, Fritz G, Kaler EW. Wormlike micelles formed by synergistic self-assembly in mixtures of anionic and cationic surfactants. Langmuir. 2002 May 14;18(10):3797-803.
24. (a) Koehler RD, Raghavan SR, Kaler EW. Microstructure and dynamics of wormlike micellar solutions formed by mixing cationic and anionic surfactants. The Journal of Physical Chemistry B. 2000 Nov 30;104(47):11035-44.

    (b) Bakshi MS. How surfactants control crystal growth of nanomaterials. Crystal Growth & Design. 2015 Dec 30;16(2):1104-33.
25. Ma J, Zhang X, Zhao N, Xiao F, Wei W, Sun Y. Mechanism of TBD-catalyzed hydrolysis of acetonitrile. Journal of Molecular Structure: THEOCHEM. 2009 Oct 15;911(1-3):40-5.
26. Moorthy JN, Singhal N. For the hydration of nitriles to amides catalyzed by acid or base, see. J. Org. Chem. 2005;70:1926-9.
27. Cariati E, Dragonetti C, Manassero L, Roberto D, Tessore F, Lucenti E. Efficient catalytic hydration of acetonitrile to acetamide using [Os $(CO)_3Cl_2]_2$. Journal of Molecular Catalysis A: Chemical. 2003 Sep 15;204:279-85.
28. Jana S, Praharaj S, Panigrahi S, Basu S, Pande S, Chang CH, Pal T. Light-Induced Hydrolysis of Nitriles by Photoproduced α-MnO_2 Nanorods on Polystyrene Beads. Organic letters. 2007 May 24;9(11):2191-3.
29. Jana S, Basu S, Pande S, Ghosh SK, Pal T. Shape-selective synthesis, magnetic properties, and catalytic activity of single crystalline β-MnO_2 nanoparticles. The Journal of Physical Chemistry C. 2007 Nov 8;111(44):16272-7.

Enhanced photocatalytic water splitting by gold carbon dot core-shell nanocatalyst under visible/sunlight

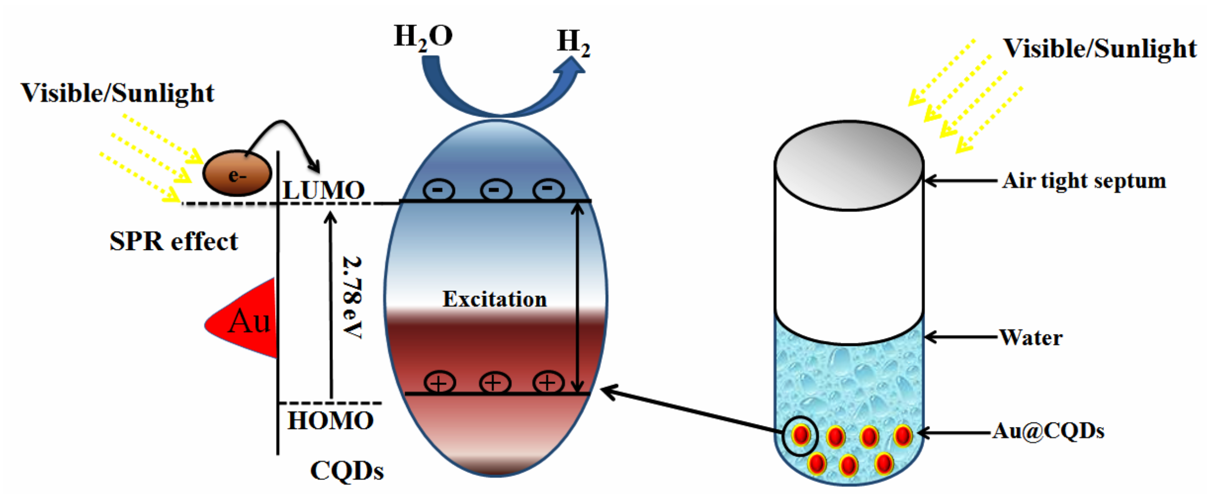

Highlights

- ➢ Fabrication of carbon quantum dots (CQDs) and core-shell Au@CQDs for the photocatalytic hydrogen generation from the water.
- ➢ The higher rate of hydrogen production for CQDs (260 μmol) and Au@CQDs (280 μmol) was observed under sunlight irradiation.
- ➢ The FRA response for Au@CQDs is very low (2.74 ohms) over that of CQDs PEs (88.8 ohms), which is otherwise 12.9 kohm for bare TiO_2 PEs.
- ➢ The photoelectrochemical response of Au@CQDs is highest amongst available reports with this family of materials reported till date.

5.1Introduction

In view of growing energy demand, hydrogen fuel is being considered as an ideal sustainable candidate owing to its zero emission and higher chemical energy per mass (142 $MJkg^{-1}$) characteristics. Its production from existing natural and renewable resources such as water and biomass further strengthens its candidature. With the introduction of Honda Fujishima's effect, a significant amount of thrust has been made to develop a cost-effective technique for hydrogen production such as photocatalysis over conventional approaches. In this direction, semiconductor materials such as metal oxides and their morphological modifications have been enormously investigated for the effective photocatalytic water splitting [1-2]. However, the achieved quantum yield is still low; therefore several efforts in terms of material and technique are being made to increase the same. Of late, carbonaceous nanostructures such as carbon nanotubes, graphene, graphene oxide, etc., have been extensively adopted due to their environmental compatibility, cost-effectiveness and rich electron transport mechanism. Kang et al. [3] demonstrated an amorphous carbon nitride photocatalyst with impressively extended visible-light-responsive range for photocatalytic hydrogen generation. Likewise, Silva et al. [4] synthesized carbon nanotubes-TiO_2 catalyst for hydrogen production from methanol and saccharides. Several other reports also advocate the effective role of carbonaceous materials in enhancing photocatalytic hydrogen production [5-6]. In recent past, carbon dots have been successfully demonstrated for water splitting due to their visible light adsorption, tunable excitation/emission characteristic, and high photostability. Yu et al. [7] synthesized carbon nanocomposites with TiO_2 for water-splitting under either UV or visible-light illumination. The observed highest hydrogen production rate was 9.1 μmol/h over neat TiO_2 photocatalyst. Xu et al. [8] developed amino conjugated carbon quantum dots to boost photocatalytic hydrogen production upto136.55 μmol for a period of 5 hours. In spite of several efforts made till date in photocatalytic hydrogen production with carbon dots (CQDs), the quantum yield is still very low under visible as well as sunlight conditions. Several reports [9-14] have suggested that the photocatalytic activity of CQDs can be improved by incorporation of noble metal (Au, Ag, and Pt) nanoparticles. These metal nanoparticles can act as an electron trap aiding the charge separation and also sensitizing the CQDs in visible light due to the localized surface plasmon resonance (LSPR) effect. Furthermore, in respect to increase visible light responsiveness of carbon dots, their interaction with noble metals like gold is proposed as best alternate, due to the fact that gold has strong affinity in visible light accredited to its plasmonic properties, as reported previously as most suitable material to sensitized several catalysts in visible/sunlight [9]. Photo electrochemical (PEC) characterization of developed photocatalytic materials further enables its possible integration in monolithic devices as PEs for solar energy conversion into hydrogen [10]. Xu et al. [8] proposed amino conjugated carbon quantum dots with an average hydrogen production rate of approximately 27.31 μmol h^{-1}. In this reference, Zhang et al.[11] demonstrated CQDs as an alternative sensitizer in PEC cells based on TiO_2 nanotube arrays. Under simulated sunlight the photocurrent density of the CQD sensitized PEC cell was observed fourfold higher than bare TiO_2 with the corresponding hydrogen production rate of about14.1 mmol h^{-1}Owing to excellent optoelectronic properties of CQDs, they not only absorb visible light but also act as collector point of photo generated electron-hole pairs. In view of the above facts, the present study was chalked out to achieve enhanced hydrogen production with Au coated CQD photocatalysts i.e. Au@CQDs. The as-synthesized Au@CQDs obtained via a facile approach are characterized for their optical, morphological, structural and photoelectrochemical characteristic and successfully demonstrated for photocatalytic and PEC measurements for hydrogen production. The reported investigation further extends as well as strengthens applicability of carbon dots towards hydrogen production as a cost-effective, stable and nontoxic material candidate.

5. 2 Experimental

5.2.1 Materials and reagents

Ascorbic acid (99%, lobachemie) and hydrogen tetrachloroaurate ($HAuCl_4$, 99%, Sigma Aldrich India) were used without further purification. Kollicoat-IR (MW 45 000Da) was gifted from BASF which was used as a stabilizing agent in the synthesis of CQDs. In-house fabricated TiO_2 coated ITO (in-house fabricated) glasses were used as a substrate to fabricate photoelectrodes (PEs). Sulphuric acid (98%), anhydrous sodium sulfate (Sisco research laboratories); potassium ferrocyanide, potassium ferricyanide and potassium chloride purchased from CDH private limited were used to carry out electrochemical measurements as well as photoelectrochemical (PEC) studies. Ultrapure deionized water obtained from Millipore (Resistance: 18 MΏ) was used for the preparation of all reagents and cleaning of glass wares**.**

5.2.2 Synthesis of Carbon dots (CQDs) and Au@CQDs

Water-soluble CQDs were synthesized by dissolving ascorbic acid and kollicoat (1:1, w/w %) under continuous stirring. After 30 minutes, the sample (5 mL) was transferred into glass reaction vessel subjected to microwave heating at 130 °C for 30 minutes at 300 W power with Multiwave-3000 microwave reaction systems (Anton Paar). The Au@CQDs was fabricated by addition of $HAuCl_4$ precursor (40 µL, 10^{-2}M) to a C-dot solution (5 mL) at room temperature. The immediate change in color of CQDs solution from yellow to pink indicated the formation of Au@CQDs.To fabricate PEs, the TiO_2 deposited ITO glasses were incubated overnight in as-prepared solution of CQDs and Au@CQDs solution under dark condition. The obtained TiO_2/CQDs and TiO_2/Au@CQDs PEs were thereafter rinsed with ultrapure deionized water, and air-dried to obtain uniform film on the substrate prior electrochemical measurements.

5.2.3 Instrumentation

The electronic excitation of CQDs and Au@CQDs were analyzed by UV–Vis spectrophotometer (Analytik Jena, Specord)and photoluminescence spectrophotometer (Perkin Elmer LS-55, excitation wavelength ranging from 290-460 nm).The structural characteristics were recorded by FTIR-spectrophotometer (Carry-660, Agilent Technologies)in 1000 to 4000 cm^{-1} range using KBr pellet technique. The morphology of as-synthesized CQDs and Au@CQDs were examined with a high resolution transmission electron microscope (HR-TEM, JEOL JE-2100 microscope)at 200kV operating voltage. The phase identification was done with X-ray diffractometer (PANALYTICAL X'Pert PRO) using Cu Kα (λ=1.540 Å) as radiation source. The electrochemical and PEC characteristic of CQDs and Au@CQDs were measured by fabricating PEs discussed above. Three electrode configurations were used to study cyclic voltammetric and impedance behaviour of the PEs in ferri/ferro redox electrolyte, wherein PEs was used as working electrode, Pt as a counter electrode and Ag/AgCl as a reference electrode.

5.2.4 Photocatalytic Performance of CQDs and Au@CQDs

The photocatalytic experiments were carried out in a sealed test tube containing catalyst (1 mL) and water/methanol mixture (1:1) for a total reaction volume of 5mL. The reaction mixture was at first degassed with Ar gas for 20 minutes to remove dissolved oxygen and then irradiated under UV (125 W Hg arc) and visible light (CFL60 W setup).The temperature of the reaction mixture was maintained by using a cold flowing water jacket attached with the reactor. The experiment was also carried out under sunlight on June 29, 2016 (Solar flux= 637 watts/m^2).The amount of hydrogen evolved during the course of the reaction was quantified by gas chromatography (Nucon, India) system equipped with molecular sieve (5x

A column) packed column and argon as a carrier gas. The temperature of the column, injector and detector was fixed at 30°C (thermal conductivity detector, TCD).The quantification was done against 200 ppm hydrogen standard. The following formula was used to calculate the solar to hydrogen conversion rates (STH):

$$\mathrm{STH}\ (\%) = \frac{\mathrm{rH_2} \times \Delta\mathrm{G}}{\text{solar flux} \times \text{Reactor surface area}}$$

rH_2 = hydrogen production rate, ΔG = 237 kJ/mol, Reactor surface area = 0.0055 m^2, Solar flux = 637 watt/m^2

5.2.5 Photo-electrochemical measurements

The photoresponse of PEs was studied by a similar three electrode configuration system discussed above. The electrolyte used was 0.1 M Na_2SO_4 maintained at pH 3 and purged with nitrogen to remove dissolved oxygen. A solar simulator equipped with 300 W Xe lamp and AM 1.5 filter was used as light source. The intensity of the source was calibrated and controlled at 100 mW/cm^2. The current density versus the potential of PEs was measured under dark and light conditions by linear scan voltammetry at 10 mVs^{-1}scan rate. Impedance spectra were recorded with frequency response analyzer and Z_{view} software at open circuit potential in the 0.1to 10^5 frequency range under 10 mV ac perturbation signal in light and dark condition. All pH measurements were made using digital pH-meter (LMPH-10, Labman Scientific Instruments Ltd).

5.3 Results and discussion

5.3.1 Plausible Mechanism for CQDs and Au@CQDs formation

The mechanism for the synthesis of CQDs by ascorbic acid involves different stages during carbonization and is quite complicated. Plausibly the reaction is expected to occur in three steps as proposed in Fig. 5.1. During 1st stage (dehydration), ascorbic acid heating endures dehydration giving rise to different soluble products such as furfural compounds and several organic acids like acetic, lactic, propionic, ketones and aldehyde [12]. The hydronium ion formed from these acids acts as a catalyst in subsequent decomposition stages and the presence of ascorbic acid controls the reaction in dehydration and decomposition step. In the 2nd stage (polymerization) the condensation and polymerization of these products lead to some soluble polymers. Since ascorbic acid is very reactive and acidic, therefore, the successful feasibility of the whole reaction is possible at a lower temperature. In the 3rd stage (aromatization), the process converts organic originator into its fundamental carbon-containing residues via microwave heating. In the last stage i.e. (passivation) carbon residues formed acquire PL properties [13-14].

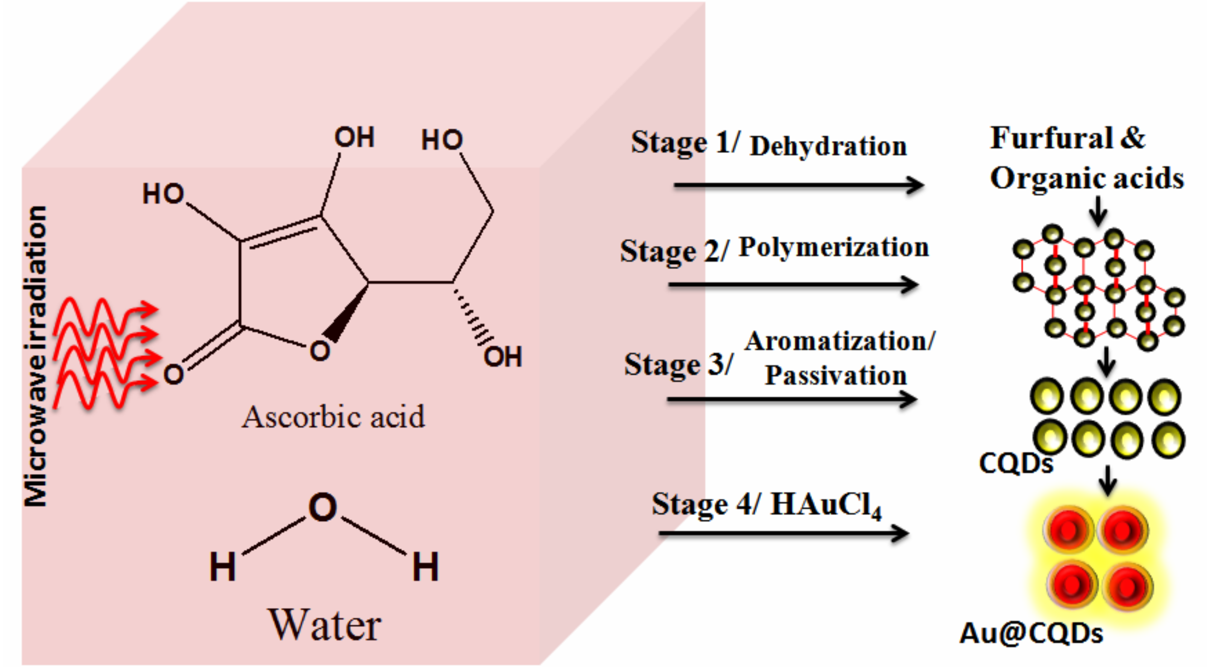

Fig. 5.1: Graphical mechanism for the formation of fluorescent CQDs and Au@CQDs nanocatalyst.

This step introduces an insulating shell on the surface, which minimizes the impact of surface defect, trap sites and direct quenching from the surrounding, which enhances the fluorescence emission. During this step, the formation of C=C double bond creates the sufficient gap between HOMO and LUMO by which electron can easily jump to LUMO and ends up as a responsible factor for high fluorescence intensity. Further, when $HAuCl_4$ was added to the solution of CQDs, the growth of Au nanoparticles was observed without any heating or photoexcitation due to the strong electronic interaction between metal and CQDs. During this procedure, the nucleation was first initiated at the sites of CQDs surface that host the electrons and the process of electron-hole recombination occurring at their surface was hindered which ultimately leads to fluorescence quenching of CQDs.

5.3.2 Characterizations of CQDs &Au@CQDs nano catalyst

The as-synthesized CQDs exhibit a broad extended peak in visible region as shown in Fig.5.2 (a).The absorption edge extending to 400 nm is only found in CQDs indicating the formation of nanocarbon. In Au@CQDs, these peaks disappear because of the strong electronic interaction between the Au and CQDs [15]. Furthermore, a characteristic surface plasmon resonance (SPR) band is observed at 528 nm for Au@CQDs, which confirms the formation of Au NPs. The optical band gap of CQDs and Au@CQDs was calculated from tau plot ($(\alpha h\nu)^2$ vs. hν) (Fig. 5.2(b)), where α, hand ν are absorption coefficient, plank constant and light frequency, respectively. The band gap for CQDs and Au@CQDs was found to be 2.78 eV and 2.68 eV, obtained by extrapolating the intercept of x-axis from the maximum slope of the curve. The charge transfer between Au and CQDs after core-shell formation results in the decrease of band gap value.

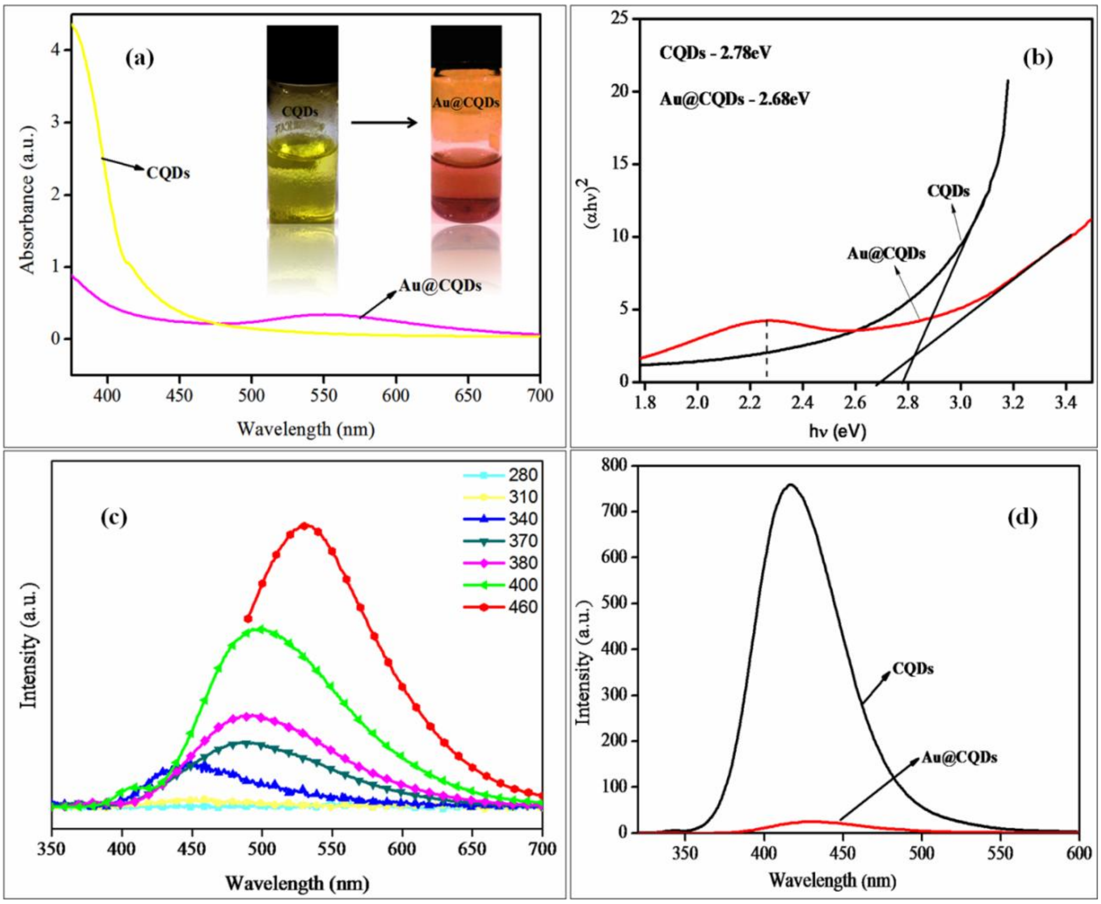

Fig. 5.2: (a) UV-visible absorption spectra and (b) $(\alpha h\nu)^2$ vs. hν curve for CQDs and Au@CQDs. (c) Effect of excitation wavelength on emission behaviour of as-synthesized CQDs and (d) comparative emission behavior of CQDs &Au@CQDs

The PL characteristic of as-synthesized CQDs showed maximum emission at 410nm excitation wavelength and exhibited a red shift on increase in excitation wavelength, which is a typical characteristic of CQDs (Fig. 5.2(c)). The evidence for the reduction of $Au^{3+}$by CQDs was also confirmed by the remarkable quenching of fluorescence emission of CQDs as shown in Fig. 5.2(d). Initially, the CQDs showed very high fluorescence due to radiative recombination of electrons and holes, which is usually confined onto their surface. Through their participation with Au^{3+}, the nucleation was initiated first at the surface sites that host the electrons, thus the process of electron-hole recombination occurring at their surface was hindered which ultimately leads to effective quenching of the fluorescence emissions.

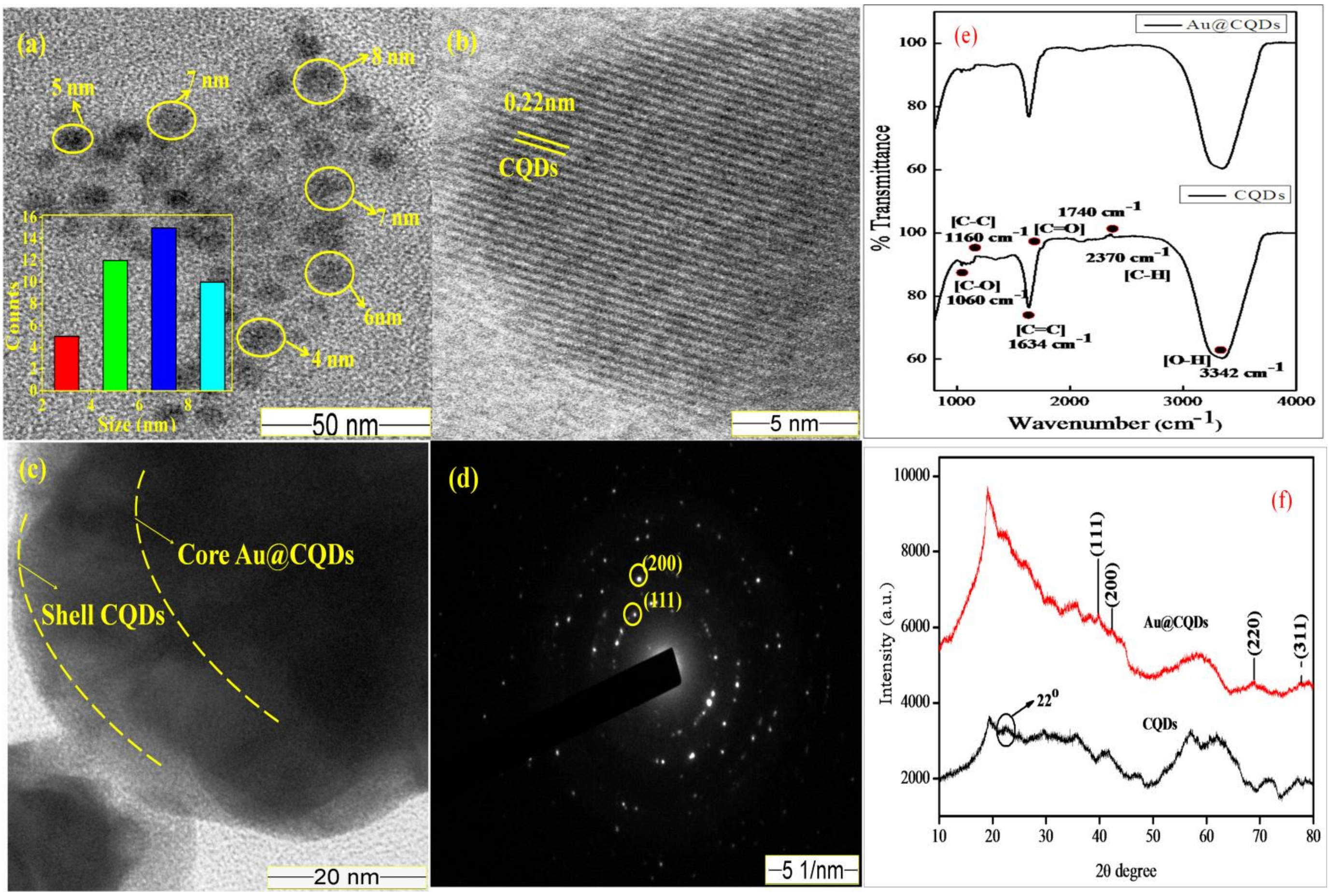

Fig. 5.3: (a) HRTEM image of CQDs inset is the size distribution of CQDs(b) HRTEM image of a single particle (c) HRTEM image of Au@CQDs (d) SAED pattern for Au@CQDs, (e) FTIR spectra of CQDs and Au@CQDs, (f) Thin film XRD-spectra of CQDs and Au@CQDs.

CQDs are known to contain covalently bonded oxygen-rich functionalities such as carbonyl, hydroxyl, carboxyl, etc., which helps CQDs dispersion in water. The FT-IR spectrum of CQDs demonstrate these characteristics feature in terms of observed stretching vibrational peak at 3342 cm^{-1},2370 cm^{-1}, 1740 cm^{-1}, 1634cm^{-1}, 1160cm^{-1} and 1060cm^{-1}, which are associated with OH,C-H ,C=O,C=C,C-C and C-O vibrations, respectively (Fig. 5.3(e)). In case of Au@CQDs, the disappearance of the peak at 2370 $cm^{-1}$and decrease in peak intensity at 1060cm^{-1}, dictates involvement of CQDs in Au nanoparticles formation or coating of CQDs with Au NPs shell [16]. Further, it is clearly evident from FT-IR spectra that part of the oxygenated groups on the CQDs was involved in the redox reaction between CQDs and Au salts.

The thin film XRD spectrum of CQDs shows a broad peak centered at $2\theta = 22^o$ (JCPDS Card Number 75- 1621) which is also attributed to highly disordered carbon atoms [17]. The crystallite size of CQDs calculated from Scherrer equation ($D = 0.9\lambda/\beta\cos\theta$) is found to be 5-7nm. In addition four well-resolved diffraction peaks at $2\theta = 38.1$, 44.2, 64.6, and 77.5° which could be assigned to the (111), (200), (220), and (311) planes of Au NPs (JCPDS Card Number 89-3697) were observed in the XRD pattern of Au@CQDs as shown in Fig. 5.3(f). Both the PL observation of the Au@CQDs and the XRD measurement pointed to the successful reduction of $HAuCl_4$ to form Au NPs during the synthesis process.

HR-TEM analysis revealed the spherical morphology of as-synthesized CQDs, with an average diameter of~7nm, which is obtained through statistical analysis for ~50 nanoparticles which was calculated by image j software (Fig. 5.3(a)). The high crystallinity for CQDs with the emergence of lattice fringes for (102) plane of graphitic sp^2 carbon is also observed (Fig. 5.3(b)). On the other hand, as observed from micrographs, a low contrast continuous layer of CQDs (shell) having thickness ~6nm wrapped with a high contrast Au core signifying the core-shell structure of Au@CQDs composite. It was observed that a cluster of Au was embedded in as prepared CQDs and the average size of Au calculated manually from the HR-TEM results was found to be ~25 nm. The SAED pattern shows the crystalline nature of Au@CQDs and ring pattern of Au metal corresponding to fcc structure.

To measure PEC characteristic of CQDs and Au@CQDs, the PEs based on them were fabricated as discussed in experimental section and characterized. The electrochemical studies disclosed that the current density of Au@CQDs PEs is several folds than CQDs PEs. Furthermore, the scan rate study of Au@CQDs PEs showed that with an increase in the scan rate, the current density increases with an anodic shift of oxidation peak and cathodic shift of reduction peak. The ratio of peak current density, i_a/i_c is found to be 1.035, indicating nearly reversible redox reaction of the Fe^{2+}/Fe^{3+}redox species at Au@CQD PEs interface. The diffusion coefficient for this reversible and diffusion controlled reversible reaction for the studied PEs was calculated using Randles–Sevcik equation [20] and is found to be 0.1169 cm^2sec^{-1} and 0.0295 cm^2sec^{-1} respectively. To further study the electron transfer kinetics dependence on scan rate (ν) at Au@CQD PEs, the areal capacitance C was calculated and found to be decreased from 0.0078 F/cm^2 to 0.0027 $F/cm^2$with respect to increased scan rate from 10 mV/s to 100 mV/s, which can be attributed to limited ionic species transport at electrode interface at higher scan rate.

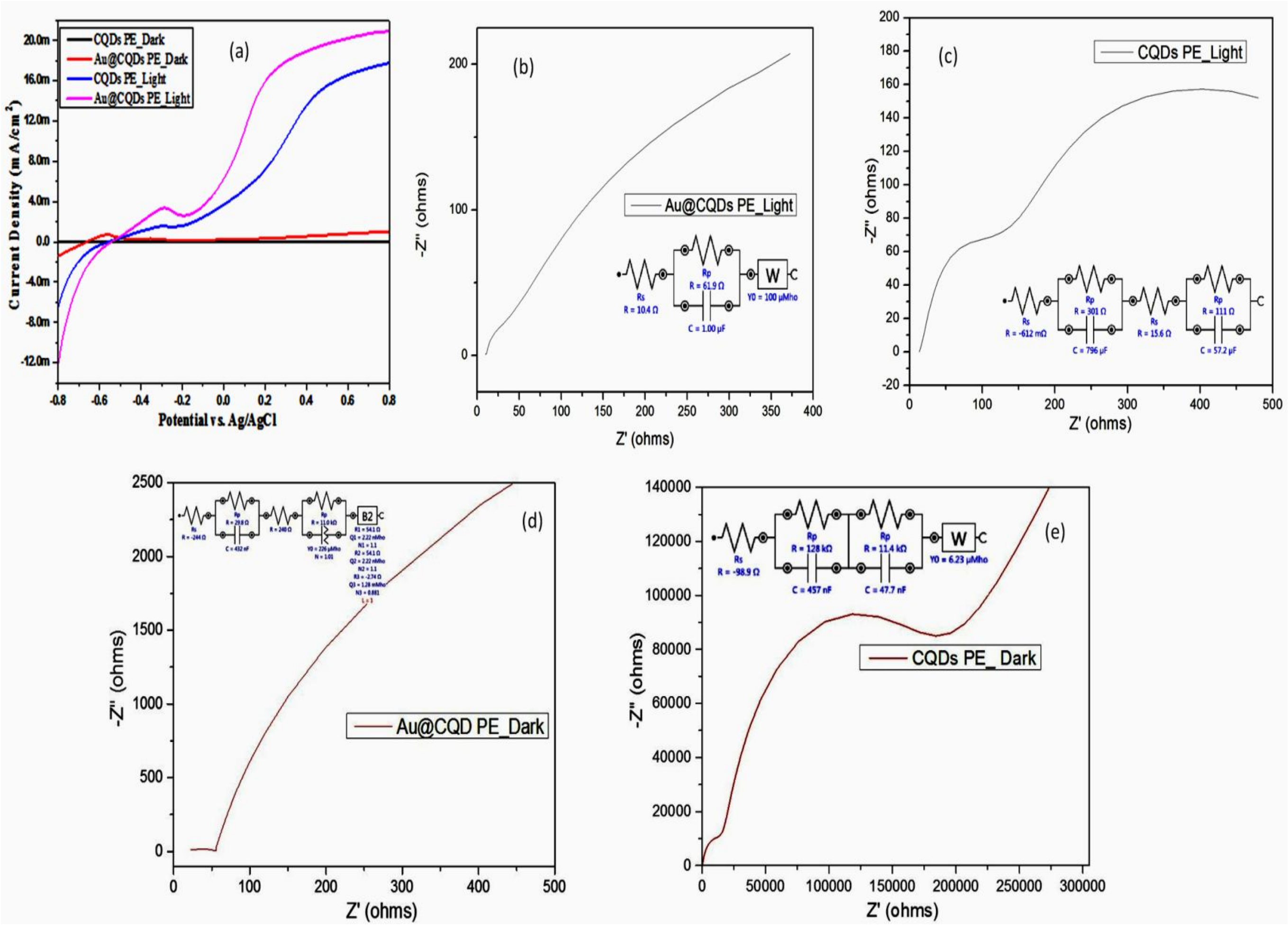

Fig. 5.4: (a) LSV behavior PEs and impedance characteristics of (b) Au@CQDs PEs and (c) CQDs PEs under light (black color) (d) Au@CQDs PEs (e) CQDs PEs under dark (red color) conditions.

Fig. 5.4(a) is associated with current density characteristic of CQDs and Au@CQDs PEs in the dark and illumination under white light of the Xe arc lamp at ~100 mW/cm^2 power density. It can be seen very clearly that current densities are negligibly small in dark condition, whereas under illumination is remarkable. The photocurrent density for Au@CQDs PEs is higher than that of CQDs PEs. It can be seen very clearly that at a very low bias of 0.16V the current densities are 16 mA/cm^2 and 6 mA/cm^2 for Au@CQDs and CQDs PEs, respectively. The photoelectrochemical response of Au@CQDs is highest amongst available reports with this family of materials reported till date [21]. Furthermore, the observed current density is multifold higher than bare TiO_2 coated PEs. To understand observed behavior impedance characteristic of both PEs were measured under light and dark condition in 3 x 10^5 to 0.1 Hz frequency range and are shown in Fig. 5.4(b,c,d,e). It can be seen clearly from FRA response and associated Randel's equivalent circuit (inset) that the polarization/charge transfer resistance for Au@CQDs is very low (2.74 ohms) over that of CQDs PEs (88.8 ohms), which is 12.9 kohm for bare TiO_2 PEs. These observations reveal the significant role played by Au layer onto CQDs interface by means of reducing electrical resistance, which could play a catalytic role in photoelectrochemical water splitting along with its light absorption properties in the visible region of the solar spectrum. The enhanced PEC performance of Au@CQDs PEs can be further understood in terms of its role as a hybrid photosensitizer to provide photoexcited electrons to the conduction band of TiO_2 particles coated onto ITO substrate thus extending visible light reactivity of the semiconductor and boosted H_2 evolution. Quantitatively the hydrogen generation is as a function of time is determined from Faraday's law of electrolysis and found to be 93.7 µmolh^{-1} (311 µmolh^{-1}cm^{-2}) and 37.5 µmolh^{-1}(125 µmolh^{-1}cm^{-2}) for Au@CQDs and CQDs PEs, respectively.

The photocurrent vs. time transient for the both PEs measured under white light illumination with 30 s light on/off cycle is displayed in Fig. 5.5 (a).Under dark condition, the PEs i.e. CQD and Au@CQDs show a negligible current response, while upon illumination, the photocurrent increases rapidly and reaches steady state values. It can be concluded very clearly that Au@CQDs exhibit very good photo-switching performance with approximately two-fold faster response in comparison with CQDs PEs. Furthermore, the performance of Au@CQDs PEs is measured for several bias potentials (Fig. 5.5 (b)) and it exhibit staircase type increased behaviour in current density as seen observed earlier in linear sweep voltammetry.

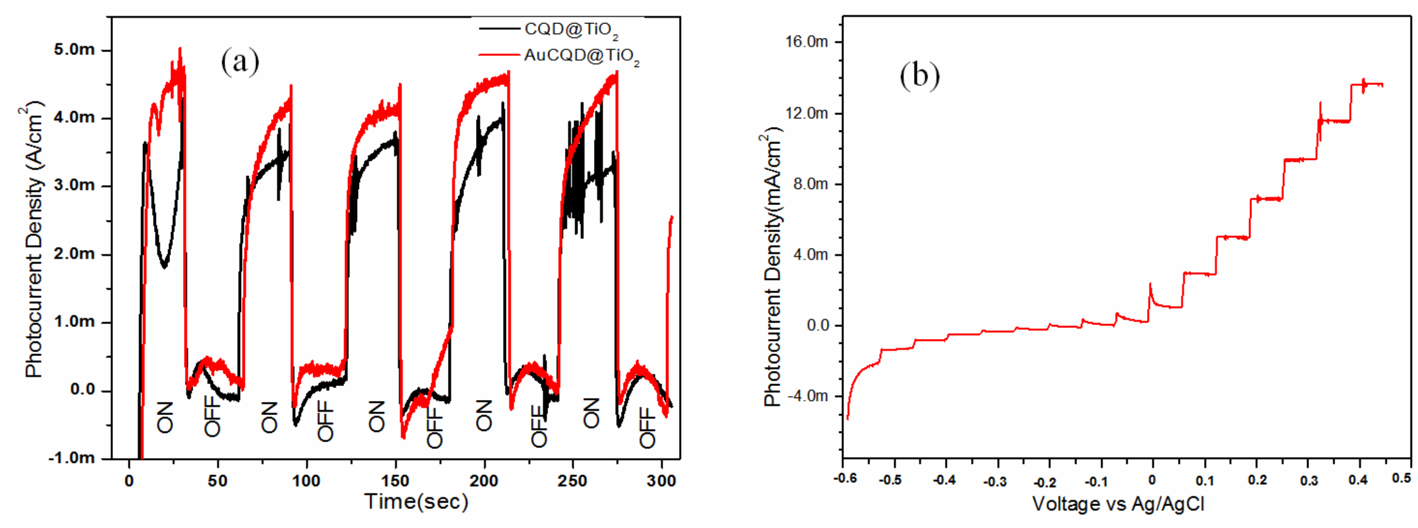

Fig. 5.5: (a) Photocurrent transient response Characteristics of PEs (b) on-off cycle curve for Au@CQDs PEs under AM 1.5 illuminations at different bias potentials.

5.3.3 Nano photocatalysis Study by CQDs and Au@CQDs

Photocatalytic water splitting experiments were performed in water using methanol as sacrificial mediator under different light sources i.e. direct sunlight, visible light and UV-light. Hydrogen evolution was not observed under UV-light irradiation due to weak optical response and the highest rate was observed under sunlight due to its good optical response.

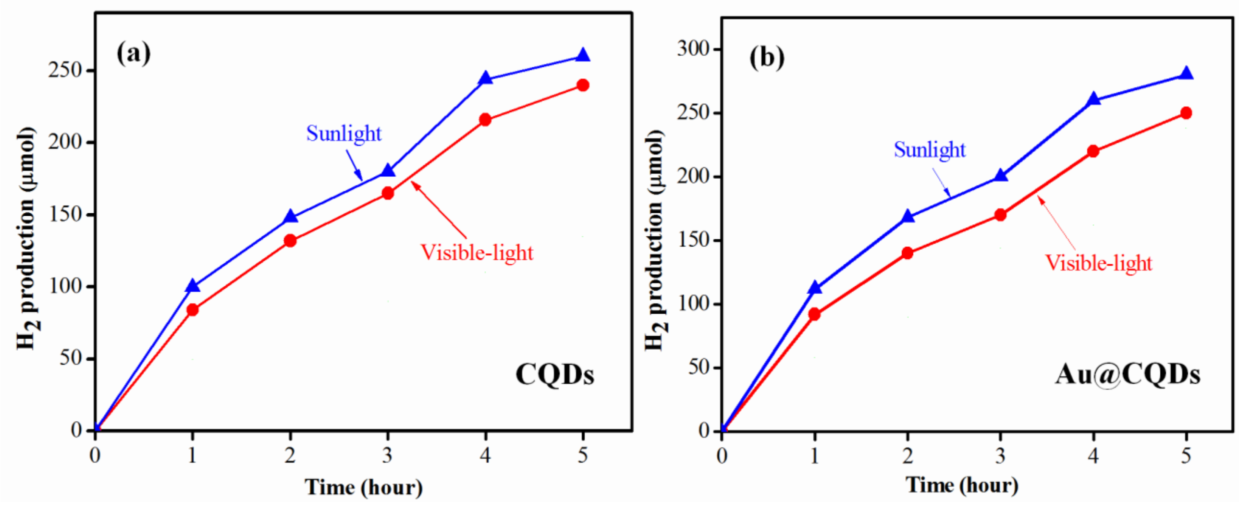

Fig. 5.6: Photocatalytic hydrogen production of (a) CQDs (b) Au@CQDs under visible light and sunlight.

As observed in Fig. 5.6 the amount of hydrogen evolved significantly increases with the reaction time under visible-light/sunlight. The hydrogen evolution rate for CQDs was 240 µmol in 5 h under visible-light source whereas it increases up to 260 µmol under sunlight. However, by the use of Au@CQDs the quite higher amount of hydrogen was evolved which was 250 µmol and 280 µmol under visible-light and sunlight respectively (Fig. 5.7). Also, the highest STH (%) was observed for Au@CQDs (1.89%) followed by CQDs (1.75%) under sunlight irradiation. There was no significant difference in the photocatalytic activity of CQD and Au@CQD because of their similar band energetic but in terms of photoelectrochemical current density, Au@CQDs showed superior activity due to effective shuttling and distribution of electrons. The photocatalytic water-splitting reactions were also studied without using Au@CQDs or light irradiation but no hydrogen was detected which confirms that hydrogen comes from the photocatalytic reactions. The role of sunlight flux on H_2 production was also studied and it was observed that the rate of H_2 production exponentially increased with the increase in sunlight flux. The average flux recorded during 5 hours of the reaction was 637 watts/m^2.

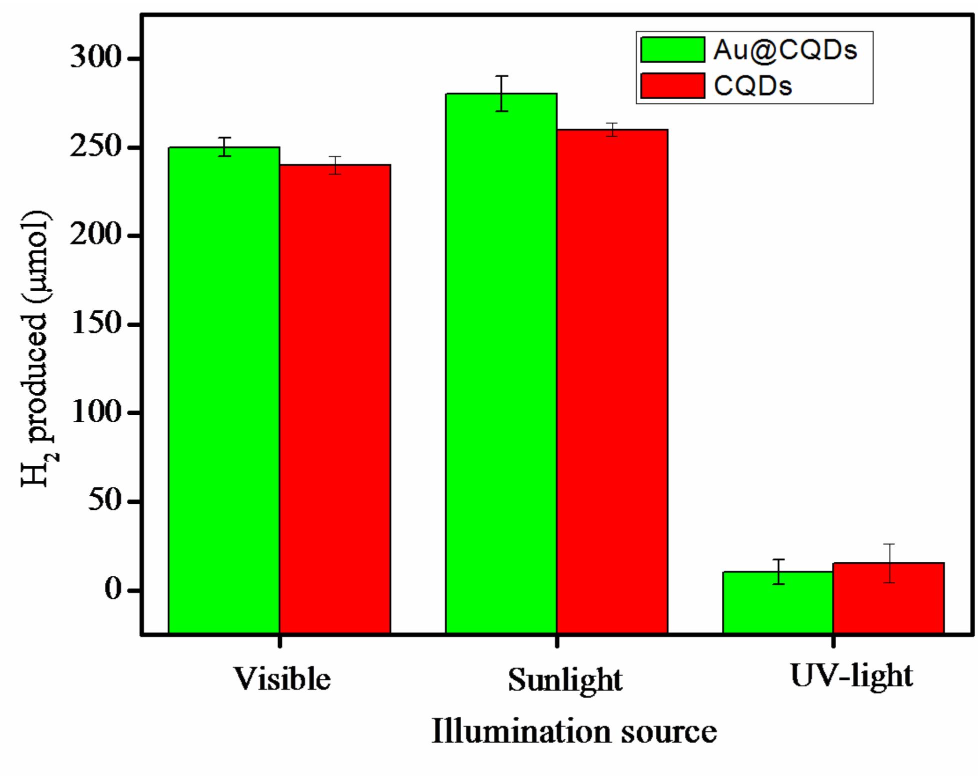

Fig. 5.7: Histogram presenting the hydrogen production of CQDs and Au@CQDs under different illumination source.

Some theoretical experimentation and calculations have confirmed that the band gap energy is dependent upon the size of CQDs [21,22]. As the size of the CQDs increases, the gap decreases gradually and HRTEM results show small sized CQDs of size 2-5 nm which agrees well with the visible light emission of CQDs [23]. Therefore, the observed photocatalytic activity is attributed to the size of the CQDs (quantum size effect). Moreover, the band gap energy for CQDs is 2.78 eV which have an excellent charge-storing ability, can also act as an electron buffer to promote the electron extraction from the conduction band and subsequently decrease the electron-hole recombination rate. Finally, CQDs can enhance electron transport because of their photoinduced electron-transfer properties. The lower PL intensity is credited to effective distribution of electron-hole pairs in order to lower the rate of recombination. Moreover, the PL quantum yield calculated in the current experiment is very low (2.23%), suggesting the participation of photo-generated electrons in CQDs for the photocatalytic reduction. Extended further to improve the photocatalytic activity, Au@CQD composite was fabricated with the band gap energy of 2.68 eV. The electron transfer properties both in case of CQDs and Au@CQDs was further elaborately investigated by photoelectrochemical studies (section 3), at a very low bias of 0.16 V the current densities were found to be 16 mA/cm^2 and 6 mA/cm^2 for Au@CQDs and CQDs PEs, which is ample for photocatalytic water splitting.

A reaction mechanism is proposed to explain the photocatalytic water splitting by Au@CQD composite in visible-light/sunlight as shown in starting schematic scheme. The Au nanoparticles absorb in the visible region because of SPR effect resulting in the generation of energetic electrons and holes. These free electrons in the intermediate energy levels act as a “color center” which can be stabilized transiently and further shuttling of photoexcited electrons to the LUMO of CQDs in visible regions. Furthermore, in case of photocatalytic hydrogen production, the reduction potential of the photocatalyst needs to be more negative vs NHE (0 V) for efficient results. Earlier [30] it has been reported that the CB or LUMO of the CQDs is -0.906 eV (versus NHE), which satisfies the thermodynamic potentials for hydrogen evolution and making it susceptible for the hydrogen production reaction. So, the photoexcited electrons in the LUMO of CQDs are thermodynamically feasible for constructive water splitting. In the view of their attractive properties, CQDs and Au@CQDs would expect to realise the efficient usage of the full spectrum of sunlight.

References

1. Chen HM, Chen CK, Chang YC, Tsai CW, Liu RS, Hu SF, Chang WS, Chen KH. Quantum dot monolayer sensitized ZnO nanowire- array photoelectrodes: true efficiency for water splitting. Angewandte Chemie. 2010 Aug 9;122(34):6102-5.

2. Yan K, Wu G. Titanium dioxide microsphere-derived materials for solar fuel hydrogen generation. ACS Sustainable Chemistry & Engineering. 2015 Apr 21;3(5):779-91.

3. Kang Y, Yang Y, Yin LC, Kang X, Liu G, Cheng HM. An Amorphous Carbon Nitride Photocatalyst with Greatly Extended Visible- Light- Responsive Range for Photocatalytic Hydrogen Generation. Advanced Materials. 2015 Aug 1;27(31):4572-7.

4. Silva CG, Sampaio MJ, Marques RR, Ferreira LA, Tavares PB, Silva AM, Faria JL. Photocatalytic production of hydrogen from methanol and saccharides using carbon nanotube-TiO_2 catalysts. Applied Catalysis B: Environmental. 2015 Nov 30;178:82-90.

5. Xiang Q, Yu J, Jaroniec M. Preparation and enhanced visible-light photocatalytic H_2-production activity of graphene/C_3N_4 composites. The Journal of Physical Chemistry C. 2011 Mar 30;115(15):7355-63.

6. Pragathiswaran C, Abbubakkar BM, Govindhan P, Abuthahir KS. Journal of Applicable Chemistry. Journal of Applicable Chemistry. 2015;4(2):525-32.

7. Yu H, Zhao Y, Zhou C, Shang L, Peng Y, Cao Y, Wu LZ, Tung CH, Zhang T. Carbon quantum dots/TiO_2 composites for efficient photocatalytic hydrogen evolution. Journal of Materials Chemistry A. 2014;2(10):3344-51.

8. Xu X, Bao Z, Zhou G, Zeng H, Hu J. Enriching photoelectrons via three transition channels in amino-conjugated carbon quantum dots to boost photocatalytic hydrogen generation. ACS applied materials & interfaces. 2016 May 24;8(22):14118-24.

9. Tabata M, Maeda K, Ishihara T, Minegishi T, Takata T, Domen K. Photocatalytic hydrogen evolution from water using copper gallium sulfide under visible-light irradiation. The Journal of Physical Chemistry C. 2010 Jun 4;114(25):11215-20.

10. Jia T, Kolpin A, Ma C, Chan RC, Kwok WM, Tsang SE. A graphene dispersed CdS–MoS_2 nanocrystal ensemble for cooperative photocatalytic hydrogen production from water. Chemical communications. 2014;50(10):1185-8.

11. Xiang Q, Cheng F, Lang D. Hierarchical Layered WS_2/Graphene- Modified CdS Nanorods for Efficient Photocatalytic Hydrogen Evolution. ChemSusChem. 2016 May 10;9(9):996-1002.

12. Zhang LJ, Zheng R, Li S, Liu BK, Wang DJ, Wang LL, Xie TF. Enhanced photocatalytic H_2 generation on cadmium sulfide nanorods with cobalt hydroxide as cocatalyst and insights into their photogenerated charge transfer properties. ACS applied materials & interfaces. 2014 Aug 18;6(16):13406-12.

13. Lang D, Cheng F, Xiang Q. Enhancement of photocatalytic H_2 production activity of CdS nanorods by cobalt-based cocatalyst modification. Catalysis Science & Technology. 2016;6(16):6207-16.

14. Pan X, Xu YJ. Graphene-Templated Bottom-up Fabrication of Ultralarge Binary CdS–TiO2 Nanosheets for Photocatalytic Selective Reduction. The Journal of Physical Chemistry C. 2015 Mar 11;119(13):7184-94.

15. Spoto G, Minunni M. Surface plasmon resonance imaging: what next?. The journal of physical chemistry letters. 2012 Sep 10;3(18):2682-91.

16. Li J, Gao X, Liu B, Feng Q, Li XB, Huang MY, Liu Z, Zhang J, Tung CH, Wu LZ. Graphdiyne: A metal-free material as hole transfer layer to fabricate quantum dot-sensitized photocathodes for hydrogen production. Journal of the American Chemical Society. 2016 Mar 18;138(12):3954-7.

17. Zhang X, Wang F, Huang H, Li H, Han X, Liu Y, Kang Z. Carbon quantum dot sensitized TiO_2 nanotube arrays for photoelectrochemical hydrogen generation under visible light. Nanoscale. 2013;5(6):2274-8.

18. Sahu S, Behera B, Maiti TK, Mohapatra S. Simple one-step synthesis of highly luminescent carbon dots from orange juice: application as excellent bio-imaging agents. Chemical Communications. 2012;48(70):8835-7.

19. Sevilla M, Fuertes AB. The production of carbon materials by hydrothermal carbonization of cellulose. Carbon. 2009 Aug 1;47(9):2281-9.

20. Hu B, Wang K, Wu L, Yu SH, Antonietti M, Titirici MM. Engineering carbon materials from the hydrothermal carbonization process of biomass. Advanced Materials. 2010 Feb 16;22(7):813-28.

21. Mandani S, Sharma B, Dey D, Sarma TK. Carbon nanodots as ligand exchange probes in Au@C-dot nanobeacons for fluorescent turn-on detection of biothiols. Nanoscale. 2015;7(5):1802-8.

22. Jia X, Li J, Wang E. One-pot green synthesis of optically pH-sensitive carbon dots with upconversion luminescence. Nanoscale. 2012;4(18):5572-5.

23. Zhu S, Meng Q, Wang L, Zhang J, Song Y, Jin H, Zhang K, Sun H, Wang H, Yang B. Highly photoluminescent carbon dots for multicolor patterning, sensors, and bioimaging. Angewandte Chemie. 2013 Apr 2;125(14):4045-9.

24. Gregoriou VG, Rodman SE. Quantitative depth profile analysis of micrometer-thick multilayered thin coatings using step-scan FT-IR photoacoustic spectroscopy. Analytical chemistry. 2002 May 15;74(10):2361-9.

25. Mathew S, kumar Prasad A, Benoy T, Rakesh PP, Hari M, Libish TM, Radhakrishnan P, Nampoori VP, Vallabhan CP. UV-visible photoluminescence of TiO_2 nanoparticles prepared by hydrothermal method. Journal of fluorescence. 2012 Nov 1;22(6):1563-9.

26. Liu J, Liu Y, Liu N, Han Y, Zhang X, Huang H, Lifshitz Y, Lee ST, Zhong J, Kang Z. Metal-free efficient photocatalyst for stable visible water splitting via a two-electron pathway. Science. 2015 Feb 27;347(6225):970-4.

27. Yu X, Liu R, Zhang G, Cao H. Carbon quantum dots as novel sensitizers for photoelectrochemical solar hydrogen generation and their size-dependent effect. Nanotechnology. 2013 Jul 26;24(33):335401.

28. Li H, He X, Kang Z, Huang H, Liu Y, Liu J, Lian S, Tsang CH, Yang X, Lee ST. Water- soluble fluorescent carbon quantum dots and photocatalyst design. Angewandte Chemie International Edition. 2010 Jun 14;49(26):4430-4.

29. Martindale BC, Hutton GA, Caputo CA, Reisner E. Solar hydrogen production using carbon quantum dots and a molecular nickel catalyst. Journal of the American Chemical Society. 2015 Apr 28;137(18):6018-25.

30. Yang P, Zhao J, Wang J, Cui H, Li L, Zhu Z. Pure carbon nanodots for excellent photocatalytic hydrogen generation. RSC Advances. 2015;5(27):21332-5.

Optical Detection of Thiol Drugs by Core-Shell Luminous Carbon Dots-Gold Nanoparticles System

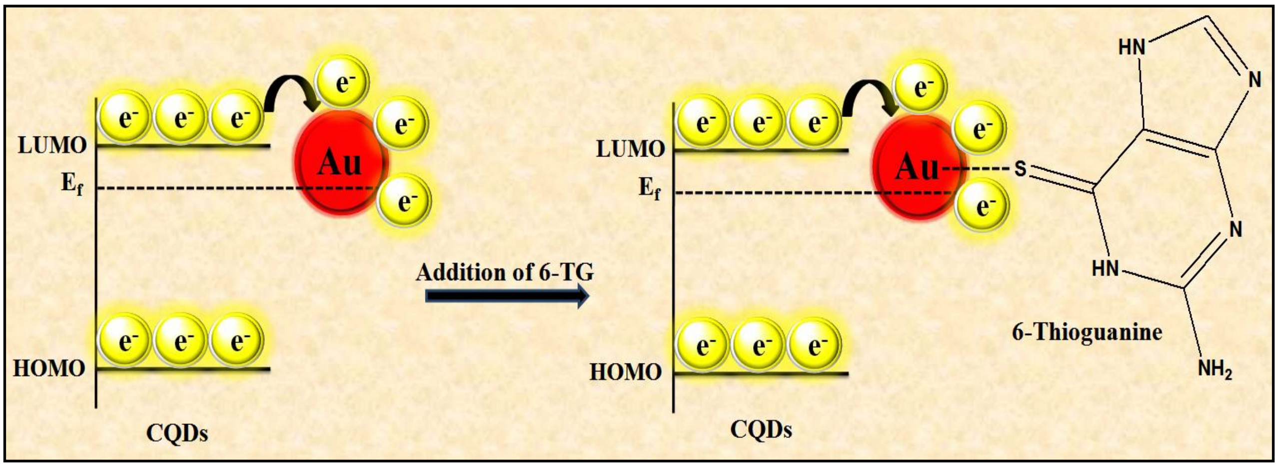

Highlights

- Fabrication of carbon quantum dots (CQDs) by simple one-step microwave technique.
- The CQDs were further used for making core-shell (Au@CQDs) nanocomposites within 5 seconds.
- The Au@CQDs could act as a biosensor for detection of various amino acids, enzymes and pentids.
- A detailed investigation into the course of fluorescence turn off/on of CQDs shows positive results.

6.1 Introduction

Noble metal (Au, Ag etc) based plasmonic nanoparticles (NPs) have gained incredible significance as colorimetric sensors due to their distinctive and excellent characteristics like distance-dependent optical properties and high extinction coefficients in visible region [1-10]. These metal NPs are known as excellent fluorescence quenchers and their quenching effect has been thoroughly explored on various fluorophores. In addition, these NPs have a huge number of applications in the field of sensing and nano-medicine [11-15]. Fluorescence quenching by the metal NPs is generally a type of energy transfer method taking place among the fluorophores and NPs. The composite formation of these metallic NPs with other active materials has been reported to be efficient in several advanced sensing and biomedical applications. But the composite formation with the quantum dot is least studied and composite materials of such scale can be effective because of alteration in optoelectronic properties.

Recently composites with photoluminescent nanomaterials had gained interest due to their applicability in various fields, ranging from biomedical to optoelectronics fields [16-17]. One new category of luminescent nanomaterials is carbon quantum dots (CQDs). CQDs are a rising category of carbon nanomaterial due to their impressive fluorescence property, good biocompatibility, photo stability, energy conversion capability and water solubility. The great interest towards this small water-soluble type of carbon could be credited to its character as eco-friendly and non-toxic nature, as an alternative to semiconductor quantum dots in diverse applications like electronics, drug delivery and catalysis [18, 19]. The existence of carboxylic moiety onto the surface of CQDs has the ability to function both as a reducing and stabilizing agents in the fabrication of metallic NPs, similar with other carboxyl enriched ligands like citrates, ascorbates [20-21] etc. If CQDs are able to create a shell surrounding the metal NPs, it may function like a self-assembled monolayer of stabilizing agent [22]. In the existence of these metal NPs, the fluorescence emission of these CQDs can be notably quenched as a result of energy transfer. When any biological moiety introduced into CQDs–metal NPs system the fluorescence is again regained due to the interaction of moiety with Au NPs leading to aggregation of NPs. The applicability of CQDs–metal NPs system can thus be exploited for turn-on fluorescence detection of purine compounds.

Purine compounds have a significant role in human cell metabolism and the compounds are also utilized to treat cancer [23]. As an example the 6-thioguanine (6-TG) is useful as an anticancer agent, to enhance immune response and also in the treatment of leukemia at advanced stages [24]. The 6-TG is hastily activated inside the body via intracellular conversion to its nucleotide, thioguanylic acid and its thioguanosine phosphate derivatives [25]. At present, many of the available methods for the determination of 6-TG involves expensive biological reagents, sophisticated instrumentation and cumbersome sample preparation. Therefore, the improvement of a novel, sensitive, fast and simple practical method is still in a great demand. In this context, we report the development of core-shell AuNPs-CQDs (Au@CQDs) nanocomposite as fluorometric nanosensor for the detection of 6-TG which works by the combination of ligand exchange and Förster resonance energy transfer (FRET) phenomena. This method is better or has comparable performance than most of the other methods, moreover CQDs are very inexpensive and environmental friendly probe and in addition, its interaction with metal NPs has not been extensively studied previously.

6.2 Experimental Section

6.2.1 Reagents

Hydrogen tetrachloroaurate ($HAuCl_4$, 99%, Sigma Aldrich India), ascorbic acid (99%, lobachemie) were used without further purification. Kollicoat-IR (MW 45000Da) was gifted from BASF, 6-Thioguanine (98%, Alfa Aesar) was used as a model compound for fluorescence turn-on detection. The ultrapure water from Millipore (Resistance: 18 MΏ) was used throughout the experiment and for making the solution.

6.2.2 Synthesis of CQDs and Au@CQDs

The CQDs were synthesized by a simple microwave method (Fig. 6.1). Briefly, 0.5 g of ascorbic acid and kollicoat (1:1 w/w %) was dissolved in water under continuous stirring. After 20 minutes the sample (5 mL) was pipetted out into glass reaction vessel and heated in a microwave synthesizer (Multiwave 3000 Microwave Reaction System, Anton Paar). The reaction was carried out at a temperature of 130 °C for 30 minutes at 300 W powers. The yellow color of the mixture confirmed the formation of CQDs. The Au@CQDs is fabricated by addition of $HAuCl_4$ precursor (50 µL) to the C-dot solution (1 mL) at room temperature. The color change from yellow to pink within 5 seconds was observed indicating the formation of Au@CQDs.

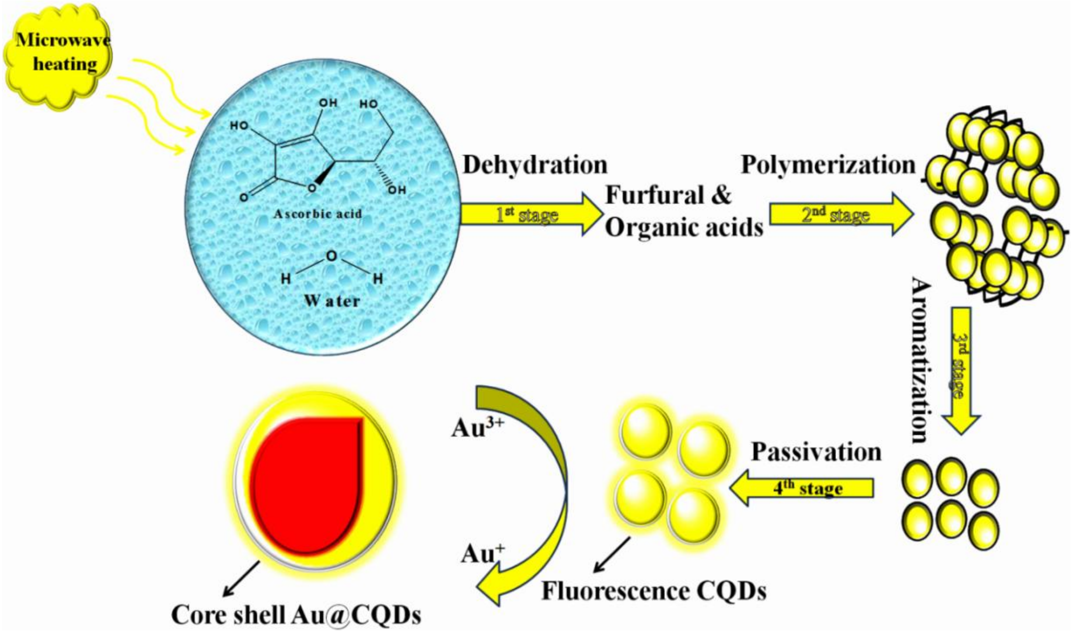

Fig. 6.1: Graphical mechanism for the formation of fluorescence CQDs and core-shell Au@ CQDs.

6.2.3 Assay of 6-Thioguanine

The fluorescence detection of 6-TG was performed in ultrapure water. Different concentration of 6-TG was mixed with 1 mL of Au@CQDs nanocomposites and incubated for 2 minutes at room temperature. The photoluminescence (PL) signal was investigated by the fluorescent spectrometer at an excitation wavelength of 320 nm. For the kinetic study, the fluorescence recovery of samples was examined at different incubation time (0-120 seconds).

6.2.4 Instrumentation

The electron excitation of CQDs and Au@CQDs was analyzed using UV–Vis spectrophotometer (Analytik Jena, Specord). The PL emission spectrum was recorded by fluorescent spectrophotometer (Perkin Elmer) at different excitation wavelength ranging from 290-460 nm. The phase identification was analyzed through XRD analysis **(**PANALYTICAL X’Pert PRO) with Cu Kα **(**λ=1.540 Å) as radiation source over the range $10° \leq 2\theta \leq 90°$. Fourier transforms infrared (FTIR) spectra were measured on the Perkin Elmer PE-983 FTIR spectrophotometer. Transmission electron microscopy (HRTEM) analysis was carried out on JEOL JE-2100 microscope under the accelerating voltage of 200 kV. Particle size distribution and zeta potential were determined by dynamic light scattering method (DLS, Zetasizer, Malvern). The oxidation state of the photocatalyst was analyzed by X-ray photon spectroscopy (XPS, KRATOS Axis 165 Shimadzu, UK) with Mg Ka radiation (1252.6 eV at 75 W).

6.3 Results and Discussion

6.3.1Characterization of CQDs and Au@CQDs

The optical properties and morphology of CQDs and Au@CQDs were already explained in Chapter 5. The average hydrodynamic size has been found to be 7 nm for CQDs which is in accordance with HRTEM and XRD results (Fig. 6.2(a)). While the participation of Au^{3+} leads to agglomeration resulting in the increase of the size distribution up to 90 nm (Fig. 6.2(b)). The zeta potential value for CQDs and Au@CQDs were observed to be -0.318 mV and -0.628 mV respectively which confirm the negative charge on its surfaces.

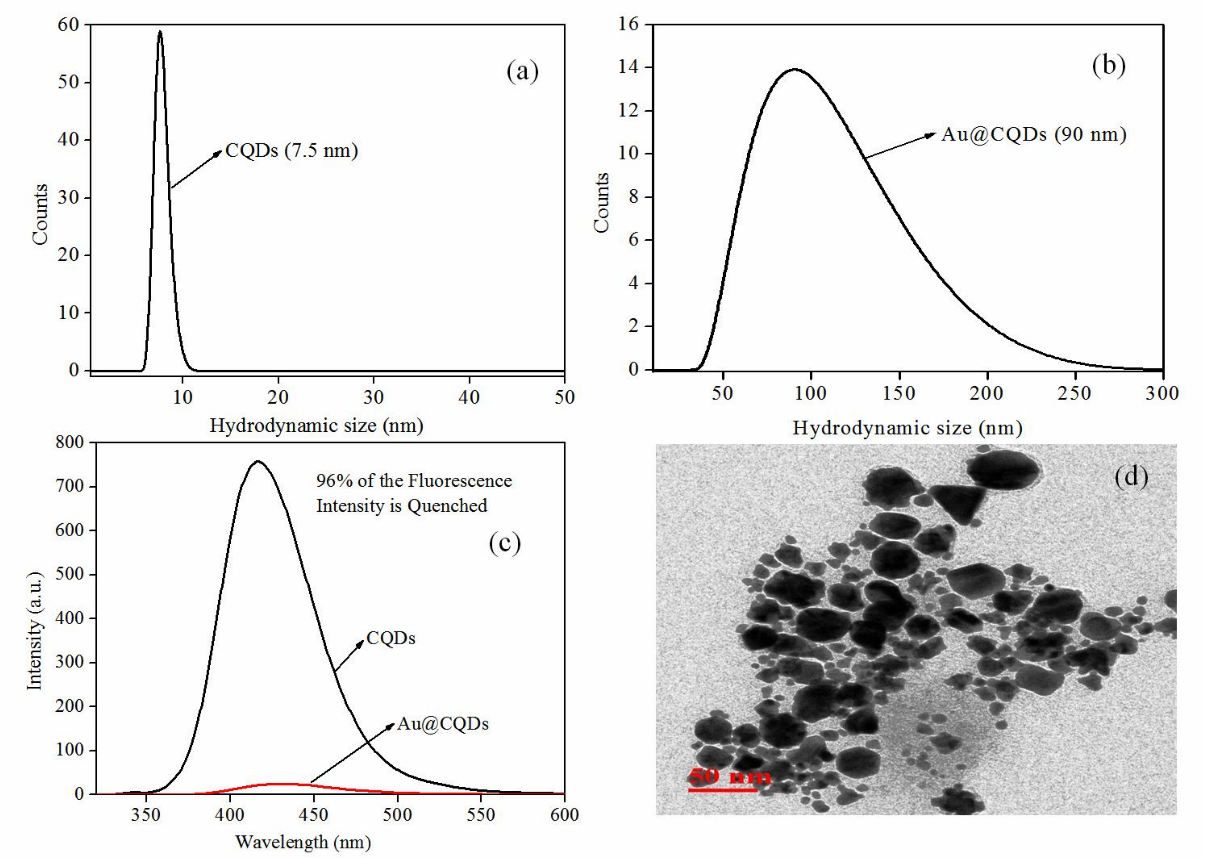

Fig. 6.2: DLS spectra for (a) CQDs (b) Au@CQDs (c) Emission spectrum of CQDs and Au@CQDs (d) TEM image of the Au@CQDs showing aggregation after the addition of 6-TG

XPS measurements were performed to determine the composition of CQDs. As shown in Fig. 6.3 the C 1s and O 1s peaks are the two major elements observed for CQDs. The high-resolution C 1s peak is deconvoluted into two signals, which includes the (sp^2) C-C and C-O-C bond at 283.4 and 285 eV. These results show that pure CQDs contain only oxygenic groups which are in agreement with FTIR results.

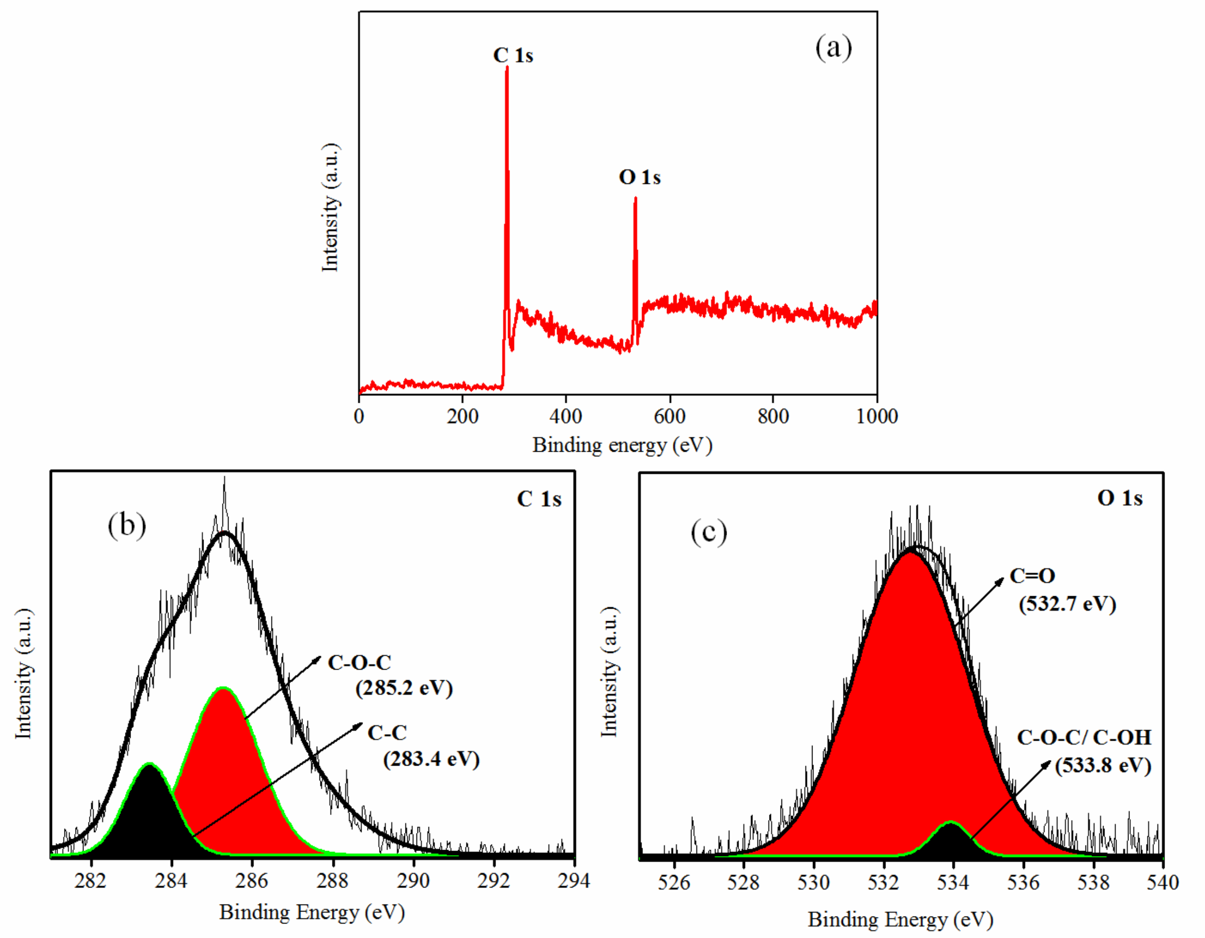

Fig. 6.3: (a) XPS survey of CQDs (b) C 1s (c) O 1s spectrum of CQDs.

6.3.2 Fluorescence Turn-off of CQDs by AuNPs

The CQDs show maximum emission when excited at 410 nm and PL also shifted to longer wavelength with increasing excitation wavelength, typical characteristics of CQDs [23]. The confirmation for the reduction of Au^{3+} salts by CQDs was observed by the fluorescence quenching (Fig. 6.2 (c)). Initially, the CQDs showed very high fluorescence due to radiative recombination of electrons and holes which are usually confined onto their surface and by the interaction of CQDs with Au^{3+} the electrons and holes are being trapped and become less available for the radiative recombination which ultimately leads to PL quenching. The fluorescence intensity of CQDs decreases considerably with the increasing amount of AuNPs concentration, demonstrating an efficient quenching procedure. Fluorescence quenching data are usually represented by Stern-Volmer equation which gives the plot between F_0/F vs. concentration of the quencher and is represented as:

$$F_0/F = 1+K_{SV}\,[Au]$$

Here, F_0 and F are the fluorescence intensity of CQDs in the absence and presence of quencher [Au], K_{SV} is the stern Volmer constant (M^{-1}). The plot is represented in Fig. 6.4(a) and the corresponding value of K_{SV} is calculated to be 5.2×10^{-4} M^{-1} indicating high quenching efficiency.

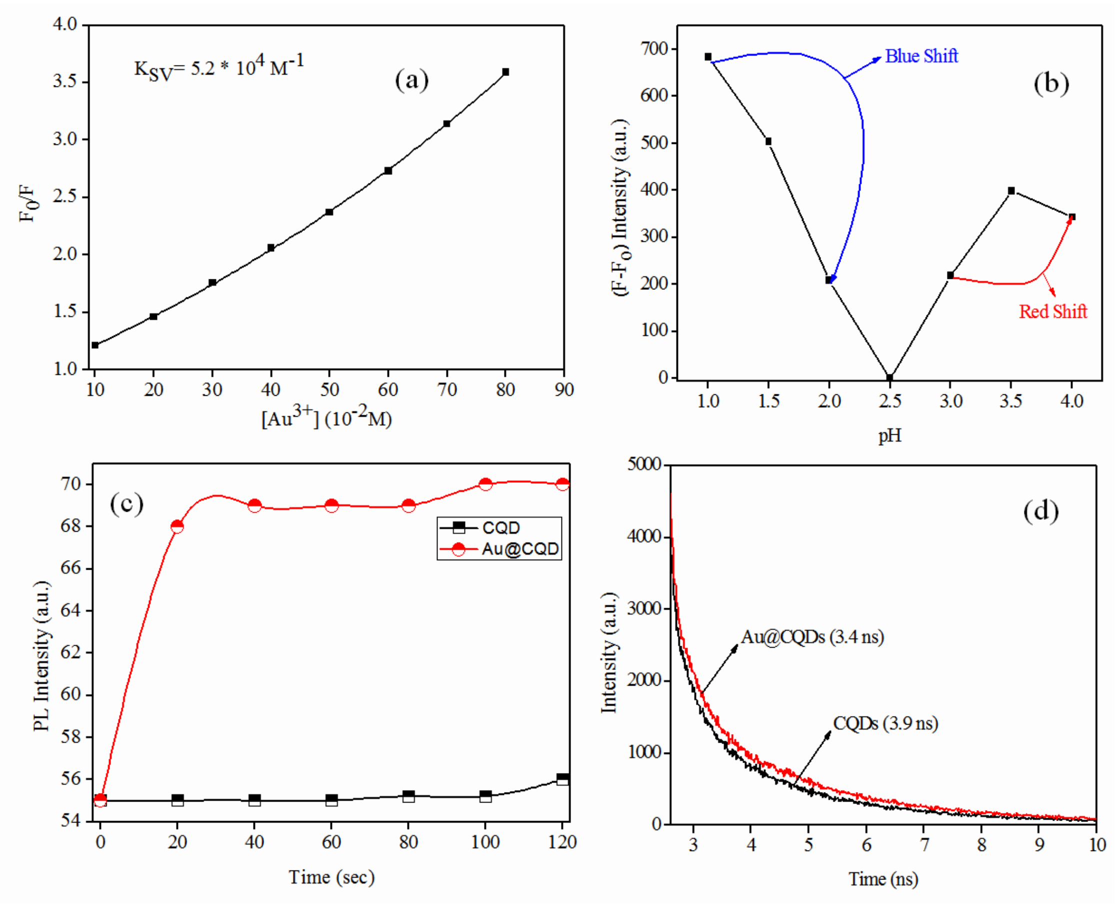

Fig. 6.4: Plot between (a) Stern-Volmer plot for the quenching of CQDs fluorescence at various concentrations of Au^{3+}; (b) enhanced fluorescence intensity (F-F_0, where F and F_0 are fluorescence intensities in the presence and absence of 6-TG respectively) vs. pH (c) PL intensity vs. time (kinetic study) (d) PL lifetime decay curves for CQDs and Au@CQDs.

6.3.3 Photostability of CQDs

Before carrying out the practical application for the sensing of 6-Thioguanine (6-TG) the stability of CQDs was done by the UV (125 W Hg arc) and visible light (CFL 60 W) irradiation for 60 minutes and no change was observed in the fluorescence intensity signifying the good photostability.

6.3.4 Accession of Critical Parameters for Sensing of 6-TG

6.3.4.1 Testing at Different pH and Colour

The restored fluorescence efficiency of CQDs is highly dependent upon the pH value. The influence of pH on enhanced fluorescence intensity was studied in the range of 1.0 to 4.0 as shown in Fig. 6.4(b). The solution of nitric acid (1 N) and sodium hydroxide (1 N) were used for adjusting the pH of the solution. The pH of the original mixture [Au@CQDs+6-TG (60 μM)] was found to be 2.5. The highest response was found at pH 1.5. It seems that at this value the interaction of Au@CQDs with 6-TG is highest. At the higher concentration of acidic/basic medium, it may cause the aggregation of Au@CQDs which leads to less interaction with 6-TG. Also, it was clearly seen that with the increase in the H^+ concentration blue shift was observed and with the increase in OH^- concentration red shift was observed.

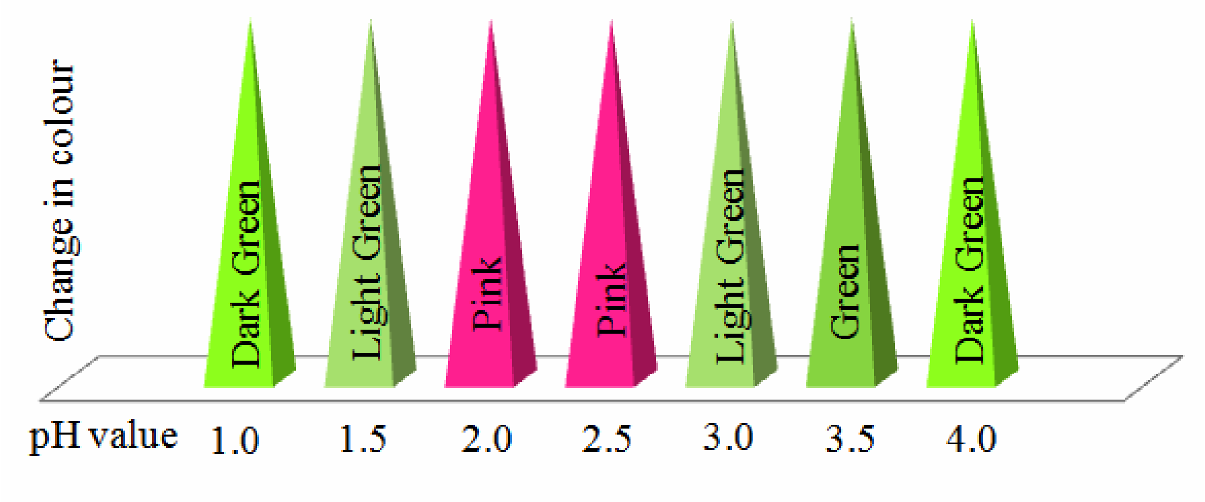

Fig. 6.5: Histogram representing the change in colour of solution with pH.

The colour of the mixture is also dependent upon the pH value. It was observed that the colour of the solution became darker by the addition of acids (H^+) or bases (OH^-). The colour of the original mixture is pink changing to light/dark green due to the addition of H^+ and OH^- as shown in Fig. 6.5. This pH-dependent property suggests that the change in concentration of H$^+$ and OH$^-$ causes the electronic transition changes of $\pi \rightarrow \pi^*$ and $n \rightarrow \pi^*$ in CQD by refiling or depleting their valence bond, thereby changing the fluorescence intensity.

6.3.4.2 Kinetic Study (Testing at Different Time Intervals)

The fluorescence intensity does not significantly increase, with an increase in the incubation time. The kinetic study was performed upto the incubation time of 120 seconds as shown in Fig. 6.4(c). So 120 seconds was selected as the optimum time for the instant interaction of 6-TG with Au@CQDs which remains stable afterward.

6.3.5 Fluorescence Turn-on Detection of 6-TG

The Au@CQDs exhibit fluorescence turn on behavior upon addition of 6-TG. The plot of enhanced fluorescence intensity (F/ F$_0$) against the concentration of 6-TG with the addition of 10 μL at each time is shown in Fig. 6.6 (a) indicating that even with the small addition (10 μL) of 6-TG notable change in the PL intensity was observed.

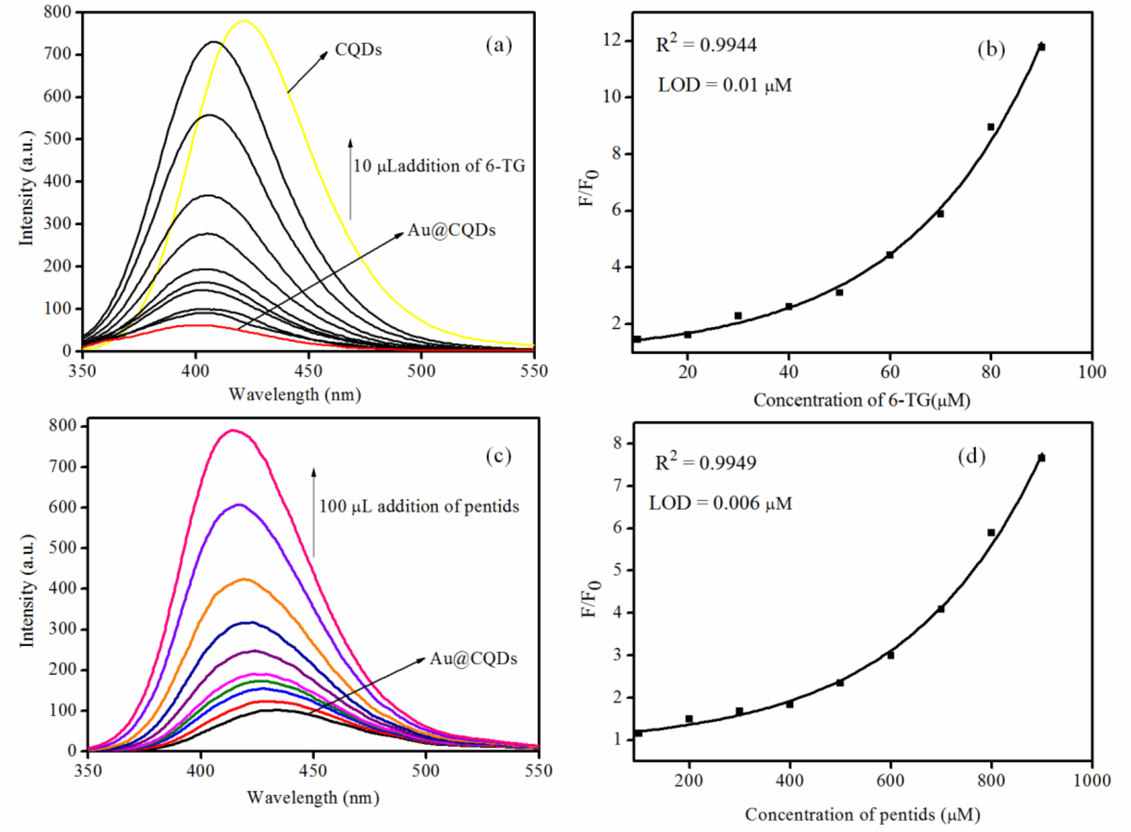

Fig. 6.6: (a) Emission spectrum of Au@CQDs after addition of different concentrations of (a) 6-TG (c) Pentids, linear relationship between the (F-F$_0$/ F$_0$) against the concentration of (b) 6-TG in the range 0-100 μM with the correlation coefficient of 0.9944 (c) Pentids in the range 100-1000 μM with the correlation coefficient of 0.9949.

Meanwhile, a linear relationship between the (F/F_0) against the concentration of 6-TG is obtained in the range of 0-100 μM with the correlation coefficient of 0.9944 (Fig. 6.6(b)). This fluorescence turn-on behaviour is due to the interaction of 6-TG with Au NPs via Au-S bond, leading to aggregation of NPs that was confirmed by HRTEM images as shown in Fig. 6.2(d). The limit of detection ($3\sigma/s$) for 6-TG was found to be 0.01μM, where σ represents the standard deviation of five blank measurements, and s is the slope of the calibration curve and comparatively this method is better compared with those previously reported techniques [29-31] and biosensors as shown below in Table 6.1 and 6.2.

Table 6.1: The performance of optical sensors assembles for 6-thioguanine

Biosensor	**Regression Coefficient**	**LOD**	**Reference**
Gold nanorod	0.997	0.015	[26]
Gold nanosphere	0.996	0.220	[26]
Silver nanoparticles	0.997	0.009	[27]
Multiwall carbon nanotubes	0.9835	0.008	[28]
CQD-AuNPs	0.990	-	[24]
CQD-AgNPs	0.995	0.01	[24]
CQD-AuNPs	0.994	0.01	Present Work

Table 6.2: The performance of optical sensors assembles for 6-thioguanine

Biosensor	**Regression Coefficient**	**LOD**	**Reference**
Gold nanorod	0.997	0.015	[26]
Gold nanosphere	0.996	0.220	[26]
Silver nanoparticles	0.997	0.009	[27]
Multiwall carbon nanotubes	0.9835	0.008	[28]
CQD-AuNPs	0.990	-	[24]
CQD-AgNPs	0.995	0.01	[24]
CQD-AuNPs	0.994	0.01	Present Work

6.3.6 Mechanism for Fluorescence Turn-on/off Detection of 6-TG by CQDs

As shown in Fig. 6.2(c) the fluorescence intensity of CQDs was quenched by 96% with the interaction of Au^{3+} forming Au@CQDs. The fluorescence lifetime of CQDs decreased from 3.9 ns to 3.6 ns due to the presence of Au^{3+} ascribed to the energy transfer process taking place in the CQD-AuNP systems, where CQD acts as the donor and AuNPs as the acceptors leading to the quenching of fluorescence. The quenching is dynamic in nature, as a decrease in the emission lifetime of the semiconductor colloids is observed when an electron acceptor or surface modifier is adsorbed on the semiconductor surface which is confirmed by Stern Volmer plot (Fig. 6.6(a)) [22]. Thus, it suggested that Au^{3+} was bound to the surface of CQDs. This whole prediction was also verified by the results of UV-Vis absorption spectra as the peak of CQDs diminishes at 370 nm that was attributed to change in their surface states as Au^{3+} gets bound to CQDs surface. The AuNPs were stabilized by carboxyl and hydroxyl groups present on the surface of CQDs which are well-known to bind weakly to the AuNPs surface. Upon accumulation of 6-TG, the Au-S bond could be formed because of a strong binding preference of thiol groups for metals. This leads to aggregation of AuNPs and release of CQDs from Au surface. The recovered fluorescence intensity only resulted by forming $[Au\text{- }(6\text{-TG})_n]^{3-}$ complexes in the presence of thiols. Moreover, as more number of Au aggregates are formed with the increasing amount of 6-TG, the number of fluorescence acceptors decreases which cause steric hindrance effect and Au no longer behave as good acceptor and the fluorescence intensity of CQDs is recovered.

6.3.7 Analytical Application

To promote the applicability of the present technique in biological industries the whole scenario was also performed for several biomolecules and amino acids as shown in Fig. 6.7. The results recommended that the Au@CQDs composite is suitable for thiol-containing biomolecules. As the amino acids which do not contain any free sulfhydryl groups, they are not capable of exchanging the CQDs from AuNPs surface. Encouraged by these positive results, we investigated the technique for enzymes which also shows the turn-on fluorescence because of the presence of free sulfhydryl groups present in the biomolecules.

To further symbolize the applicability of Au@CQDs as a biosensor for pharmaceutical utility, we investigated the results for pentids tablets. Pentids tablets contain Penicillin G as an active ingredient and are generally used for bacterial infections and sexually transmitted infections.

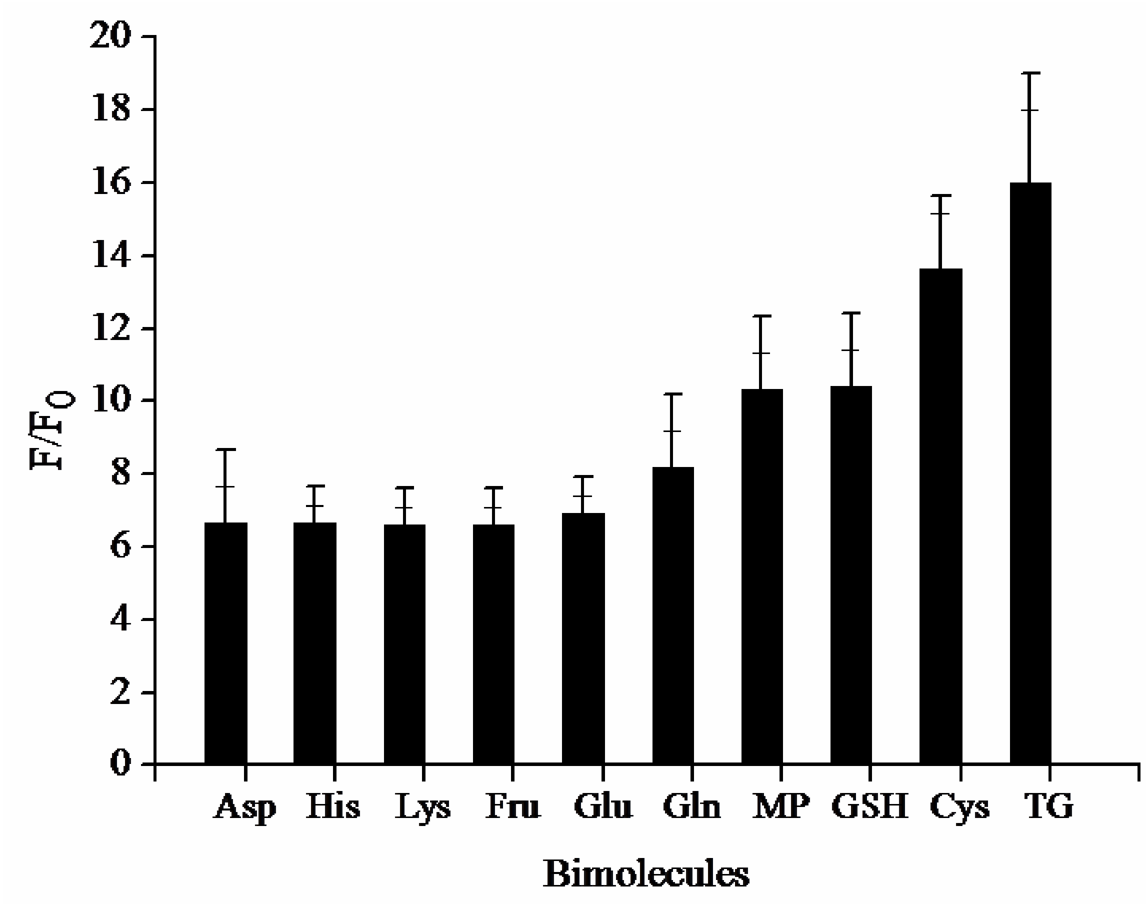

Fig. 6.7: Plot of relative intensities of Au@CQDs as a function of different biomolecules.

The plot of enhanced fluorescence intensity against the concentration of pentids with the addition of 100 μL at each time is as shown in Fig. 6.6(c). The turn-on fluorescence is linearly dependent upon the concentration of pentids with a correlation coefficient of 0.9949 and observed LOD is 0.006 μM (Fig. 6.6(c)). This suggests that the composite is highly beneficial to be used as a fluorometric sensor for thiol-containing biomolecules.

References

1. Myers JP, vom Saal FS, Akingbemi BT, Arizono K, Belcher S, Colborn T, Chahoud I, Crain DA, Farabollini F, Guillette Jr LJ, Hassold T. Why public health agencies cannot depend on good laboratory practices as a criterion for selecting data: the case of bisphenol A. Environmental Health Perspectives. 2009 Mar;117(3):309.

2. Misra V, Pandey SD. Hazardous waste, impact on health and environment for development of better waste management strategies in future in India. Environment international. 2005 Apr 1;31(3):417-31.

3. Villegas LG, Mashhadi N, Chen M, Mukherjee D, Taylor KE, Biswas N. A short review of techniques for phenol removal from wastewater. Current Pollution Reports. 2016 Sep 1;2(3):157-67.

4. Jones OA, Voulvoulis N, Lester JN. Potential ecological and human health risks associated with the presence of pharmaceutically active compounds in the aquatic environment. Critical reviews in toxicology. 2004 Jan 1;34(4):335-50.

5. Oturan MA, Aaron JJ. Advanced oxidation processes in water/wastewater treatment: principles and applications. A review. Critical Reviews in Environmental Science and Technology. 2014 Dec 2;44(23):2577-641.

6. Martinez-Huitle CA, Ferro S. Electrochemical oxidation of organic pollutants for the wastewater treatment: direct and indirect processes. Chemical Society Reviews. 2006;35(12):1324-40.

7. Oller I, Malato S, Sánchez-Pérez J. Combination of advanced oxidation processes and biological treatments for wastewater decontamination—a review. Science of the total environment. 2011 Sep 15;409(20):4141-66.

8. Dewil R, Mantzavinos D, Poulios I, Rodrigo MA. New perspectives for advanced oxidation processes. Journal of environmental management. 2017 Jun 15;195:93-9.

9. Reddy PV, Kim KH, Kavitha B, Kumar V, Raza N, Kalagara S. Photocatalytic degradation of bisphenol A in aqueous media: A review. Journal of environmental management. 2018 May 1;213:189-205.

10. Ribeiro AR, Nunes OC, Pereira MF, Silva AM. An overview on the advanced oxidation processes applied for the treatment of water pollutants defined in the recently launched Directive 2013/39/EU. Environment International. 2015 Feb 28;75:33-51.

11. Mehta A, Mishra A, Sharma M, Singh S, Basu S. Effect of silica/titania ratio on enhanced photooxidation of industrial hazardous materials by microwave treated mesoporous SBA-15/TiO_2 nanocomposites. Journal of Nanoparticle Research. 2016 Jul 1;18(7):209.

12. Mehta A, Sharma M, Kumar A, Basu S. Effect of Au content on the enhanced photocatalytic efficiency of mesoporous Au/TiO_2 nanocomposites in UV and sunlight. Gold Bulletin. 2017 Mar 1;50(1):33-41

13. Mehta A, Basu S. Controlled photocatalytic hydrolysis of nitriles to amides by mesoporous MnO_2 nanoparticles fabricated by mixed surfactant mediated approach. Journal of Photochemistry and Photobiology A: Chemistry. 2017 Jun 15;343:1-6.

14. Peng WC, Wang SB, Li XY. Shape-controlled synthesis of one-dimensional α-MnO_2 nanocrystals for organic detection and pollutant degradation. Separation and Purification Technology. 2016 May 11;163:15-22.

15. Wang Y, Indrawirawan S, Duan X, Sun H, Ang HM, Tadé MO, Wang S. New insights into heterogeneous generation and evolution processes of sulfate radicals for phenol degradation over one-dimensional α-MnO_2 nanostructures. Chemical Engineering Journal. 2015 Apr 15;266:12-20.

16. Zhang P, Zhan Y, Cai B, Hao C, Wang J, Liu C, Meng Z, Yin Z, Chen Q. Shape-controlled synthesis of Mn_3O_4 nanocrystals and their catalysis of the degradation of methylene blue. Nano Research. 2010 Apr 1;3(4):235-43.

17. Zhang W, Yang Z, Wang X, Zhang Y, Wen X, Yang S. Large-scale synthesis of β-MnO2 nanorods and their rapid and efficient catalytic oxidation of methylene blue dye. Catalysis Communications. 2006 Jun 1;7(6):408-12.

18. Dong Y, Yang H, He K, Song S, Zhang A. β-MnO_2 nanowires: a novel ozonation catalyst for water treatment. Applied Catalysis B: Environmental. 2009 Jan 12;85(3-4):155-61.

19. Mehta A, Pooja D, Thakur A, Basu S. Enhanced photocatalytic water splitting by gold carbon dot core shell nanocatalyst under visible/sunlight. New Journal of Chemistry. 2017;41(11):4573-81.

20. Cai QY, Li J, Ge J, Zhang L, Hu YL, Li ZH, Qu LB. A rapid fluorescence “switch-on” assay for glutathione detection by using carbon dots–MnO_2 nanocomposites. Biosensors and Bioelectronics. 2015 Oct 15;72:31-6

21. Zhang H, Zhao L, Geng F, Guo LH, Wan B, Yang Y. Carbon dots decorated graphitic carbon nitride as an efficient metal-free photocatalyst for phenol degradation. Applied Catalysis B: Environmental. 2016 Jan 1;180:656-62.

22. Benjamin O, Silcock P, Leus M, Everett DW. Multilayer emulsions as delivery systems for controlled release of volatile compounds using pH and salt triggers. Food Hydrocolloids. 2012 May 1;27(1):109-18.

23. Rather RA, Singh S, Pal B. A Cu+ 1/Cu0-TiO_2 mesoporous nanocomposite exhibits improved H_2 production from H_2O under direct solar irradiation. Journal of Catalysis. 2017 Feb 1;346:1-9.

24. Fufa TO, Yadav AT. Synthesis, characterization and photocatalytic activity of $MnO_2/Al_2O_3/Fe_2O_3$ nanocomposite for phenol degradation. Synthesis. 2014;6(10).

25. An G, Ma W, Sun Z, Liu Z, Han B, Miao S, Miao Z, Ding K. Preparation of titania/carbon nanotube composites using supercritical ethanol and their photocatalytic activity for phenol degradation under visible light irradiation. carbon. 2007 Aug 1;45(9):1795-801.

CHAPTER 7

Highly Effective CQD/TiO_2 Nanocomposite For Sensing of Toxic Metal Ions and Photodetoxification of Industrial Dyes with Kill Waste by Waste Concept

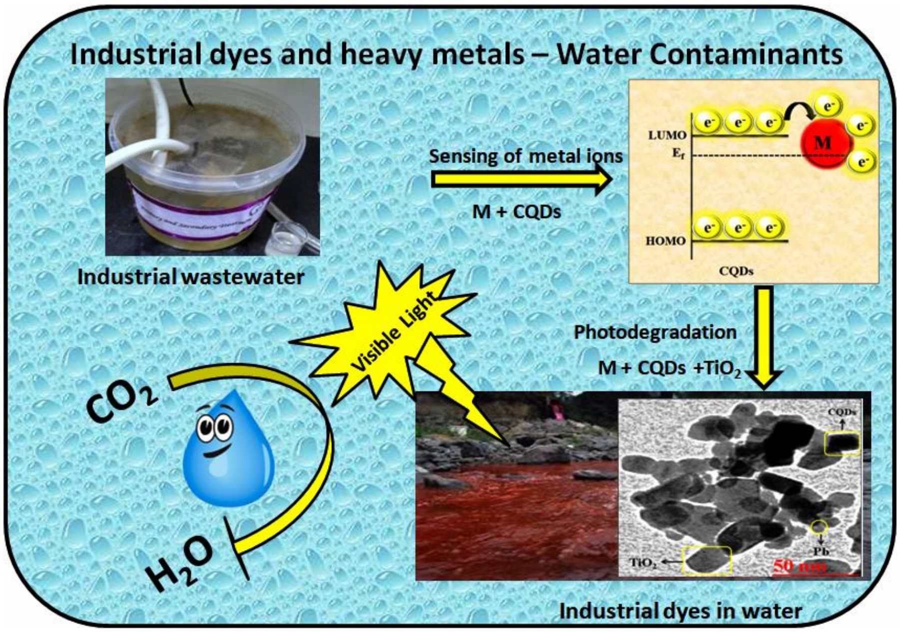

Highlights

- A novel “Kill waste by waste” approach was adapted for the waste water treatment.
- Detection of a toxic metal ion by CQDs and immersed with TiO_2 to make PCT composites.
- The PCT nanocomposites were utilized for the complete photodetoxification of dyes.
- The analytical practical also shows excellent activity for real water samples.

7.1 Introduction

The toxic effluent in the form of heavy metals and harmful dyes are two major concerns abating the quality of water. This is reasonably due to the ever-growing population, commercialization, ecological degradation and harmful domestic/industrial discharge. Amongst diverse heavy metal ions, mercury (Hg), lead (Pb) and cadmium (Cd) are forbidden in electronic equipment by the European Union's restriction on hazardous substances (RoHS) directive owing to their harmful nature [1-5]. Among these metal ions, Pb is the most abundant and toxic ion because of its use in pigments, batteries, and gasoline. Even tiny amounts of Pb causes reproductive, cardiovascular, neurological and developmental disorders particularly in women and children [6]. Currently, the most common techniques used for the detection of Pb ions are optical detections like colorimetric and fluorescence changes. The chief benefit of utilizing the fluorescence technique is its ease and lower limit of detection [7-10]. Now, the concern is to rationally design a material capable of sensing the Pb ions from toxic water leading to its removal.

Recently carbon quantum dots (CQDs) are emerging as one of the best nanomaterials for the numerous photocatalytic applications. This new class of zero-dimensional nanomaterials was accidentally obtained during purification of single-walled carbon nanotubes in 2004 [11-12]. Since then CQDs have attained a special status in the carbon-based material family. Their merits such as inexpensive, facile synthesis, excellent water solubility, low toxicity, stable fluorescence and biocompatibility. These properties craft them as next-generation luminescent nanomaterials superior to other traditionally used both luminescent inorganic quantum dots and fluorescent organic dyes [13-15]. Recently, Kumar *et al*. [16] synthesized CQDs by *Ocimum sanctum* for the selective sensing of Pb ions with a limit of detection 0.59 nM. He *et al*. [17] built a selective fluorescent Leadfluor-1sensor synthesized by organic processes for detecting Pb in living cells. Similarly, Dong *et al.* [18] used a new co-reactant electrochemiluminescence (ECL) system consisting of carbon quantum dots (CQDs) and sulfite SO_3^{2-} for this purpose. Though many more reports are available in the literature for better sensing of lead ions. Each of these reports has its limitations of cost/time effectiveness and non-utilizing of the Pb/CQDs solution after detection.

Industrial dyes like reactive brilliant red X-3BS (RBX), coralline red BS (CRB) and remazol black XP (CNB) etc. from textile and printing industry are the key sources of water contamination and harmful to aquatic life [19-22]. To remove these toxic dyes numerous materials and modifications have been used. But to “kill waste by waste” type technique is not reported yet. In this process (“kill waste by waste”) we utilize Pb-CQDs and impregnate light active support like titanium dioxide (TiO_2) on it for the detoxification of dyes. This strategy is a novel concept towards sustainable development. The reason to choose TiO_2 is due to its excellent record for photocatalytic dye degradation. The single drawback of TiO_2 as a photocatalyst is its band gap i.e. 3.2 eV which disables it to be active in the visible light region of the solar spectrum. This limitation can be overcome by the above-said approach.

In this respect, a novel “kill waste by waste” type methodology was adopted for the removal of both toxic Pb and industrial dyes. The synthesis of CQDs has been done by a facile one-step process using ascorbic acid as a precursor. The as-synthesized CQDs were utilized for the detection of heavy metal ions (Pb), selectively. The as-fabricated Pb-CQDs solution was immersed in TiO_2 by wet impregnation method without adding any structure directing agent. Hence as an outcome, the process is very facile, reproducible and cost-effective. The Pb-CQDs-TiO_2 (PCT) nanocomposite was successfully used for the complete photo-detoxification of industrial dyes like RBX, CBX etc. This was examined by optical spectroscopy and gas chromatography considering CO_2 and H_2O as a final photo mineralized product. The same procedure was also adopted for real sample analysis in order to test the results at an industrial scale.

7.2 Experimental procedure

7.2.1 Chemicals and Reagents

All the analytic grade chemicals were used as received: Ascorbic acid (99%, Loba Chemie Ltd.), Ethanol (99.9 %, Jiangsu Huaxi International China), Titanium dioxide (TiO_2-P25, 50% Evonik Industries), Lead nitrate ($Pb(NO_3)_2$, 98% Merck). Kollcoat-IR (MW = 45000) was gifted from BASF which was used as the stabilizing agent in the synthesis of CQDs. Deionized (DI) water (35 mho cm^{-1} at 25^oC) obtained from Millipore (Milli-Q) ultra-filtration system was used throughout the experiment.

7.2.2 Synthesis of CQDs and Pb-CQDs-TiO_2 nanocomposite

Carbon quantum dots were synthesized by the microwave-assisted facile and green method; we have reported earlier [11]. Briefly, 0.5 g of ascorbic acid and kollicoat (1:1w/w %) was dissolved in water under continuous stirring. After 20 minutes the sample (5 mL) was pipetted out into glass reaction vessel and heated in the microwave synthesizer (Multiwave

3000 microwave reaction system, Anton Paar). The reaction was carried out at a temperature of 130 °C for 30 minutes at 300 W powers. The yellow color of the mixture confirmed the formation of CQDs. The final composite of Pb-CQDs-TiO_2 was synthesized by wet impregnation method. A suspension of P25 (0.5 g) in water (20 mL) was stirred at room temperature and then1.0 mL of Pb-CQDs (1:1 v/v) solution was added dropwise. The stirring was continued for 8-10 hours at room temperature to make a homogenous solution. The samples were washed with water through centrifugation and dried in an oven at 80^0C for 8 h. The as-prepared solid photocatalyst was abbreviated as PCT.

7.2.3 Sensing/detection of heavy metal ions

The detection of toxic metal ions was performed in water by the fluorescence spectrophotometer. The metal ions with concentrations of 10 µM (Cu, Ni, Cd, Pb, and Hg) were mixed with 1 mL of CQDs and incubated for 10 minutes at room temperature. The photoluminescence (PL) signal was investigated by fluorescence spectrometer at an excitation wavelength of 320 nm. After the selective detection of Pb, the Pb-CQDs photocatalyst was kept for the purpose of photo-detoxification of harmful dyes.

7.2.4 Characterization and photocatalytic activity

Electronic excitations and emissions of CQDs and metal-CQDs were analyzed by using a UV-Vis spectrophotometer (Analytik Jena, Specord 205) and fluorescence spectrophotometer (PerkinElmer LS-55, USA) using an excitation wavelength ranging from 260-320 nm. X-ray diffraction pattern studies of the photocatalysts were studied by PANalytical Xpert Pro (Almelo, Netherlands) with Cu Kα at 1.54 A^o operating at 45 kV and the diffraction angle of $20\text{-}80^o$ (5^o/min rise). High-resolution transmission electron microscopy (HRTEM) was carried out on Technie G2 (FEI) S-Twin instrument operated at 200 kV. The FESEM and EDS were done by Hitachi SU 8180 field emission scanning electron microscope operating at 30 kV. To examine the oxidation state, X-ray photon spectroscopy (XPS) was recorded on commercial Omicron EA 125, source Al-kα radiation at 1486.6 eV. Particle size distribution and zeta potential were determined by dynamic light scattering method (DLS, Zetasizer, Malvern). The band gap was measured by UV-Vis diffuse reflectance spectroscopy with Hitachi 3900H spectrophotometer using $BaSO_4$ as a reflectance standard. Surface area and porosity were measured by BET (BEL mini-II, Micro Trac Corp. Pvt. Ltd, Tokyo, Japan) based N_2 adsorption-desorption method at cryogenic temperature after pre-treating the sample at 100^oC for 3 h at N_2 atmosphere.

The photocatalytic activity was carried out in a test tube containing 5 mL dye solution (100 mg/L) and 10 mg (2 mg/mL) of photocatalyst under visible light source with intermittent stirring. The reaction mixture containing dye solution and photocatalyst was stirred in dark for 60 minutes before illumination. The kinetics and concentration change of dye samples were recorded after filtration with cellulose filter (0.22 µm) at different time intervals having the absorption maximum at 520 nm under UV-Vis spectrophotometer. The total mineralization of the dye samples was quantified by observing the amount of CO_2 evolved through gas chromatography (GC Nucon 13A porapak-Q column with TCD detector). The quantification of CO_2 was done against the 200 ppm standard with a retention time of 0.57 min. The temperature of the detector, injector and oven was set at room temperature and the injection was done manually by a gas tight syringe (Hamilton, 5 mL). Moreover, the reaction intermediates were identified by GC-MS (Shimadzu QP2010 plus, RTX-5 sil MS column) by injecting 1µL of the extracted sample with Helium gas (1ml/min) as a carrier. The oven was programmed from 60^oC (5 min hold) to $240^oC@6^o$ C, while transfer line and injector were kept isothermally at 250^oC and 275^oC respectively.

7.2.5 Detection of hydroxyl radicals ($^{\bullet}OH$) generated during photoexcitation

The generation of $^{\bullet}OH$ radicals on the surface of the photocatalysts was determined from photo-luminescence (PL) technique using coumarin as a probe molecule. Coumarin reacts with $^{\bullet}OH$ radicals to form highly fluorescent 7-hydroxycoumarin. The experimental procedure was similar to that of the photocatalytic process and was carried out in the test tube containing 10 mg of the photocatalyst and 5 mL of coumarin aqueous solution (10^{-3} M). The PL spectra of the photocatalysts were measured on a fluorescence spectrophotometer at an excitation wavelength of 320 nm.

7.3. Results and Discussion

7.3.1 Detection of toxic heavy metals by CQDs and its selectivity for Pb ions

The PL responses of CQDs towards different metal ions including Hg^{+2}, Cd^{+2}, Ni^{+2}, Cu^{+2}, and Pb^{+2} have been analyzed. The above metal ions of concentration, 10 µM were added to the solution of CQDs (2 mL) and their PL spectrum has been recorded. The histogram is plotted taking F/F_0 against the equal concentration of different metal ions as shown in Fig. 7.1. The Pb^{2+} ions cause the drastic change in the fluorescence intensity compared to other metal ions enlightening its strong interaction with CQDs. High selectivity and specificity of Pb^{2+} ions towards CQDs are due to the very high binding affinity between the vacant d-orbital of Pb^{2+} and hydroxyl groups present on CQDs. The hydroxyl group present on the CQDs donates the electron to the vacant orbital of Pb^{2+} via non radiative type electron-transfer mechanism which is facile compared to other metal ions.

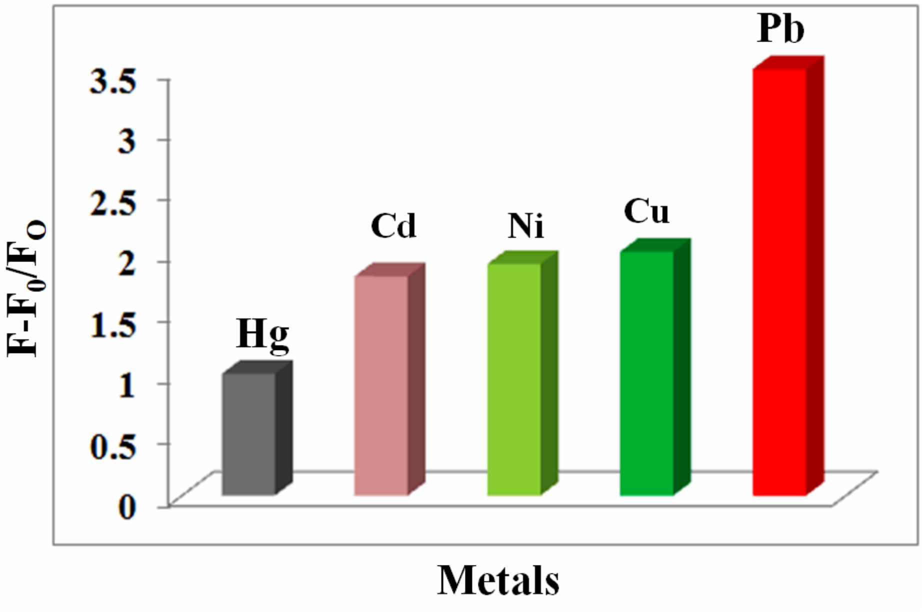

Fig. 7.1: Plot of relative fluorescence intensities of CQDs as a function of different metal ions.

The sensitivity of CQDs towards Pb^{2+} was evaluated under optimized conditions. As shown in Fig. 7.2(a), the PL intensity of CQDs gradually quenched with the addition of Pb^{2+} in the range of 0-100 µM. The plot of enhanced fluorescence intensity (F/F_0) against the concentration of Pb^{2+} with the addition of 10 µL each time is shown in Fig. 7.2(b) which discloses that even with the small addition (10 µL) of Pb^{2+}, the notable change in the PL intensity is observed. Meanwhile, a linear relationship between the ($F- F_0/F_0$) against the concentration of Pb^{2+} was obtained with the limit of detection and correlation coefficient of 0.070 µM and 0.9944 respectively.

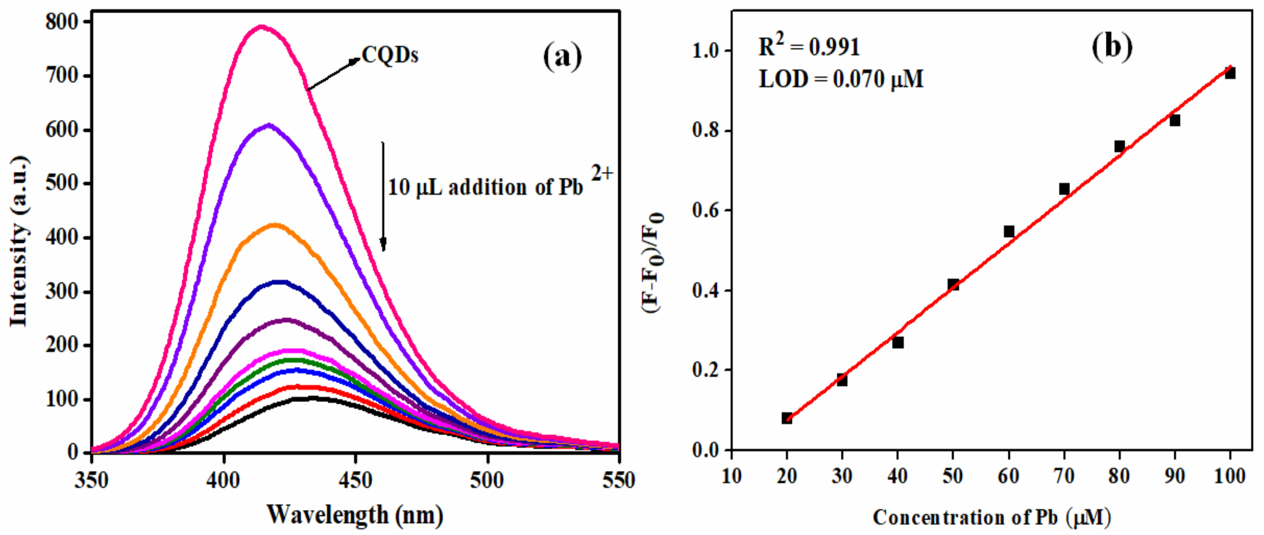

Fig. 7.2: (a) Emission spectrum of CQDs after addition of different concentrations of Pb ions and **(b)** linear relationship between the F-F_0/ F_0 against the concentration of Pb.

7.3.2 Structural and morphological characteristics of PCT photocatalyst

Additionally, the presence of Pb and CQDs were confirmed by the HR-TEM and elemental distribution analysis. Fig. 7.3(a) displays the micrographs of as-synthesized CQDs with a spherical morphology possessing an average diameter of ~7 nm, which is calculated through the statistical analysis for ~50 nanoparticles by image-j software. Two separate lattice fringes (d spacing) measured to be 0.35 nm and 0.14 nm were observed for TiO_2 (101) plane and PbO respectively, further confirmed by the selected area electron diffraction pattern (SAED) that is in consonance with the XRD and TEM results. Moreover, the dot elemental mapping (Fig. 7.4) of the final composite displays that all the elements are spatially distributed.

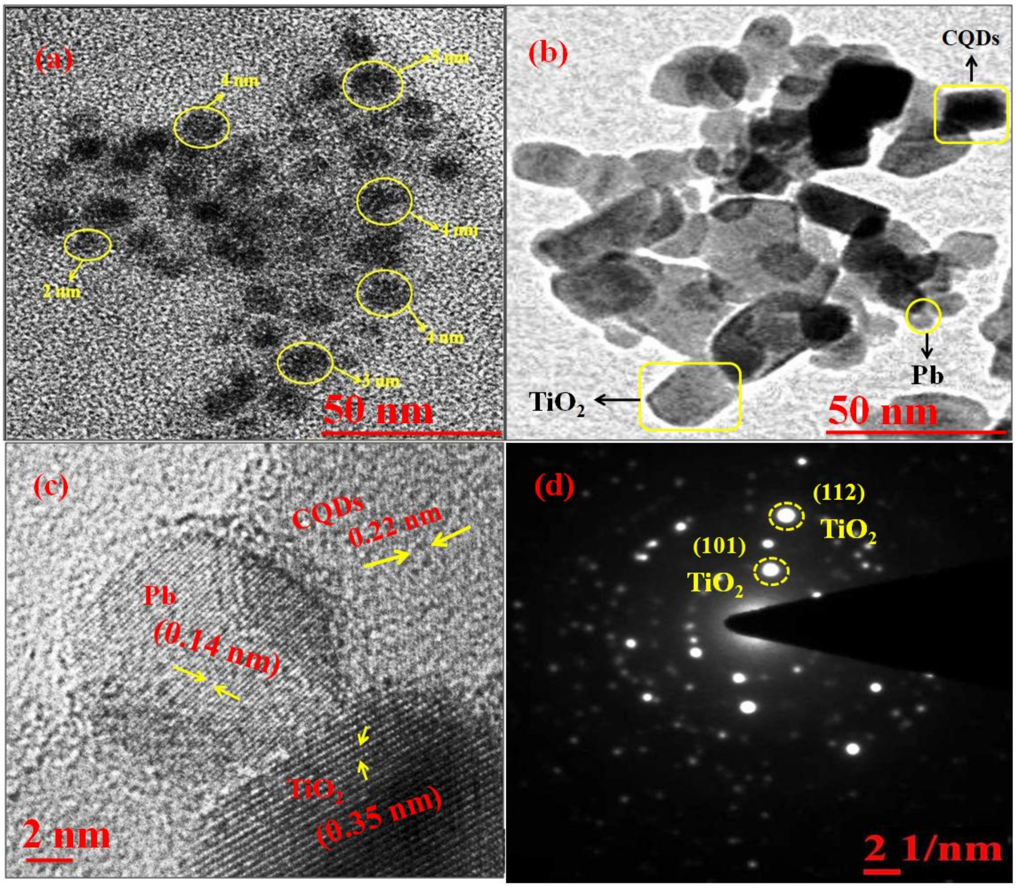

Fig. 7.3: (a) HRTEM micrographs of (a) pure CQDs, (b) PCT, (c) lattice fringes and (d) SAED pattern of PCT.

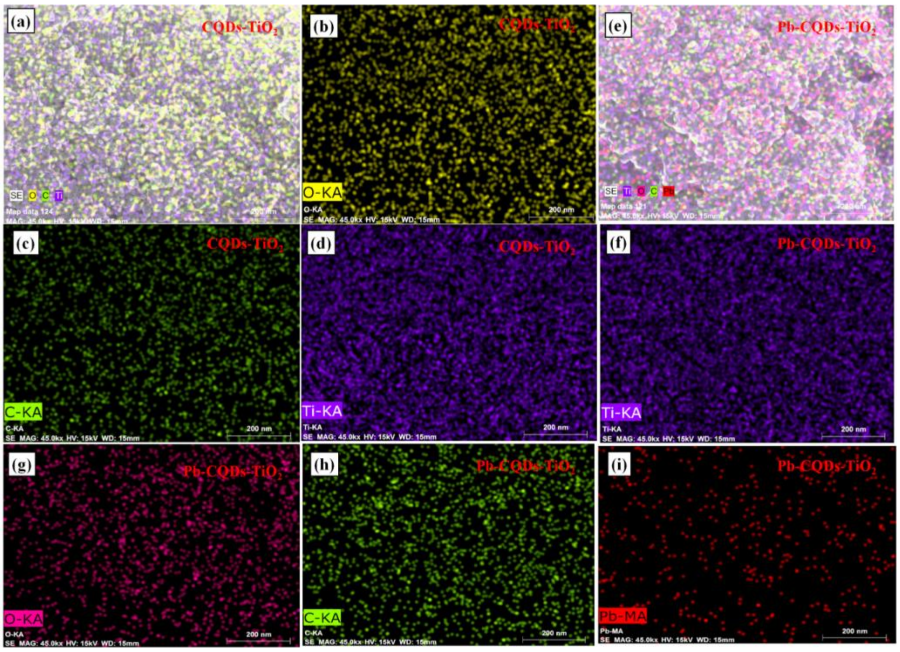

Fig. 7.4: Elemental mapping for (a) CQDs-TiO$_2$ (b) O-KA (c) C- KA (d) Ti-KA and (e) Pb-CQDs-TiO$_2$ (f)Ti-KA (g)O-KA (h) C- KA (i) Pb-MA

The BET (Brunner-Emmet-Teller) based on N_2 adsorption and desorption curves of the photocatalysts shows that all the adsorption-desorption isotherms are typical type-IV due to the little porous nature of the nanocomposites imparted by the presence of carbon. The surface area of TiO_2 (P25) alone was recorded to be 55 m^2/g which decreases after the inclusion of CQDs (23.5 m^2/g) due to the blockage of certain pore sites. The energy gap (E_g) calculated for TiO_2 by the optical absorption spectroscopy was 3.15 eV which makes it active in UV region only, the E_g got decreased to 2.8 and 3.0 eV for PCT and CQDs-TiO_2 respectively due to the effective charge transfer between these separate interfaces, which makes this composite active in the vast visible light spectrum.

7.3.3 X-Ray photoelectron spectroscopy (XPS) characteristics

As shown in Fig. 7.5(a, b) XPS analysis of CQDs before sensing of Pb ions depicted the respective peaks of different spin states of C 1s and O 1s. The high-resolution C 1s spectra have been deconvoluted into two peaks at 283.4 and 285.2 eV corresponding to (sp^2) C-C and C-O-C interaction. Similarly, the O1s spectrum is also fitted in two deconvoluted peaks with binding energy values of 532.7 and 533.8 eV corresponding to C=O and Ti-O-Ti bond respectively. After the sensing of toxic metal ions (Pb) by CQDs and its impregnation of TiO_2 support, a shift was observed in the binding energies of C 1s (285.2 to 284.5 eV) and O 1s (532.7 to 528.8 and 530.2 to 533.8 eV respectively). This shifting of the peak was probably due to the interaction of CQDs with Pb^{2+} and TiO_2 as electron pair of CQDs transfers to vacant d-orbital of Pb which is in compliance with PL results. In Pb spectrum, the oxidation state of Pb changes from +2 to +1 (PbO) due to interaction with CQDs at the binding energy of 138.0 and 141.7 eV. In the case of Ti 2p, two binding energy values are recorded at 457.6 eV and 464.7 eV assigned to two typical states of Ti^{+4} ($2p_{3/2}$ and $2p_{1/2}$ respectively).

7.3.4 Photocatalytic activity

The photocatalytic activity of the photocatalyst was monitored by detoxifying the most harmful industrial dyes like RBX, CRB, and CNB. Control experiments were performed revealing that the above-mentioned dyes do not degrade in dark or by photolysis. Therefore the collective effect of both light and photocatalyst were necessary for the photocatalytic oxidative degradation of dyes.

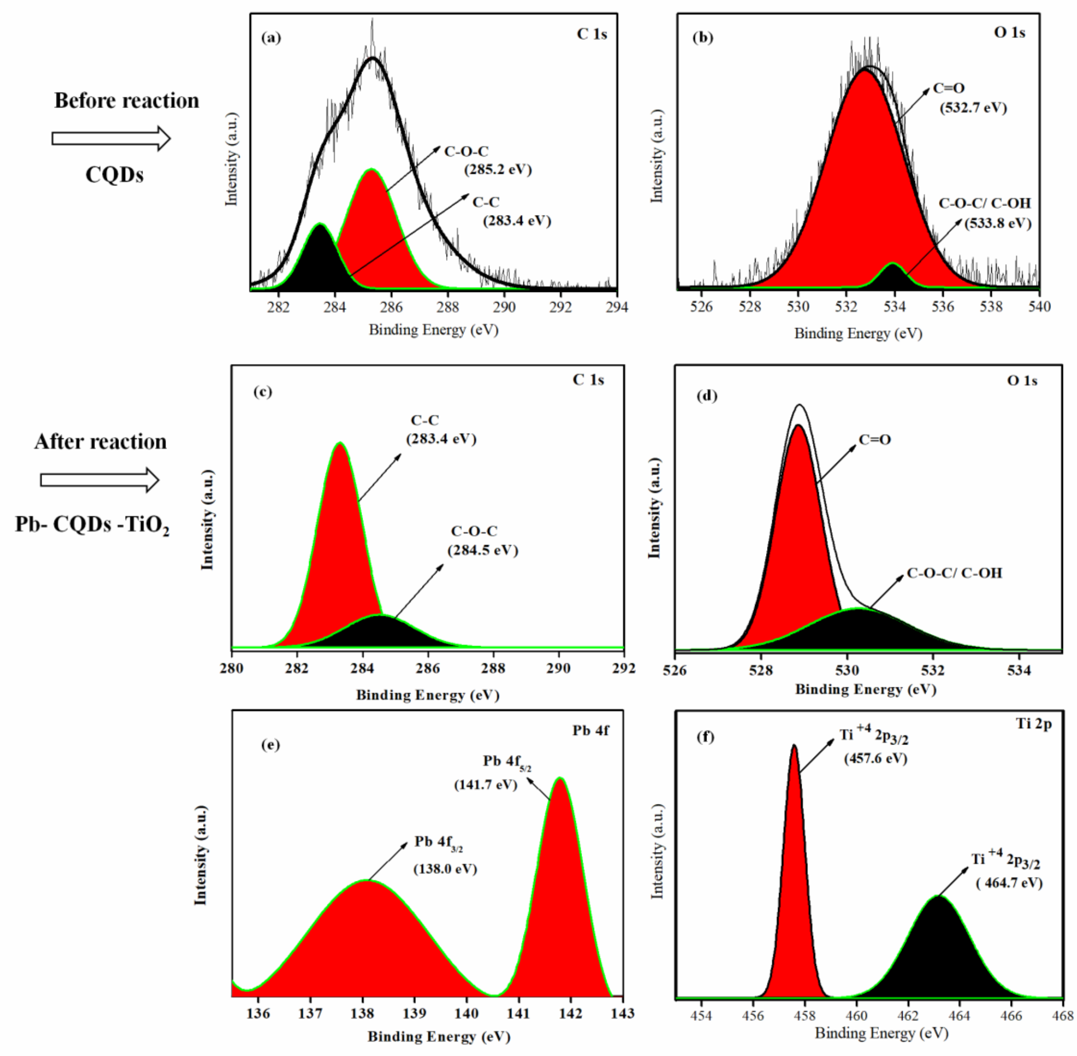

Fig. 7.5: XPS survey for (a-b) C 1s and O 1s spectrum of pure CQDs, (c-f) C 1s, O 1s, Pb 4f and Ti 2p of PCT (Pb-CQDs-TiO_2).

The PCT composite prepared in the present work may combine the adsorptive capacity of TiO_2, light absorption of Pb-CQDs and the photocatalytic ability of the PCT composite to degrade dye in aqueous solution. The degradation of dyes was monitored prior to the decrease in the intensity of absorption peak corresponding to 550 nm in the UV-Vis spectra. The photocatalytic activity of PCT was higher as compared to CQDs-TiO_2 and bare TiO_2 which is due to the formation of high oxidative radicals. The % degradation efficiency of RBX, CBX, and CRB dye was 100%, 99%, and 85% respectively by PCT. Moreover, the catalyst was easily separated from the reaction mixture as there was no permanent adsorption of reactants on the catalyst, so regeneration of catalyst was done after every reaction, with centrifugation and further washing with ethanol. The complete mineralization of RBX dye into CO_2 was analyzed through GC-analysis as shown in Fig. 7.6. The photocatalyst PCT evolve the highest amount of CO_2 compared to other photocatalysts at same reaction condition.

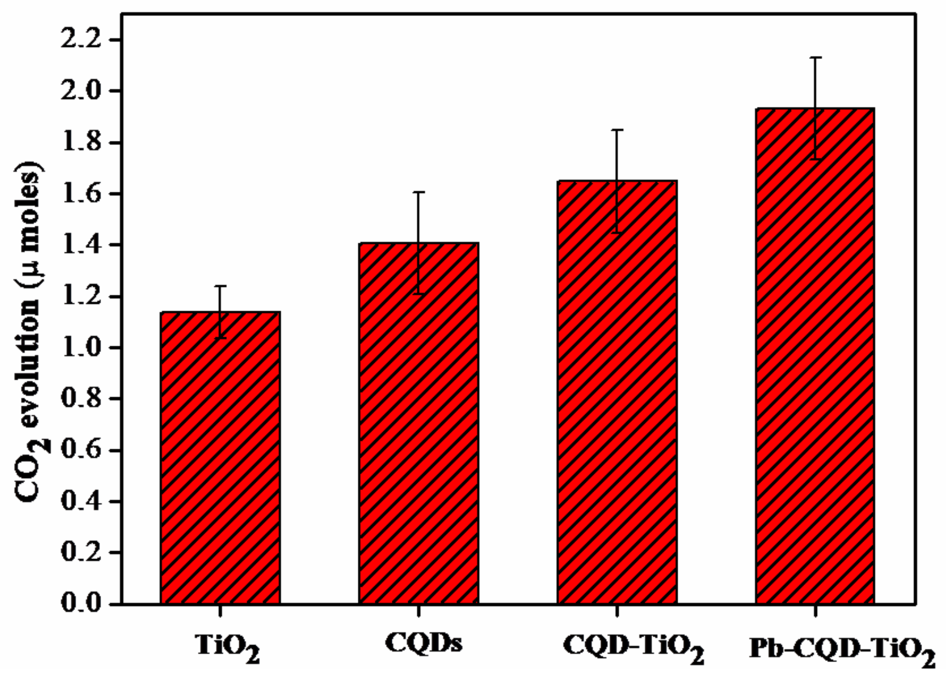

Fig. 7.6: CO_2 evolution for photocatalytic degradation of RBX dye with the different catalyst.

The higher photocatalytic activity of PCT over CQDs-TiO_2, bare TiO_2, and bare CQDs was mainly due to two reasons one is the formation of high oxidative radicals and other is perfect band alignment after the formation of the composite. Upon irradiation under visible light, electron excitation takes place in CQDs from HOMO to LUMO which further gets transferred to CB of TiO_2. Upon doping with lead cations, the formation of acceptor level above the HOMO of CQDs takes place which leads to a decrease in the band gap of the composite. Due to the creation of the acceptor level in CQDs, the number of holes increases which creates active sites for the formation of high oxidative radicals such as hydroxyl radicals ($OH^{\cdot}$). For comparison and understanding the mechanism of photocatalytic activity, the $OH^{\cdot}$ radicals were detected on the surface of visible illuminated photocatalysts by PL analysis using coumarin as reference molecule. The photocatalyst (PCT) shows maximum emission intensity and also lower E_g (2.8eV) compare to other photocatalysts which are clearly the reason for the highest increment in its photocatalytic activity.

The color of RBX dye fades away with time which may be ascribed due to the destruction of the chromophore of the dye molecule. Based on GC-MS analysis one plausible pathway for photodegradation of RBX is proposed as shown in Fig. 7.7.

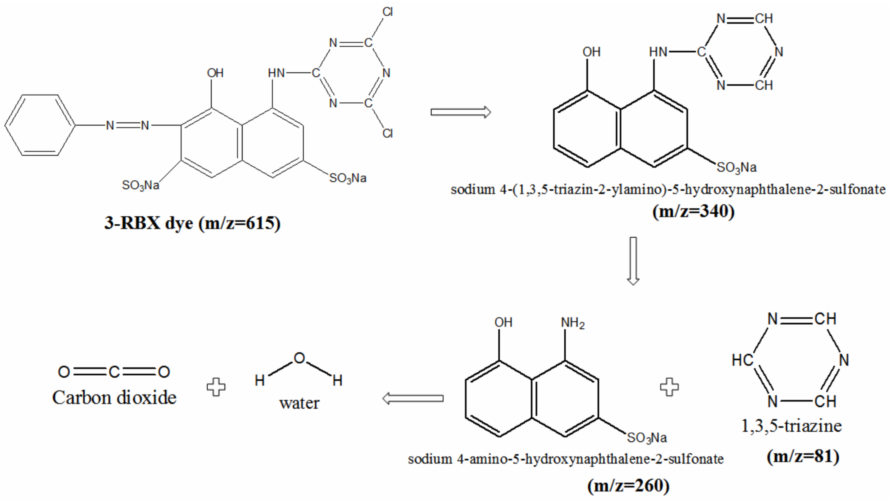

Fig. 7.7: Plausible mechanism for the photodegradation of RBX dye under visible light irradiation.

The route suggests that RBX with m/z =615 breaks into the molecule with m/z = 340 because of the low bond energy of –N–CH_3 bond (78 kcal/mol). Further by the cleavage of N–C bond, this route suggests the formation of intermediates with m/z = 260 and 81 and finally decomposes to CO_2 and H_2O. One molecule of RBX produces 19 molecules of CO_2 after complete degradation of dye. Quantitatively 0.05 μmol of RBX is supposed to produce 1.8 μmol of CO_2 by the composite. Thus, the present work presents the complete detoxification of RBX (100%) by Pb-CQDs-TiO_2 under visible light irradiation.

7.3.5 Real sample analysis

The main motive of above study is the selective removal of both lead ions and dyes from water. In consideration of above, real contaminated water samples were taken from different localities points in Patiala, India. Before analysis, the collected water samples were filtered through 0.22 μm membrane to remove suspended particles. Then the amount of Pb^{2+} in the collected water samples was analyzed by atomic absorption spectroscopy (AAS). The amount of Pb^{2+} in all the real samples was >0.070 μM (LOD for Pb^{2+} in synthetic solution by CQDs) so the samples were proceeded for sensing without spiking. The same sensing procedure was followed up for all the collected samples and immersed with TiO_2 to make PCT composites by real samples. Finally, the PCT composites synthesized by real water samples were again utilized for the photodegradation of RBX dye which shows good results (Table 1).

Again the real water samples were collected from paper and pulp industry Patiala, as this sample would be expected to contain a large amount of organic pollutant especially dyes. The sample was purified and spiked with the standard solution of dye (RBX, 100 mg/L) and photodegradation was checked using PCT composite. The composite regardless showed excellent efficiency (99%) for real water samples also. The brighter side of PCT composite is that it is easily recycled with no marks remaining in the samples. However, the application of Pb ions and degradation of dyes in wastewater samples has not been explored to this extent by CQDs till now.

Table 7.1: Determination of Pb ions in different waste water samples.

Samples	Amount of Pb determined by AAS (ppm)	F/F_0 of Pb-CQDs	% Degradation of RBX by PCT
Laboratory drain water (Thapar University area, Patiala, India)	0.1	0.856	88%
Local industrial drain water, Patiala	0.5	0.968	92%
Local battery industrial drain water, Patiala	0.6	0.988	95%
Standard solution	3.3	0.991	99%

References

1. Directive R. Directive 2002/95/EC of the European Parliament and of the Council of 27 January 2003 on the restriction of the use of certain hazardous substances in electrical and electronic equipment. Official Journal of the European Union. 2003 Feb;13:L37.

2. World Health Organization. Guidelines for drinking-water quality: recommendations. World Health Organization; 2004.

3. de Vries W, Römkens PF, Schütze G. Critical soil concentrations of cadmium, lead, and mercury in view of health effects on humans and animals. InReviews of Environmental Contamination and Toxicology 2007 (pp. 91-130). Springer New York.

4. Claudio ES, Goldwin HA, Magyar JS. Fundamental coordination chemistry, environmental chemistry, and biochemistry of lead (II). Progress in inorganic chemistry. 2003 Apr 4;51:1-44.

5. Guo Y, Zhang L, Cao F, Leng Y. Thermal treatment of hair for the synthesis of sustainable carbon quantum dots and the applications for sensing Hg^{2+}. Scientific reports. 2016 Oct 20;6:35795.

6. Carocci A, Catalano A, Lauria G, Sinicropi MS, Genchi G. Lead toxicity, antioxidant defense and environment. In Reviews of Environmental Contamination and Toxicology Volume 238 2016 (pp. 45-67). Springer, Cham.

7. Tarley CR, Andrade FN, De Oliveira FM, Corazza MZ, De Azevedo LF, Segatelli MG. Synthesis and application of imprinted polyvinylimidazole-silica hybrid copolymer for Pb^{2+} determination by flow-injection thermospray flame furnace atomic absorption spectrometry. Analytica chimica acta. 2011 Oct 10;703(2):145-51.

8. Pereira FM, Brum DM, Lepri FG, Cassella RJ. Extraction induced by emulsion breaking as a tool for Ca and Mg determination in biodiesel by fast sequential flame atomic absorption spectrometry (FS-FAAS) using Co as internal standard. Microchemical Journal. 2014 Nov 1;117:172-7.

9. Jiang Y, Wang Y, Meng F, Wang B, Cheng Y, Zhu C. N-doped carbon dots synthesized by rapid microwave irradiation as highly fluorescent probes for Pb^{2+} detection. New Journal of Chemistry. 2015;39(5):3357-60.

10. Mehta A, Pooja D, Thakur A, Basu S. Enhanced photocatalytic water splitting by gold carbon dot core shell nanocatalyst under visible/sunlight. New Journal of Chemistry. 2017;41(11):4573-81.

11. Cao L, Wang X, Meziani MJ, Lu F, Wang H, Luo PG, Lin Y, Harruff BA, Veca LM, Murray D, Xie SY. Carbon dots for multiphoton bioimaging. Journal of the American Chemical Society. 2007 Sep 19;129(37):11318-9.

12. Zhang H, Zhao L, Geng F, Guo LH, Wan B, Yang Y. Carbon dots decorated graphitic carbon nitride as an efficient metal-free photocatalyst for phenol degradation. Applied Catalysis B: Environmental. 2016 Jan 1;180:656-62.

13. Choi H, Ko SJ, Choi Y, Joo P, Kim T, Lee BR, Jung JW, Choi HJ, Cha M, Jeong JR, Hwang IW. Versatile surface plasmon resonance of carbon-dot-supported silver nanoparticles in polymer optoelectronic devices. Nature Photonics. 2013 Sep;7(9):732.

14. Li J, Gao X, Liu B, Feng Q, Li XB, Huang MY, Liu Z, Zhang J, Tung CH, Wu LZ. Graphdiyne: A metal-free material as hole transfer layer to fabricate quantum dot-sensitized photocathodes for hydrogen production. Journal of the American Chemical Society. 2016 Mar 18;138(12):3954-7.

15. Kumari A, Kumar A, Sahu SK, Kumar S. Synthesis of green fluorescent carbon quantum dots using waste polyolefins residue for Cu2+ ion sensing and live cell imaging. Sensors and Actuators B: Chemical. 2018 Jan 1;254:197-205.

16. He Q, Miller EW, Wong AP, Chang CJ. A selective fluorescent sensor for detecting lead in living cells. Journal of the American Chemical Society. 2006 Jul 26;128(29):9316-7.

17. Dong Y, Chen C, Lin J, Zhou N, Chi Y, Chen G. Electrochemiluminescence emission from carbon quantum dot-sulfite coreactant system. Carbon. 2013 May 1;56:12-7.

18. Mehta A, Mishra A, Sharma M, Singh S, Basu S. Effect of silica/titania ratio on enhanced photooxidation of industrial hazardous materials by microwave treated mesoporous SBA-15/TiO2 nanocomposites. Journal of Nanoparticle Research. 2016 Jul 1;18(7):209.

19. Mehta A, Sharma M, Kumar A, Basu S. Effect of Au content on the enhanced photocatalytic efficiency of mesoporous Au/TiO_2 nanocomposites in UV and sunlight. Gold Bulletin. 2017 Mar 1;50(1):33-41.

20. Tanaka K, Padermpole K, Hisanaga T. Photocatalytic degradation of commercial azo dyes. Water research. 2000 Jan 1;34(1):327-33.

21. Forgacs E, Cserhati T, Oros G. Removal of synthetic dyes from wastewaters: a review. Environment international. 2004 Sep 1;30(7):953-71.

22. Xia F, Ou E, Wang L, Wang J. Photocatalytic degradation of dyes over cobalt doped mesoporous SBA-15 under sunlight. Dyes and Pigments. 2008 Jan 1;76(1):76-81.

Fluorescent Carbon Dots decorated MnO_2 Nanorods for Complete Photo mineralization of Phenol

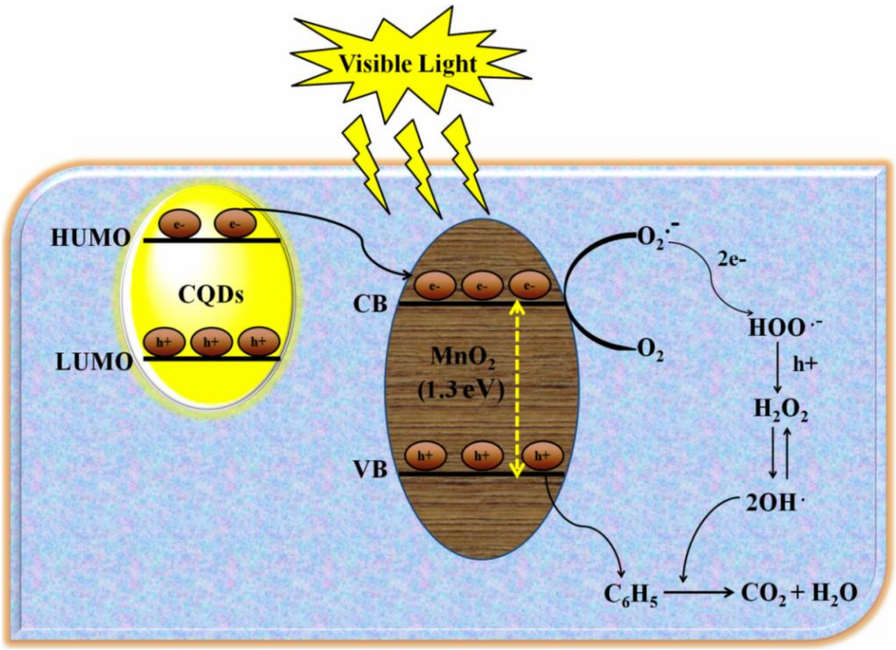

Highlights

- Synthesis of MnO_2@CQDs via novel in-situ approach by directly coating CQDs onto Mn nanorods.
- The composite regardless shows excellent photocatalytic activity towards phenol degradation.
- At optimum operational parameters, phenol degradation efficiency was found 90 % with a rate constant of 0.029 min^{-1}.
- The mechanism for higher activity of composite was detected by a scavenger and cyclic voltammetry study.

8.1 Introduction

The Environmental protection agency (EPA) identifies phenol as the most serious hazardous organic waste [1-2]. Phenolic compounds are effluents excreted from various chemical industries and this discharge without treatment leads to serious health risks to humans, animals, and aquatic systems [3-4]. The international agencies have set the strict limit for the discharge of phenol considering the sustainability and fragility of the environment. The excess exposure of phenol to humans can cause irritation in the skin, eyes, and mucous membranes. Many techniques have been developed for the phenol contaminated wastewater treatment. During the last few decades advanced oxidation processes (AOPs) have been identified as a feasible strategy to degrade a wide range of organic pollutants in aqueous media [5-10]. Most of AOPs are based upon the generation of some oxidative free radical species ($^{\cdot}OH$) to oxidize the pollutants effectively and rapidly [11-12].

Manganese dioxide (MnO_2) is copious in soils and also exists in many forms such as Mn_3O_4, Mn_2O_3, MnO_2, and MnO [13]. Due to variation in the oxidation states, MnO_2 have tremendous oxygen mobility in the oxide lattices and therefore induce better redox reactions. There are several reports in the literature on the fabrication of MnO_2 with different shapes for catalytic processes [14-16]. Zhang *et al.* [17] reported the synthesis of MnO_2 nanorods and their use as catalysts in the oxidation of methylene blue dye. Dong *et al.* [18] evaluated the catalytic properties of β-MnO_2 nanowires for the degradation of phenol and revealed good separability and remarkable catalysis for the degradation of phenol on MnO_2 nanowires. As a sustainable material, MnO_2 represents a striking visible light photocatalyst because of its suitable band gap (2.5 eV) for sunlight absorption. Though, MnO_2 possesses a quite low electrical conductivity which results in difficult charge transfer process and hence decreases the photocatalytic activity hopeful approach to increase the photocatalytic performance of MnO_2 is to form surface junctions to promote charge separation. Carbon quantum dots (CQDs) are the perfect sensitizers, predominantly composed of graphitic carbon (sp^2 carbon) with a size below 10 nm [19]. The quantum effect provides CQDs the broad optical adsorption which enables them to use as light absorbers and couple with other semiconductors like MnO_2 [20]. Also, CQDs act as electron transporters to direct the flow of photo generative carriers; hence combination is expected to deliver excellent photocatalytic activity [21].

Considering the above mention merits, here we report the synthesis of MnO_2@CQDs via novel in-situ approach by direct coating of CQDs on MnO_2 nanorods during the synthesis of MnO_2. The CQDs decorated MnO_2 composite regardless shows excellent photocatalytic activity towards phenol degradation under visible light irradiation. Moreover, the MnO_2@CQDs composite exhibits better efficiency than solely CQDs and MnO_2 nanorods. The present study delivers novel metal free composite for the removal of hazardous effluents from wastewater.

8.2 Experimental

8.2.1 Chemicals and reagents

All the analytic grade chemicals were used as received, manganese (II) nitrate tetrahydrate ($MnNO_3.H_2O$, 97.0% Sigma Aldrich), potassium permanganate ($KMnO_4$ 99%, Sigma Aldrich), ascorbic acid (99 %, Loba Chemie Ltd). Kollicoat-IR (MW 45 000Da) was gifted from BASF which was used as a stabilizing agent in the synthesis of CQDs. Deionized (DI) water obtained from Millipore (Milli-Q), an ultrafiltration system with 35 mhos cm^{-1} conductivity at 25^oC.

8.2.2 Preparation of CQDs and MnO_2@CQDs nanocomposite

Water-soluble CQDs were synthesized by adopting previously reported procedure from the same authors [19]. Ascorbic acid and kollicoat (1:1, w/w %) were dissolved and put under continuous stirring. After 30 minutes, the sample (10 mL) was transferred into glass reaction vessel subjected to microwave heating at 130 °C for 30 minutes at 300 W power with Multiwave-3000 microwave reaction systems (Anton Paar).

The MnO_2@CQDs nanorods were synthesized by a single facile hydrothermal method. A 0.2 g of $MnNO_3.H_2O$, 0.5 g $KMnO_4$ and 0.5 mL CQDs were placed in distilled water at room temperature to form a mixed solution. The solution was then transferred into a Teflon-lined stainless steel autoclave, sealed and maintained at 140 °C for 12 h. After the completion of the reaction, the resulting brownish-black solid product was filtered, washed with distilled water to remove the ions remaining in the final products, and finally dried at 100 °C in air.

8.2.3 Characterization and photocatalytic activity

The X-ray diffraction of photocatalyst was studied on PANalytical Xpert Pro (Almelo, Netherlands) with CuKα at 1.54 A^o operating at 45 kV and the diffraction angle of $20\text{-}80^o$

(5^o/min rise). High-resolution transmission electron microscopy (HRTEM) was carried out on Technie G2 (FEI) S-Twin instrument operated at 200 kV transmissions. The optical properties were studied by Analytic Jena, Specord 205 (Germany) UV-visible spectrometer. X-ray photon spectroscopy (XPS) was recorded on commercial Omicron EA 125, source Al-kα radiation at 1486.6 eV. Surface area and porosity were measured by BET, BEL mini-II, Micro Trac Corp. Pvt. Ltd, Tokyo, Japan) supported by the N_2 adsorption-desorption method at cryogenic temperature. The cyclic voltammetry (CV) characteristics were recorded on KEITHLEY (4200-SCS) by ZYVEX S100 nanomanipulator.

The photocatalytic activity was carried out in glass pyrex tube (10 mL), containing the reaction mixture of phenol (100ppm) and 5mg of photocatalyst under visible light (CFL60 W) setup with intermittent stirring. The kinetics and concentration change of phenol samples were recorded after filtration with cellulose filter (0.22 μm) at diverse time intervals by UV-Vis spectrophotometer. The quantification of CO_2 evolved during the reaction was done by gas chromatography (GC, Nucon Ltd, India) with thermal conductivity detector (TCD) and molecular sieve column (5X A, 1m). The temperature of the detector, injector, and oven was set at room temperature and the injection was done manually by a gas-tight syringe (Hamilton, 5 mL).

8.3 Results and discussion

8.3.1 Optical characteristics

The optical properties and photo stability of CQDs were already explained in our previous study [19]. The UV–Visible diffuse reflectance spectrum of MnO_2@CQDs nanocomposites has an excitation edge at 540 nm as shown in Fig. 8.1(c) inset and the calculated band gap is 1.3 eV. The band gap energy (E_g) needed to initiate the photocatalytic process has been calculated from Tauc plot.

8.3.2 Structural and morphological characteristics

The X-ray diffraction studies of the as-prepared photocatalyst displayed the presence of α-MnO_2 nanorods covered with CQDs. The diffraction pattern of as-synthesized MnO_2 samples exhibits smooth diffraction peaks for (110), (400), (211), (510), (411), (521), (002), (541) planes which are characteristics of α-MnO_2 structure with lattice constants a = 9.6957 Å and c = 2.7520 Å (JCPDS 44-0141). The CQDs exhibits a characteristic peak at around 22^o which is attributed to (002) plane of carbon reflecting the formation of CQDs over MnO_2 nanorods. Fig. 8.1(b) presents the BET (Brunner-Emmet-Teller) based N_2 adsorption and desorption curve of the MnO_2@CQDs nanocomposite, the adsorption-desorption isotherms are typical type IV Langmuir due to the mesoporous nature of the nanocomposite. The composite shows the surface area of 95.3 m^{2}g^{-1} with a pore diameter of 39 nm (inset Fig. 1b).

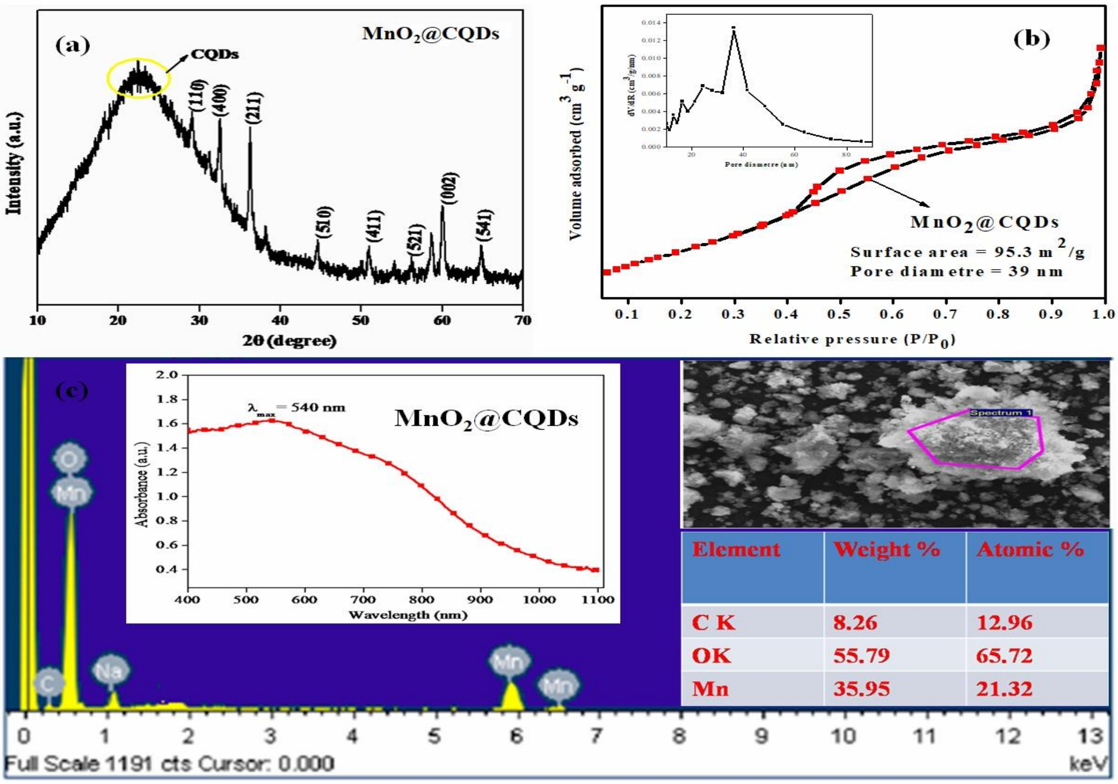

Element	Weight %	Atomic %
C K	8.26	12.96
OK	55.79	65.72
Mn	35.95	21.32

Fig. 8.1: (a) XRD pattern (b) BET analysis (inset BJH plot). (c) EDS spectra (inset DRS spectra) for MnO_2@CQDs.

The HRTEM and FESEM images are shown in Fig. 8.2 depicted the formation of MnO_2 nanorods coated by CQDs. The MnO_2 nanorods are open-ended (Fig. 8.2(b, c)) with average dimensions of 5 nm and 1 nm (L*B). The CQDs which are spherical in shape is seen to be deposited on the surface of MnO_2 (Fig. 8.2(a)). The SAED pattern (Fig. 8.2(d)) is in consonance with the XRD and TEM results showing the α-MnO_2 structure elongation along a 1D direction.

8.3.3 X-ray photon spectroscopy (XPS) characteristics

The surface composition and chemical state of photocatalysts were recorded by XPS and the survey spectra are presented in Fig. 8.3(a). The survey spectrum shows the presence of elements like Mn, O, and C. The peaks for α-MnO_2 corresponds to Mn $2p_{3/2}$ and Mn $2p_{1/2}$ spin states were observed at a binding energy of 642.2 and 653.7 eV respectively, which clearly indicates the presence of tetravalent Mn^{+4} ions. The high-resolution C 1s peak is deconvoluted into two signals, which includes the (sp^2) C-C and C-O-C bond at 283.4 and 285 eV respectively. Likewise, the deconvoluted peaks of O 1s at 528.7 eV and 530.3 eV are due to the linkage of Mn-O and Mn-OH respectively.

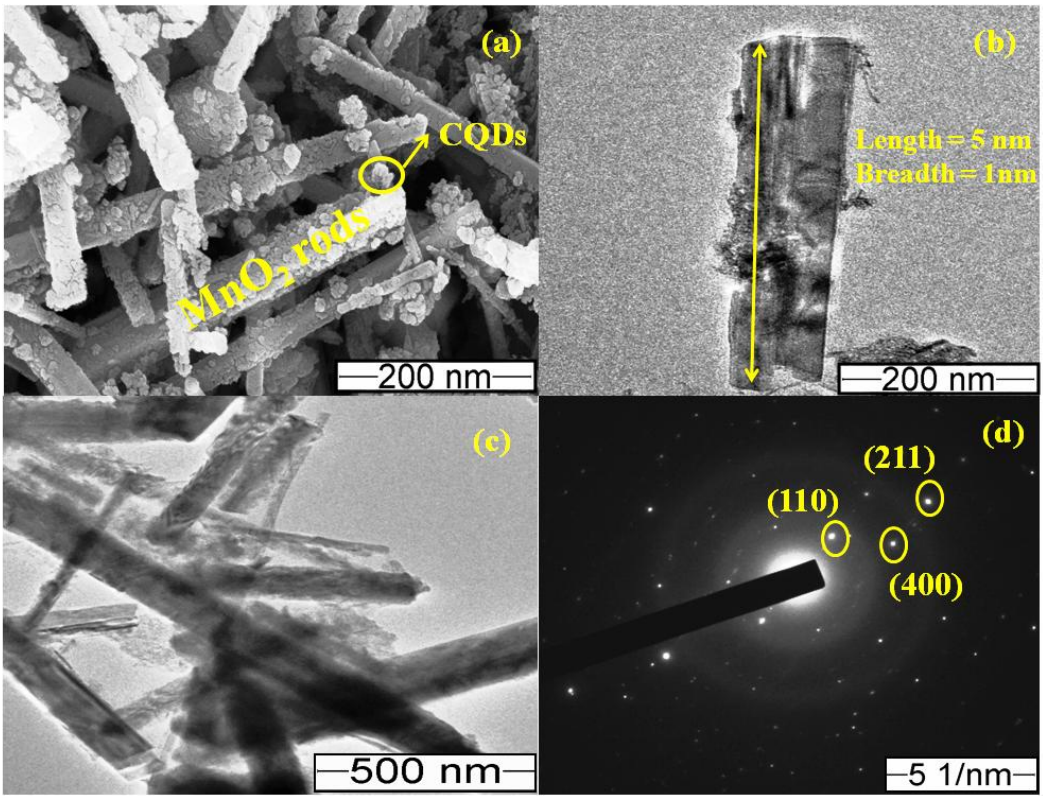

Fig. 8.2: (a) FESEM (b, c) HRTEM (d) SAED pattern for MnO_2@CQDs.

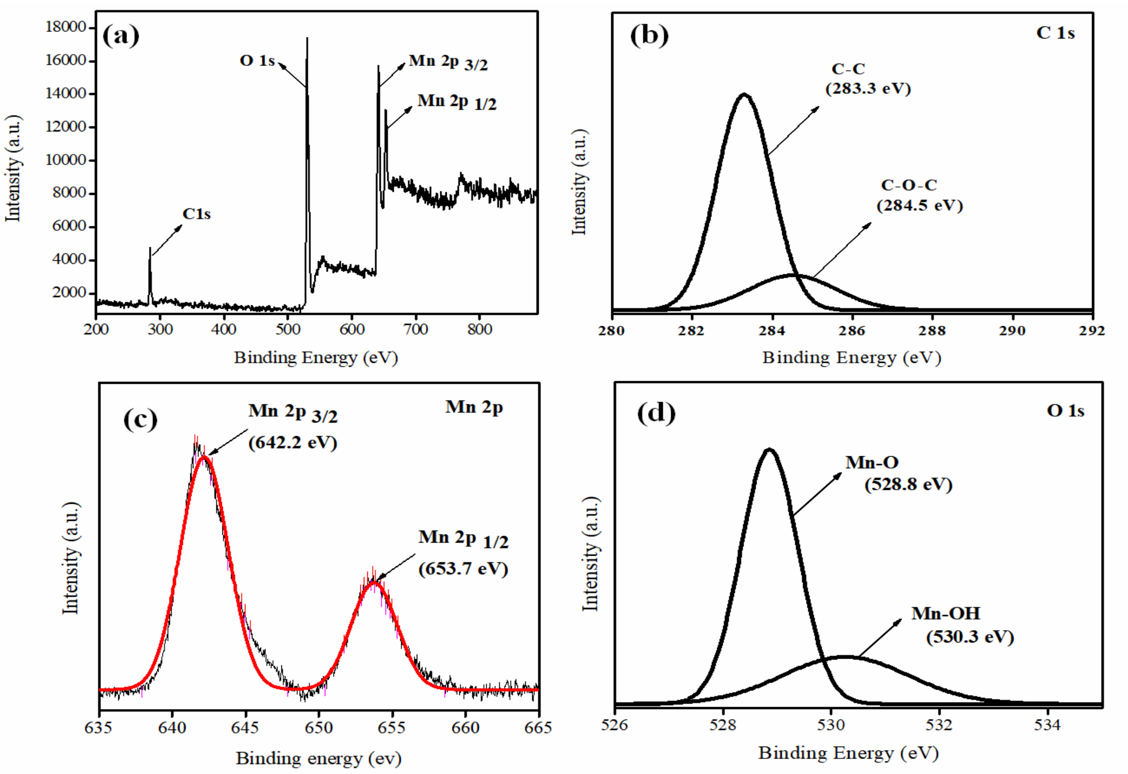

Fig. 8.3: (a) XPS survey (b) C1s (c) Mn 2p $_{3/2}$ (c) O 1s for MnO_2@CQDs.

8.4 Photocatalytic activity for the Phenol degradation

8.4.1 Kinetic study by MnO_2@CQDs photocatalyst

The efficiency of the photocatalyst was tested using three experiments, first photolysis (without catalyst) and secondly catalysis in dark was carried out. But no results for phenol degradation were obtained signifying that the activity merely due to the photocatalytic process. The photocatalytic phenol degradation was carried out under visible light at different time intervals. The kinetics of phenol degradation was examined using Langmuir-Hinshelwood equation $R = -dC/dt = kKC /1 +KC$, where R is the rate of photocatalytic degradation (mol l^{-1} min^{-1}), C is the concentration of reactant (mol l^{-1}), t is the irradiation time (min), k (min^{-1}) is rate constant, and K (l mg^{-1}) is Langmuir- Hinshelwood adsorption coefficient. At very low concentration, $KC \ll 1$ and thus it can be neglected, the gained simplified form of the above equation $R = -dC/dt = kKC$ or $(C/C_0) = e^{kKt} = e^{kt}$, where C_0 and C are initial and final concentration and k is the apparent pseudo first-order rate constant (min^{-1}). The photocatalyst MnO_2@CQDs shows 90% phenol degradation efficiency with a rate constant of 0.029 min^{-1} as shown in Fig. 8.4(a).

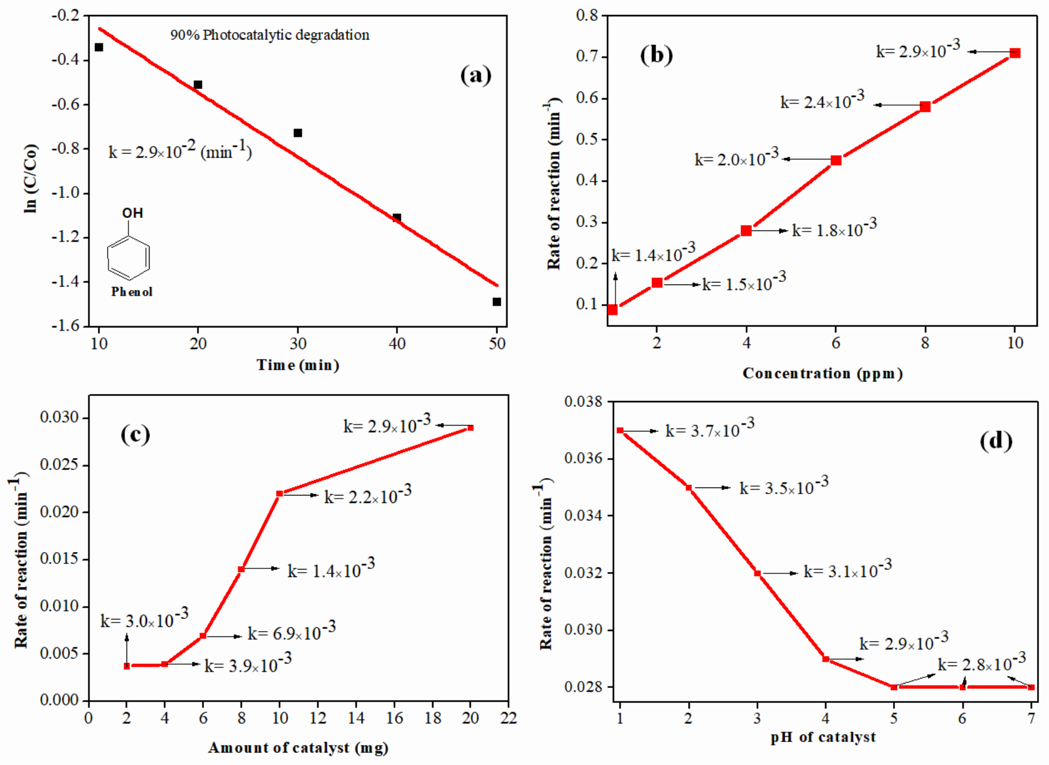

Fig. 8.4: (a) ln(C/Co) for photocatalytic degradation of phenol (b) Rate of reaction versus change in the concentration of phenol (c) change in the amount of catalyst (d) change in pH by MnO_2@CQDs.

8.4.2 Optimization under different reaction conditions

Further investigation was conducted to understand the effect of reaction conditions on the photodegradation of phenol. The absorbance spectra depict at varying phenol concentration. The degradation rate constant for phenol also varies with the changing concentration as shown in Fig. 8.4(b). At the concentration of 10 ppm, the maximum (90%) efficiency was achieved in 50 min. Similarly, the effect of catalyst (MnO_2@CQDs) dosage on phenol photocatalytic degradation was also studied. It was seen that greater MnO_2@CQDs loading in solution would extensively increase the rate of reaction ((Fig. 8.4(c)), 20 mg MnO_2@CQDs /50 mL in phenol solution resulted in 90% degradation efficiency further increase in the dosage of photocatalyst shows no increase in the degradation efficiency of phenol. Volatile organic compounds at altered pH conditions display separate charges and physicochemical behaviour [22]. The pH of water samples plays an important part in the photocatalytic degradation process of organic contaminants. The effect of pH in the range from 1 to 7 on the photocatalytic degradation was also investigated. The degradation rate was found to be higher at pH=5 and remains constant at a basic range as shown in Fig. 8.4(d). In, acidic condition the band gap decrease due to a strong interaction between acidic (H^+) with phenol and thus we found a certain change in efficiency. But no such case happens in basic conditions.

The activity of the regenerated MnO_2@CQDs catalyst was also studied by washing with water, as shown in Fig. 8.5(b) the efficiency was almost similar for three cycles. In fourth and fifth cycles the efficiency decreases up to 80% which is due to adsorption of intermediates on the surface of the catalyst. The role of reactor surface area (illumination area) was also studied under visible light using MnO_2@CQDs as photocatalyst as shown in Fig. 8.5(c). It was observed that the degradation efficiency increased twice by increasing the illumination area (area of reactor occupied by reaction mixture and exposed to irradiation source) of the reactor [23].

8.4.3 Photocatalytic mechanism for MnO_2@CQDs as a photocatalyst

As shown in Fig. 8.5 (a) upon addition of different scavengers, it was found that the reaction was inhibited to some extent by the addition of methanol and DMSO which are a hole (h^+) and electron (e^-) scavenging agents. The reaction was highly masked by IPA which is hydroxyl radical ($OH^\cdot$) scavenger, which means that these radicals generated from holes are highly responsible for photodegradation of phenol.

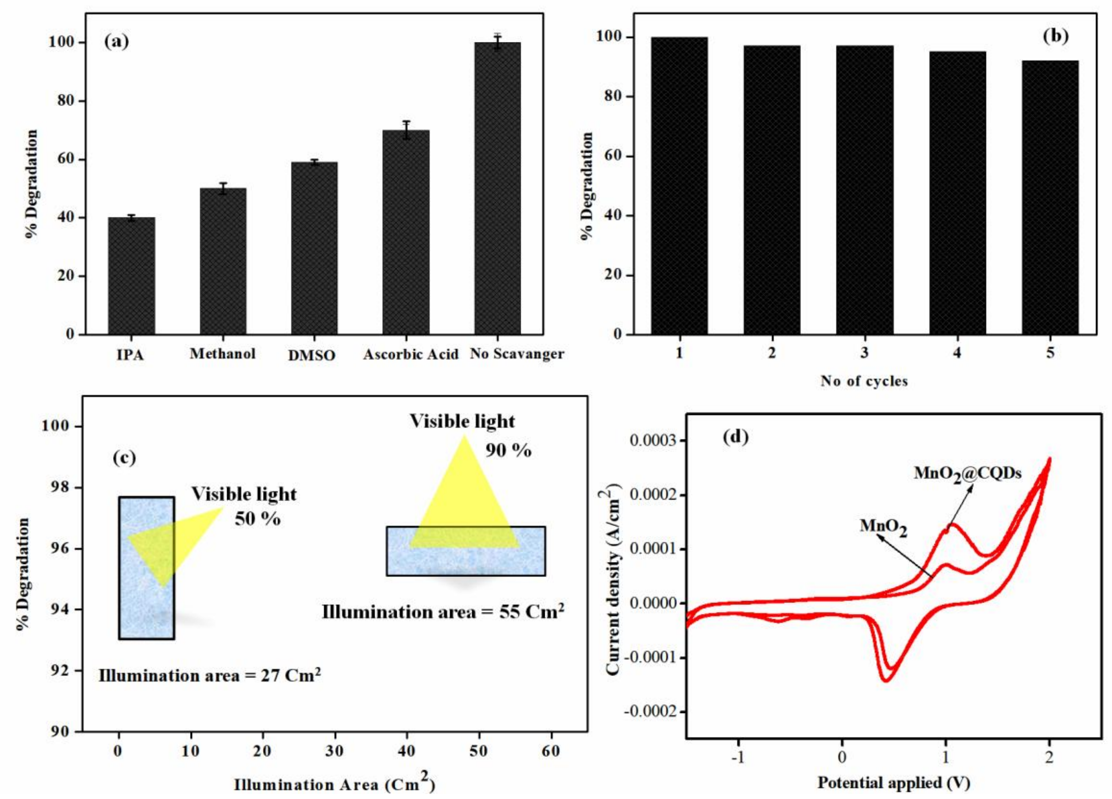

Fig. 8.5: (a) Effect of different scavengers (b) Effect of no. of cycles (c) Effect of the illumination area on % degradation of phenol (d) CV analysis of MnO_2@CQDs.

In addition to the above analysis, the CV responses of MnO_2 and MnO_2@CQDs composite were also done to examine the charge generation of conducting materials. A rectangular type CV with symmetry in cathodic and anodic directions indicates the ideal conducting materials. It is seen clearly in Fig. 8.5(d) the composite shows a larger current which is responsible for the larger photocatalytic behavior. Notably, the larger current behavior of the composite is due to the introduction of CQDs onto MnO_2 nanorods. Because the current arises from the transport of photogenerated electrons to the back contact and the simultaneous capture of photogenerated holes by hole scavengers in the composites.

In MnO_2@CQDs composite MnO_2 acts as an electron acceptor and CQD acts as an electron donor. The degradation mechanism of phenol is initiated by absorption of a photon that equals/exceeds its band gap energy (1.3 eV) generating electron-hole (e^-h+) pairs where h^+VB is strongly oxidizing and e^-CB is strongly reducing. The h^+ are highly activated as observed by scavenger study, reacts with the adsorbed species such as phenol compounds, water, hydroxide ion and oxygen [24-25]. At the external surface of the catalyst, the h^+ & e^- participates in redox reactions with adsorbed species. Oxidation of H_2O/OH^- by the h^+

generates the $OH^{\cdot}$ which is an extremely powerful oxidant. The plausible degradation reactions for a photocatalytic activity of MnO_2@CQDs are expected below.

$(MnO_2@CQDs) + h\nu \text{ (visible light)} \longrightarrow e^- + h^+$ (1)

$h^+tr + e^-tr \longrightarrow e^- + \text{heat}$ (2)

$4h^+ + 2H_2O \longrightarrow OH^{\bullet} + 4H^+$ (3)

$h^+ + OH^- \longrightarrow OH^{\bullet}$ (4)

$e^- + O_2 \longrightarrow O_2^{\cdot -}$ (5)

$O_2^{\cdot -} + H^+ \longrightarrow 2OH^{\cdot}$ (6)

$\text{Phenol} + OH^{\bullet} \rightarrow CO_2 + H_2O$ (7)

Finally the $OH^{\bullet}$ radical reacts with phenol (C_6H_6OH) to produce carbon dioxide (CO_2) and water (H_2O) as end products. The complete photo mineralized end products were also detected by GC (CO_2) analysis. The estimation of CO_2 after the photodegradation of phenol by MnO_2@CQDs (Fig. 8.7) shows that, with an increase in time, the amount of CO_2 increases progressively. At the intermediate stage of the reaction, the sample contains dechlorinated & low molecular weight organic compounds which are less harmful than parent compound and finally all the intermediates were photo mineralized to CO_2 after 60 minutes. The photocatalyst MnO_2@CQDs evolve the highest amount of CO_2 compared to solely MnO_2 and CQDs.

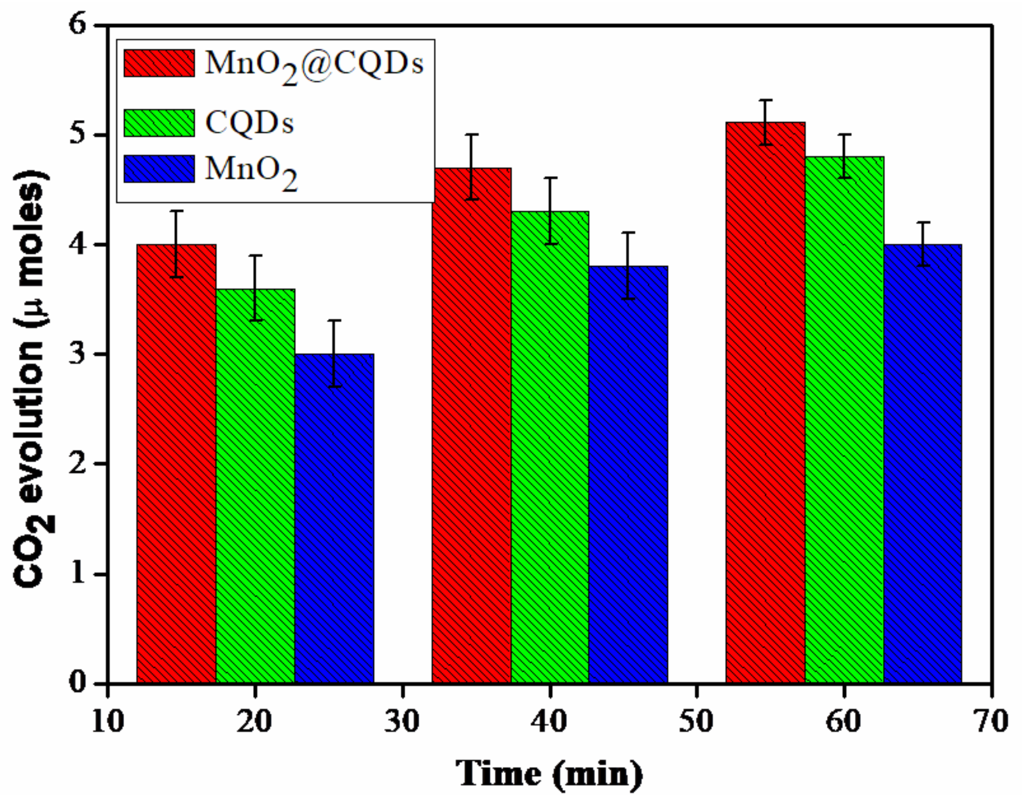

Fig. 8.7: Comparative study for photocatalytic degradation of phenol by CO_2 evolution.

References

1. Bunz UH, Rotello VM. Gold nanoparticle–fluorophore complexes: sensitive and discerning “noses” for biosystems sensing. Angewandte Chemie International Edition. 2010 Apr 26;49(19):3268-79.

2. Descalzo AB, Martínez- Máñez R, Sancenon F, Hoffmann K, Rurack K. The supramolecular chemistry of organic–inorganic hybrid materials. Angewandte Chemie International Edition. 2006 Sep 11;45(36):5924-48.

3. Yuan X, Tay Y, Dou X, Luo Z, Leong DT, Xie J. Glutathione-protected silver nanoclusters as cysteine-selective fluorometric and colorimetric probe. Analytical chemistry. 2013 Jan 11;85(3):1913-9.

4. Hu B, Zhao Y, Zhu HZ, Yu SH. Selective chromogenic detection of thiol-containing biomolecules using carbonaceous nanospheres loaded with silver nanoparticles as carrier. ACS nano. 2011 Mar 17;5(4):3166-71.

5. Wang J, Qu X. Recent progress in nanosensors for sensitive detection of biomolecules. Nanoscale. 2013;5(9):3589-600.

6. Chen WY, Huang CC, Chen LY, Chang HT. Self-assembly of hybridized ligands on gold nanodots: tunable photoluminescence and sensing of nitrite. Nanoscale. 2014;6(19):11078-83.

7. Goesmann H, Feldmann C. Nanoparticulate functional materials. Angewandte Chemie International Edition. 2010 Feb 15;49(8):1362-95.

8. Daniel MC, Astruc D. Gold nanoparticles: assembly, supramolecular chemistry, quantum-size-related properties, and applications toward biology, catalysis, and nanotechnology. Chemical reviews.

9. Mehta A, Sharma M, Kumar A, Basu S. Effect of Au content on the enhanced photocatalytic efficiency of mesoporous Au/TiO_2 nanocomposites in UV and sunlight. Gold Bulletin. 2017 Mar 1;50(1):33-41.

10. Mehta A, Sharma M, Kumar A, Basu S. Gold nanoparticles grafted mesoporous silica: a highly efficient and recyclable heterogeneous catalyst for reduction of 4-nitrophenol. Nano. 2016 Sep;11(09):1650104.

11. Liu D, Wang Z, Jiang X. Gold nanoparticles for the colorimetric and fluorescent detection of ions and small organic molecules. Nanoscale. 2011;3(4):1421-33.

12. Amjadi M, Farzampour L. Fluorescence quenching of fluoroquinolones by gold nanoparticles with different sizes and its analytical application. Journal of Luminescence. 2014 Jan 1;145:263-8.

13. Liu Y, Zhou Q, Yuan Y, Wu Y. Hydrothermal synthesis of fluorescent carbon dots from sodium citrate and polyacrylamide and their highly selective detection of lead and pyrophosphate. Carbon. 2017 May 1;115:550-60.

14. Hu R, Li L, Jin WJ. Controlling speciation of nitrogen in nitrogen-doped carbon dots by ferric ion catalysis for enhancing fluorescence. Carbon. 2017 Jan 1;111:133-41.

15. Liu ML, Chen BB, Liu ZX, Huang CZ. Highly selective and sensitive detection of 2, 4, 6-trinitrophenol by using newly developed blue–green photoluminescent carbon nanodots. Talanta. 2016 Dec 1;161:875-80.

16. Huang H, Liao L, Xu X, Zou M, Liu F, Li N. The electron-transfer based interaction between transition metal ions and photoluminescent graphene quantum dots (GQDs): a platform for metal ion sensing. Talanta. 2013 Dec 15;117:152-7.

17. Zhao HX, Liu LQ, De Liu Z, Wang Y, Zhao XJ, Huang CZ. Highly selective detection of phosphate in very complicated matrixes with an off–on fluorescent probe of europium-adjusted carbon dots. Chemical Communications. 2011;47(9):2604-6.

18. Li H, He X, Kang Z, Huang H, Liu Y, Liu J, Lian S, Tsang CH, Yang X, Lee ST. Water- soluble fluorescent carbon quantum dots and photocatalyst design. Angewandte Chemie International Edition. 2010 Jun 14;49(26):4430-4.

19. Liu R, Huang H, Li H, Liu Y, Zhong J, Li Y, Zhang S, Kang Z. Metal nanoparticle/carbon quantum dot composite as a photocatalyst for high-efficiency cyclohexane oxidation. ACS Catalysis. 2013 Dec 20;4(1):328-36.

20. Luo P, Li C, Shi G. Synthesis of gold@carbon dots composite nanoparticles for surface enhanced Raman scattering. Physical Chemistry Chemical Physics. 2012;14(20):7360-6.

21. Mandani S, Sharma B, Dey D, Sarma TK. Carbon nanodots as ligand exchange probes in Au@C-dot nanobeacons for fluorescent turn-on detection of biothiols. Nanoscale. 2015;7(5):1802-8.

22. Köstereli Z, Severin K. Array-based sensing of purine derivatives with fluorescent dyes. Organic & biomolecular chemistry. 2015;13(35):9231-5.

23. Amjadi M, Shokri R, Hallaj T. Interaction of glucose‐ derived carbon quantum dots with silver and gold nanoparticles and its application for the fluorescence detection of 6‐ thioguanine. Luminescence. 2017 May 1;32(3):292-7.

24. Press P. Martindale: the complete drug reference. Sweetman SC, London. 2009:29-31.

25. Pan J, Zheng Z, Yang J, Wu Y, Lu F, Chen Y, Gao W. A novel and sensitive fluorescence sensor for glutathione detection by controlling the surface passivation degree of carbon quantum dots. Talanta. 2017 May 1;166:1-7.

26. Gu J, Hu D, Wang W, Zhang Q, Meng Z, Jia X, Xi K. Carbon dot cluster as an efficient "off–on" fluorescent probe to detect Au (III) and glutathione. Biosensors and Bioelectronics. 2015 Jun 15;68:27-33.

27. Hou J, Zhang F, Yan X, Wang L, Yan J, Ding H, Ding L. Sensitive detection of biothiols and histidine based on the recovered fluorescence of the carbon quantum dots–Hg (II) system. Analytica chimica acta. 2015 Feb 15;859:72-8.

28. Niu WJ, Shan D, Zhu RH, Deng SY, Cosnier S, Zhang XJ. Dumbbell-shaped carbon quantum dots/AuNCs nanohybrid as an efficient ratiometric fluorescent probe for sensing cadmium (II) ions and l-ascorbic acid. Carbon. 2016 Jan 1;96:1034-42.

29. Li L, Wang C, Luo J, Guo Q, Liu K, Liu K, Zhao W, Lin Y. Fe^{3+}-functionalized carbon quantum dots: A facile preparation strategy and detection for ascorbic acid in rat brain microdialysates. Talanta. 2015 Nov 1;144:1301-7.

30. He D, Zheng C, Wang Q, He C, Lee YI, Wu L, Hou X. Dielectric barrier discharge-assisted one-pot synthesis of carbon quantum dots as fluorescent probes for selective and sensitive detection of hydrogen peroxide and glucose. Talanta. 2015 Sep 1;142:51-6.

Conclusion and Future Outlook

The core focus of this thesis is to bring some change in the photocatalytic process for environmental applications. Here it has been demonstrated the synthesis of metal oxide nanostructures (TiO_2, $SiO_{2,}$ MnO_2) and CQDs with different physical properties. It has been enlightened that the photocatalytic efficiency of TiO_2 and SiO_2 can be improved by tuning its band gap with the help of novel metals. These novel metals not only improved the lifetime of the charge carriers but also greatly activated metal oxides in direct sunlight resulting in higher photocatalytic efficiency. Moreover, we have explored the novel methodology kill "waste by waste" for solving two environmental problems using the same catalyst. In this process, we first detect heavy metal ions from water and then used the same solution for photocatalytic degradation of dyes. At the end of work, we have fabricated a new photocatalyst, highlighting spherical CQDs onto MnO_2 nanorods for photodegradation of phenol. Although the results obtained were better but the enhancement is needed in terms of the following points as an extension of this research work.

In present thesis work, we have explored the photocatalysis work more by elucidation the physical characteristics of catalyst and not the electrochemical behavior. Though people are now focusing on photoelectrocatalytic (PEC) degradation of organic pollutants with simultaneous H_2 evolution which has attracted much attention, owing to the input of a small external potential to help the electron transfer. In a PEC reactor, the electrons transfer along the photoanode and reach the counter electrode (cathode) through an outer circuit. Building on this understanding and the advantages of the synergistic effect between different materials for fabrication of the photocatalyst/photoanode, their morphology may facilitate charge separation and transfer, thereby leading to better photocatalytic-photoelectrochemical performance.

Materials and Design 155 (2018) 485–493

Contents lists available at ScienceDirect

Materials and Design

journal homepage: www.elsevier.com/locate/matdes

Carbon quantum dots/TiO_2 nanocomposite for sensing of toxic metals and photodetoxification of dyes with kill waste by waste concept

Akansha Mehta, Amit Mishra, Shagun Kainth, Soumen Basu *

School of Chemistry and Biochemistry, Thapar University, Patiala 147004, India

HIGHLIGHTS

- A novel "kill waste by waste" approach was developed for detection of heavy metals by carbon quantum dots.
- Lead sensing and deposition on TiO_2-carbon quantum dots was preferred over other toxic metals.
- The lead deposited TiO_2-carbon quantum dots nanocomposites completely mineralized the industrial dyes to CO_2 and H_2O.
- The nanocomposites was effective for the treatment of real waste water samples.

GRAPHICAL ABSTRACT

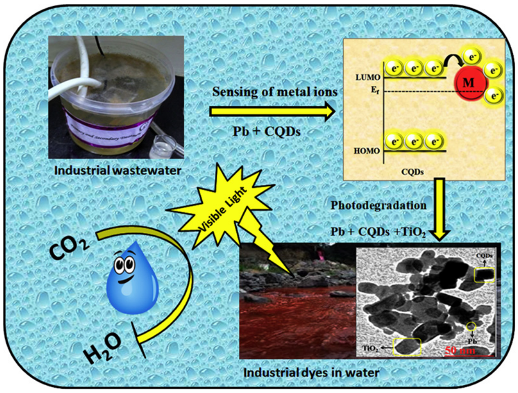

ARTICLE INFO

Article history:
Received 21 March 2018
Received in revised form 6 June 2018
Accepted 7 June 2018
Available online 08 June 2018

Keywords:
Carbon quantum dots
Fluorescence quenching
Designing lead ions detection
TiO_2
Photodetoxification

ABSTRACT

The exposure of even low amount of heavy metals and industrial dyes in wastewater leads to cardiovascular, neurological and developmental disorders. Consequently, millions of inorganic and organic pollutants containing toxic heavy metals have been accounted as water contaminants. In this report, a novel approach has been designed based on the methodology to "kill waste by waste". Firstly the toxic metals like lead (Pb) ions were detected using fluorescence carbon quantum dots (CQDs) and after impregnation of TiO_2 into the same Pb-CQDs composite, it was further used for photodegradation of harmful industrial dyes. The CQDs have been designed as a nanosensor for Pb ion detection and its fluorescence is effectively quenched with good sensitivity (0.070 μM) and selectivity. This Pb-CQDs solution was further immersed in TiO_2 by wet impregnation method to fabricate Pb-CQDs-TiO_2 (PCT) nanocomposite with a change in the energy gap (3.2 to 2.8 eV) making the composite active in visible light irradiation. The degradation efficiency achieved ~100% mark for RBX dye and 1.8 μmols of CO_2 evolution was observed in 60 min. The plausible mechanism is proposed based on GCMS studies suggesting the formation of intermediates like triazine and aryl sodium sulphonates before complete decomposing into CO_2 and water.

1. Introduction

The toxic effluent in the form of heavy metals and harmful dyes are two major concerns abating the quality of water. This is reasonably due to ever-growing population, commercialization, ecological degradation and harmful domestic/industrial discharge. Among diverse heavy metal

---

* Corresponding author.
E-mail address: soumen.basu@thapar.edu (S. Basu).

https://doi.org/10.1016/j.matdes.2018.06.015
0264-1275/

Check for updates

View Article Online
View Journal

Environmental
Science
Water Research & Technology

Accepted Manuscript

This article can be cited before page numbers have been issued, to do this please use: A. Mehta, A. Mishra and S. Basu, *Environ. Sci.: Water Res. Technol.*, 2018, DOI: 10.1039/C8EW00235E.

Volume 2 | Number 1 | January 2016 | Pages 1–234
Environmental
Science
Water Research & Technology
rsc.li/es-water
ISSN 2053-1400
ROYAL SOCIETY OF CHEMISTRY
TUTORIAL REVIEW
Anna Lee, Seth B. Darling et al
Membrane materials for water purification: design, development, and application
175 YEARS

This is an Accepted Manuscript, which has been through the Royal Society of Chemistry peer review process and has been accepted for publication.

Accepted Manuscripts are published online shortly after acceptance, before technical editing, formatting and proof reading. Using this free service, authors can make their results available to the community, in citable form, before we publish the edited article. We will replace this Accepted Manuscript with the edited and formatted Advance Article as soon as it is available.

You can find more information about Accepted Manuscripts in the author guidelines.

Please note that technical editing may introduce minor changes to the text and/or graphics, which may alter content. The journal's standard Terms & Conditions and the ethical guidelines, outlined in our author and reviewer resource centre, still apply. In no event shall the Royal Society of Chemistry be held responsible for any errors or omissions in this Accepted Manuscript or any consequences arising from the use of any information it contains.

ROYAL SOCIETY
OF CHEMISTRY

rsc.li/es-water

NJC

PAPER

Cite this: *New J. Chem.*, 2017, **41**, 4573

Enhanced photocatalytic water splitting by gold carbon dot core shell nanocatalyst under visible/sunlight†

Akansha Mehta,[a] Pooja D.,*[b] Anupma Thakur[b] and Soumen Basu*[a]

Hydrogen production from water using photocatalysts under sunlight still remains a huge challenge. The search for a suitable photocatalyst combines an ability to dissociate water molecules with a band gap that absorbs light in the visible range and also water stability. In this regard, our present study represents a facile method for fabricating carbon quantum dots (CQDs) and Au@CQDs, which are useful for photocatalytic hydrogen generation from water. The optical properties revealed a band gap energy (eV) for CQDs (2.78) and Au@CQDs (2.68); additionally, photoluminescence analysis of CQDs showed maximum emission at 460 nm while also exhibiting a red shift when excited at longer wavelengths. Spherical shaped CQDs, with an average size of 7 nm (*d* spacing of 0.22 nm), and core shell Au@CQDs, with a shell thickness of 6 nm, were observed by HRTEM analysis. Comparatively, both CQDs (260 μmol) and Au@CQDs (280 μmol) displayed a higher rate of hydrogen production under sunlight irradiation than other carbon materials reported in earlier literature. In photoelectrochemical analysis, current densities associated with Au@CQDs and CQDs photoelectrodes (PEs) were found to be 16 mA cm^{-2} and 6 mA cm^{-2}, respectively at a very low bias of 0.16 V. Moreover, frequency response analysis (FRA) associated with Randel's equivalent circuit showed that polarization/charge transfer resistance for Au@CQDs was very low (2.74 Ohm) over that of CQDs PEs (88.8 Ohm), which was 12.9 kOhm for bare TiO_2 PEs. All these observations indicate that both CQDs and Au@CQDs are ample for preventing an electron–hole recombination processes, which ultimately leads to superior photocatalytic water splitting.

Received 21st March 2017,
Accepted 2nd May 2017

DOI: 10.1039/c7nj00933j

rsc.li/njc

1. Introduction

In view of growing energy demands, hydrogen fuel is being considered as an ideal sustainable candidate owing to its zero emission and higher chemical energy per mass (142 MJ kg^{-1}) characteristics. Its production from existing natural and renewable resources, such as water and biomass, further strengthens its candidature. With introduction of the Honda Fujishima's effect, a significant amount of thrust has been made to develop a cost-effective technique for hydrogen production such as photo catalysis over conventional approaches. In this direction, semiconductor materials, such as metal oxides and their morphological modifications, have been intensely investigated for effective photocatalytic water splitting.[1,2] However, achieved quantum yields are still low; therefore, several efforts in terms of material and technique are being made to increase the same.

Of late, carbonaceous nanostructures such as carbon nanotubes, graphene, graphene oxide, *etc.*, have been extensively adopted due to their environment compatibility, cost effectiveness, and rich electron transport mechanism. Kang *et al.*[3] demonstrated an amorphous carbon nitride photocatalyst with an impressively extended visible-light-responsive range for photocatalytic hydrogen generation. Likewise, Silva *et al.*[4] synthesized a carbon nanotubes-TiO_2 catalyst for hydrogen production from methanol and saccharides. Several other reports also advocate the effective role of carbonaceous materials to enhance photocatalytic hydrogen production.[5,6] In the recent past, carbon dots have been successfully demonstrated for water splitting due to their visible light adsorption, tunable excitation/emission characteristic, and high photostability. Yu *et al.*[7] synthesized carbon nanocomposites with TiO_2 for water-splitting under either UV or visible-light illumination. The observed highest hydrogen production rate was 9.1 μmol h^{-1} over neat TiO_2 photocatalyst. Xu *et al.*[8] developed amino conjugated carbon quantum dots to boost photocatalytic hydrogen production up to 136.55 μmol for a period of 5 hours. Despite several efforts made until now with photocatalytic hydrogen production using carbon dots (CQDs), the quantum yield is still very low under visible as well as

---

[a] *School of Chemistry and Biochemistry, Thapar University, Patiala-147004, India. E-mail: soumen.basu@thapar.edu, sbasu1980@gmail.com; Tel: +91 8727001158*

[b] *CSIR-Central Scientific Instruments Organisation, Chandigarh-160030, India. E-mail: poojaiitr@csio.res.in*

† Electronic supplementary information (ESI) available. See DOI: 10.1039/c7nj00933j

Journal of Photochemistry and Photobiology A: Chemistry 343 (2017) 1–6

Contents lists available at ScienceDirect

Journal of Photochemistry and Photobiology A: Chemistry

journal homepage: www.elsevier.com/locate/jphotochem

Controlled photocatalytic hydrolysis of nitriles to amides by mesoporous MnO_2 nanoparticles fabricated by mixed surfactant mediated approach

Akansha Mehta, Soumen Basu*

School of Chemistry and Biochemistry, Thapar University, Patiala 147004, India

ARTICLE INFO

Article history:
Received 21 February 2017
Received in revised form 7 April 2017
Accepted 11 April 2017
Available online 14 April 2017

Keywords:
MnO_2 nanoparticles
Synergistic effect of CTAB and SDS
Photocatalysis
Hydrolysis of nitriles

ABSTRACT

The solid-phase MnO_2 nanoparticles fabricated by surfactant template method were exploited as the photocatalyst for the effective one-step synthesis of amides. Cationic or anionic surfactants and their combinations were used as porous templates to obtain the mesoporous MnO_2 nanoparticles with variable pore volume (0.23–1.95 cm^3/g). The morphological and structural observation of the material confirms the uniform facet structure (37.68 nm) of MnO_2 nanoparticles. The surface elemental state was confirmed by XPS analysis confirming Mn $2p_{3/2}$ (642.5 eV) and Mn$2p_{1/2}$ (654.7 eV) spin states, that are common for the tetravalent Mn ions. Presence of surfactant as stabilizer was also witnessed with a strong peak of C 1s (283–286 eV). The textural parameters obtained from XRD and Raman analysis depicted the β-phase and rutile type framework of MnO_2. The selective conversion of nitriles to amides was studied without any acid by products under visible light irradiation in the basic/neutral medium. Amides were obtained from various substrates (nitriles) with excellent yields (70–90%).

1. Introduction

One of the most important industrial reactions in the organic chemistry is amide bond formation as it constitutes important moieties in many pharmaceutical and biologically active ingredients [1]. Moreover, the flattering properties of amides like stability, conformational diversity and high polarity make it one of the most reliable and accepted functional groups in every branch of organic chemistry. Among all the methods reported for the fabrication of amides, hydration of nitriles has become one of the most widely used methods to obtain primary amides. But this is a challenging reaction as there is possibility of acid formation from amides. The hydrolysis reaction is catalyzed in acidic and basic medium, but many of the methods requires harsh conditions with poor yields due to further conversion of amides to acids [2,3]. Improved methods for the selective and controlled synthesis of amides using catalysts under stable conditions are of great demand [4](a). In this regard formation of amides by hydrolysis of nitriles using transition metal oxides nanomaterials as a photocatalyst is good choice to obtain better yields. It is a principal objective of the present study to provide a new method for converting nitriles to amides.

Nanoporous transition metal oxides with controlled morphology, porous structures, tunable nano pores and well ordered mesostructures make them ideal photocatalysts in the field of catalysis. During recent times, of all the transition metal oxides, manganese dioxide (MnO_2) nanostructures have received keen attention due to its attractive physical and chemical properties [4](b, c). The MnO_2 is non-stoichiometric compound and can exist in different crystallographic forms. The crystallographic forms are generally supposed to be responsible for their variable properties and the controlled synthesis of MnO_2 which make the controlled design of a specific forma primary objective [5]. Previously, many processes have been developed for the synthesis of MnO_2 nanoparticles with different shapes and morphology. Out of all the processes MnO_2 nanostructures are commonly synthesized using hydrothermal treatment [6,7], sol–gel process [8,9], refluxing [10,11] and normal thermal approach [12] for enormous catalytic application [13,14] because of their different morphology and variable oxidation states. Several attempts have been made to further improve the catalytic activity by using some facile techniques [15,16] but enhancing surface area is an excellent way to improve its catalytic properties. As a remedial surfactants based synthesis are considered as best route to develop a mesoporous structure. They have the exceptional property to self-organize in the solution, which may modify the interfacial properties and increase the compatibility among the particles. Materials prepared without using

---

* Corresponding author.
E-mail address: soumen.basu@thapar.edu (S. Basu).

http://dx.doi.org/10.1016/j.jphotochem.2017.04.013

Plasmonics
https://doi.org/10.1007/s11468-018-0744-0

Optical Detection of Thiol Drugs by Core–Shell Luminous Carbon Dots—Gold Nanoparticles System

Akansha Mehta[1] · **Amit Mishra**[1] · **Soumen Basu**[1]

Received: 24 October 2017 / Accepted: 13 March 2018

Abstract

Nowadays, carbon quantum dots (CQDs) with size less than 10 nm have emerged as one of the most exciting areas of chemical research in the class of inorganic nanomaterials. This article presents interesting characteristics of CQDs and their fluorescence turn-on/turn-off quenching for the detection of 6-Thioguanine (6-TG). The CQDs were fabricated by a simple one-step microwave technique and used for the simultaneous reduction of Au^{3+} to form Au^0-CQD core–shell (Au@CQD) nanocomposites. The CQDs formed were spherical in shape having an average size of ~ 7 nm confirmed by high-resolution transmission electron microscopy (HRTEM) and DLS study. The interaction of CQDs with Au leads to its fluorescence turn-off up to 96% analyzed by UV-visible, fluorescence spectroscopy, and fluorescence lifetime measurements. The turn-on fluorescence of CQDs has been witnessed by the formation of complex with 6-TG $[\text{Au-(6-TG)}_n]^{3-}$ in the presence of thiols. Meanwhile, linear relationship between turn-on fluorescence against the concentration of 6-TG is obtained in the range of 0–100 μM with the correlation coefficient of 0.9944 and limit of detection for 6-TG has been found to be 0.01 μM. The Au@CQDs could also act as biosensor for the detection of various amino acids, enzymes, and pentids drug.

Keywords Carbon quantum dots · Fluorescence quenching · 6-Thioguanine · Turn-on/turn-off detection

Introduction

Noble metal (Au, Ag, etc.)-based plasmonic nanoparticles (NPs) have gained incredible significance as colorimetric sensors due to their distinctive and excellent characteristics like distance dependent optical properties and high extinction coefficients in visible region [1–10]. These metal NPs are known as excellent fluorescence quenchers and their quenching effect has been thoroughly explored on various fluorophores. In addition, these NPs have a huge number of applications in the field of sensing and nano-medicine [11–15]. Fluorescence quenching by the metal NPs is generally a type of energy transfer method taking place among the fluorophores and NPs. The composite formation of these metallic NPs with other active materials has been reported to be efficient in several advanced sensing and biomedical applications. But the composite formation with the quantum dot is least studied and composite materials of such scale can be effective because of alteration in optoelectronic properties.

Recently, composites with photoluminescent nanomaterials had gained interest due to their applicability in various fields, ranging from biomedical to optoelectronics fields [16, 17]. One new category of luminescent nanomaterials is carbon quantum dots (CQDs). CQDs are a rising category of carbon nanomaterial due to their impressive fluorescence property, good biocompatibility, photo stability, energy conversion capability, and water solubility. The great interest towards this small water soluble type of carbon could be credited to its character as eco-friendly and non-toxic nature, as an alternative to semiconductor quantum dots in diverse applications like electronics, drug delivery, and catalysis [18, 19]. The existence of carboxylic moiety onto the surface of CQDs has ability to function as both a reducing and stabilizing agent in the fabrication of metallic NPs, similar with other carboxyl-enriched ligands like citrates and ascorbates [20, 21]. If CQDs are able to create a shell surrounding the metal NPs, it may function like a self-assembled monolayer of stabilizing agent [22]. In the existence of these metal NPs, the fluorescence emission of these CQDs can be notably quenched as a result of energy

---

Electronic supplementary material The online version of this article (https://doi.org/10.1007/s11468-018-0744-0) contains supplementary material, which is available to authorized users.

✉ Soumen Basu
soumen.basu@thapar.edu

[1] School of Chemistry and Biochemistry, Thapar University, Patiala 147004, India

Gold Bull
DOI 10.1007/s13404-016-0191-7

ORIGINAL PAPER

Effect of Au content on the enhanced photocatalytic efficiency of mesoporous Au/TiO_2 nanocomposites in UV and sunlight

Akansha Mehta[1] · **Manu Sharma**[2] · **Ashish Kumar**[1] · **Soumen Basu**[1]

Received: 11 May 2016 / Accepted: 16 November 2016

Abstract Detoxification of harmful dyes through nonconventional catalytic processes is getting thrust in light of environmental remediation. Current work reveals synthesis of gold–titania (Au/TiO_2) mesoporous nanostructure and its enhanced photocatalytic performance for degradation of alizarin dye. Optically, Au/TiO_2 shows a characteristic surface plasmonic absorption band at 520 nm, whereas X-ray diffraction (XRD) pattern reveals the anatase phase of TiO_2 with fcc unit cell structure and tetragonal geometry. X-ray photon spectroscopy depicts (Au $4f_{7/2}$ at 84.0 and Au $4f_{5/2}$ at 87.7 eV) the elemental state of gold (Au^0). Specific surface area was witnessed to decrease with increase of Au content (169, 141, 130, and 119 m^2/g for 1, 2, 3, and 4 wt%, respectively). The mesoporous Au/TiO_2 nanocomposite showed higher catalytic performance in comparison to commercial nano-TiO_2 (P25), which is credited to better charge delocalization at metal semiconductor interface. The reusability studies of the photocatalyst exhibited more than 98% degradation of the dye even after 10 consecutive cycles.

Keywords Nanocomposites · HDP · Alizarin dye · Photocatalysis

---

✉ Ashish Kumar
ashish.kumar@thapar.edu

✉ Soumen Basu
soumen.basu@thapar.edu

[1] School of Chemistry and Biochemistry, Thapar University, Patiala 147 004, India

[2] Department of Chemistry, Indian Institute of Technology Delhi, New Delhi 110016, India

Introduction

Dye pollutants are among the prime sources of water contamination from textile and printing industries. The treatment of these dye effluents is highly desired for the preservation of clean air, soil, and water. There is an immediate need to take some necessary steps to develop efficient photocatalyst to degrade these toxic pollutants.

Anatase phase of TiO_2 is one of the best photocatalyst for pollutant dye degradation. Selectively, TiO_2 is important due to their very low cost, excellent chemical and mechanical stability, catalytic activity, availability, and nontoxicity [1–3]. The only limitation for TiO_2 as a photocatalyst is that its band gap (3.2 eV for anatase) disables it to be active in visible light region of the solar spectrum. But, the presence of rutile phase shifts its absorption maximum towards visible light. Doping with metal or nonmetallic elements [4, 5] or by deposition of noble metal nanoparticles (NPs) on TiO_2 surface is also an effective way to improve the photocatalytic activity of the catalyst [6–8]. Previously, it has been reported that when TiO_2 is doped with noble metals, its photocatalytic activity is enhanced under UV and visible light irradiation. The improved UV light photocatalytic activity is recognized due to effective charge separation of the electron when they are transferred from conduction band (CB) of TiO_2 to metal NPs [9, 10]. On the other hand, the surface plasmon resonance effect of some metals like Au and Ag also helps TiO_2 to sensitize in visible light [11–13]. In advanced photocatalytic system, sunlight active metals have been given a major thrust and Au is favored due to rich photochemistry both in homogenous and heterogeneous systems. In homogenous systems, the dimeric complexes of Au have been reported as efficient materials for radical reaction under sunlight. Revol et al. reported radical

NANO: Brief Reports and Reviews
Vol. 11, No. 9 (2016) 1650104 (9 pages)

DOI: 10.1142/S1793292016501046

Gold Nanoparticles Grafted Mesoporous Silica: A Highly Efficient and Recyclable Heterogeneous Catalyst for Reduction of 4-Nitrophenol

Akansha Mehta*, Manu Sharma†, Ashish Kumar*,‡
and Soumen Basu*,§
*School of Chemistry and Biochemistry
Thapar University, Patiala-147004, India

†Department of Chemistry
Indian Institute of Technology Delhi
New Delhi-110016, India
‡ashish.kumar@thapar.edu
§soumen.basu@thapar.edu

Received 16 February 2016
Accepted 25 May 2016
Published 14 July 2016

Synthesis of gold nanoparticles dispersed uniformly on mesoporous silica (mAu/SiO_2) by homogeneous deposition–precipitation (HDP) method is used as an effective catalyst for reduction of 4-nitrophenol to 4-aminophenol. Silica provides support and surface area to increase the catalytic activity of gold. X-ray photon spectroscopy revealed binding energy of Au $4f_{7/2}$ (~84.0 eV) and Au $4f_{5/2}$ (~87.7 eV) which support the formation of Au^0 on SiO_2 surface. Au/SiO_2 showed Langmuir type-IV isotherms which are the characteristic features of mesoporous materials furthermore, pore size decreases with incorporation of Au NP's on SiO_2 surface. The enhancement is due to the strong interaction of Au^0 with silica support. The catalytic conversion was studied by UV-Visible spectroscopy and high performance liquid chromatography (HPLC) quantification method, which shows conversion of nitro group into amino group. In addition, the catalyst was easily separated and reused. The reusability of the catalyst exhibited better reduction of the 4-nitrophenol to 4-aminophenol even after 10 consecutive cycles. In comparison to trisodium citrate capped pure gold nanoparticles mAu/SiO_2 catalysts showed very good catalytic activity toward nitrophenol reduction. Here we conclude that embedment of metal catalysts like Au into high surface area support like silica is a positive step toward development of novel heterogeneous catalysts.

Keywords: Gold nanoparticles; silica; homogeneous deposition–precipitation method; catalytic reduction; 4-nitrophenol.

1. Introduction

A new class of materials, based on nanoparticles (NPs) in the composition of semiconductors (TiO_2, ZnO, etc.) and dielectrics (SiO_2, Al_2O_3, etc.) substantially extends the range of their several applications, particularly in heterogeneous catalysis, in the creation of electronic devices, chemical sensors, protecting coatings, bactericidal materials,